Western Graduate&PostdoctoralStudies

Western University
Scholarship@Western

Electronic Thesis and Dissertation Repository

12-3-2015 12:00 AM

Doping Plasmon-Enhanced TiO2 with Zirconia to Improve Solar Energy Harvesting in Dye-Sensitized Solar Cells

Anastasia Pasche, *The University of Western Ontario*

Supervisor: Paul Charpentier, *The University of Western Ontario*
A thesis submitted in partial fulfillment of the requirements for the Master of Engineering
Science degree in Chemical and Biochemical Engineering
© Anastasia Pasche 2015

Recommended Citation

DOPING PLASMON-ENHANCED TIO2 WITH ZIRCONIA TO IMPROVE
SOLAR ENERGY HARVESTING IN DYE-SENSITIZED SOLAR CELLS

Integrated Article Format

by

Anastasia Pasche

Graduate Program in Chemical and Biochemical Engineering

A thesis submitted in partial fulfillment
of the requirements for the degree of
Master of Engineering Science

The School of Graduate and Postdoctoral Studies
The University of Western Ontario
London, Ontario, Canada

© Anastasia Pasche 2015

Abstract

Solar energy is a promising solution towards meeting the world's ever-growing energy demand. Dye-sensitized solar cells (DSSCs) are hybrid organic-inorganic solar cells with potential for commercial application, but are plagued by inefficiency due to their poor sunlight absorption. Silver nanoparticles have been shown to enhance the absorptive properties of DSSCs, but their plasmonic resonance causes local hot spots, resulting in cell deterioration. This thesis studies the mitigation of thermal energy loss of plasmon-enhanced DSSCs by the co-incorporation of zirconia, a well-known thermostabilizer, into the cell's photoactive material. TiO_2 was also synthesized using green bio-sourced solvents in supercritical CO_2 to compare its performance in DSSCs to conventionally-synthesized TiO_2. Using an integrated approach to materials synthesis, characterization, cell fabrication, and solar simulation testing, it is shown that 5 molar % zirconia doping improves the photovoltaic performance of DSSCs by as much as 44%. Further, two optimized plasmonic cell architectures are presented that increase optical absorption and photocurrent in DSSCs. The integration of these nanomaterials into solar cells highlights easy fabrication methods, contributes to the development and commercialization of inexpensive and high-efficiency DSSCs, and may benefit other types of solar-harvesting devices.

Keywords

photovoltaics, dye-sensitized solar cells, titanium dioxide, zirconia thermostabilizing dopant, silver nanoparticles, core-shell nanostructures, plasmonic solar cells, atomic layer deposition, absorption enhancement, improved carrier collection, green bio-sourced solvents, supercritical carbon dioxide.

Acknowledgments

I'd like to thank the following individuals for their help during my master's thesis work:

- My supervisor Paul Charpentier for his constant support, encouragement, guidance, resources and funding. I admire his positive attitude, patience, and good humour.
- Qasem Alsharari for his help with syntheses, for training me on solar cell fabrication and testing, and for his discussions and guidance with my thesis topic.
- Lijuan Yang for her assistance with syntheses, apparatus setups, XRD characterizations and discussions.
- Wei Wu for his help with the selection and ordering of chemicals and materials, for discussions on reaction logistics, and his constant care towards maintaining a safe lab environment.
- William Xu for his help with UV-Vis and other characterizations and helpful discussions.
- Zakir Hossein for training me on several characterization techniques, including BET, and for your constant cheerful attitude.
- All my other lab colleagues for their support and help throughout my time at Western.

I'd also like to thank Tim Goldhawk and Todd Simpson at the Nanofab Lab facility at Western University for assisting me with SEM analysis of my samples and Andy Sun's research group for help with XRD and ALD.

Finally I'd like to thank Paul again for the opportunity to do collaborative research in France, and Yaocihuatl Medina-Gonzalez at the Laboratoire de Génie Chimique at INP-ENSIACET in Toulouse France for all her help with view-cell reactors, supercritical syntheses, and her incredible hospitality during my stay in France.

Table of Contents

List of Tables

List of Figures

List of Abbreviations, Symbols and Nomenclature

Abbreviations and Acronyms

AIPV	Automotive integrated photovoltaics
BSE	Back-scattering electrons
BJH	Barret-Joyner-Halenda
BET	Brunauer, Emmett and Teller
BIPV	Building integrated photovoltaics
CB	Conduction band
I-V	Current-voltage
DSSC	Dye-sensitized solar cell
EF	Electric Field
EQE	External quantum efficiency
FTO	Fluorine-doped tin oxide
GXL	Gas-expanded liquid
GW	Gigawatt (10^9 watts)
GBS	Green bio-source solvent
HSG	Hydrolytic sol-gel (synthesis route)
K	Kelvin (273.15 K = 0 ºC)
LH	Light harvesting
LSPR	Localized surface plasmon resonance
nm	Nanometer (1 x 10^{-9} m)
NP	Nanoparticle
NHSG	Non-hydrolytic sol-gel (synthesis route)
p-NPs	Plasmonic nanoparticles
psi	pounds per square inch (pressure)
PCE	Power conversion efficiency (η)
PV	Photovoltaic
RT	Room temperature (~25 ºC)
SE	Secondary electrons
SEM	Scanning electron microscope
SSA	Specific surface area (BET)

sccm	standard cubic centimeters per minute (flow rate)
$scCO_2$	Supercritical carbon dioxide
SCF	Supercritical Fluid
TW	Terawatt (10^{12} watts)
TEM	Tunnelling electron microscope
UV	Ultraviolet

Symbols

λ_{LSPR}	Localized surface plasmon resonance wavelength
η	Power conversion efficiency (PCE)

Nomenclature

$C_5H_8O_2$	Acetylacetone (acac)
Al_2O_3	Aluminum oxide
Ar	Argon
CO_2	Carbon dioxide
Cu	Copper
EtOH	Ethanol
Au	Gold
HCl	Hydrochloric acid
H_2	Hydrogen gas
H_2O_2	Hydrogen peroxide
C_3H_8O	Isopropanol
CH_3	Methyl (Me)
$HCON(CH_3)_2$	*N,N*-dimethylformamide (DMF)
N_2	Nitrogen gas
Pt	Platinum
Si	Silicon
Ag	Silver
Ag_2O	Silver(I) oxide
H_2SO_4	Sulfuric acid
SnO_2	Tin oxide

$Ti(OC_3H_7)_2(C_5H_7O_2)_2$	Titanium diisopropoxide bis(acetylacetonate) (DIPBAT)
TiO_2	Titanium dioxide (Titania)
$Ti[OCH(CH_3)_2]_4$	Titanium isopropoxide (TIP)
$Ti[O(CH_2)_3CH_3]_4$	Titanium n-butoxide (TBO)
C_7H_8	Toluene
$Al_2(CH_3)_6$	Trimethyl aluminum (TMA)
H_2O	Water
ZrO_2	Zirconium Dioxide (Zirconia)
$C_{16}H_{36}O_4Zr$	Zirconium n-butoxide (ZBO)

Preface

This dissertation is an original, unpublished intellectual and independent work by the author, A. Pasche. The synthesis of titanium dioxide nanoparticles using supercritical carbon dioxide and gas-expanded solvents was performed in collaboration with the Laboratoire de Génie Chimique (LGC) at the Université de Toulouse in France. None of the text of the dissertation is taken directly from previously published or collaborative articles. High-resolution transmission electron microscopy was performed at the Canadian Centre for Electron Microscopy at McMaster University in Hamilton, Ontario. X-ray photoelectron spectroscopy was performed at Surface Science Western in London, Ontario. All other experiments and characterizations were performed at Western University in London, Ontario.

I performed all experiments and wrote the manuscript.

Chapter 1

1   Introduction

1.1   Solar Energy and the Photovoltaics Industry

A few years ago, it was released that the world is using energy at a rate of 16 terawatts – 16 trillion (10^{12}) watts – annually[1]. Over 85 percent of that energy is obtained from limited fossil fuel-based resources[2] at the expense of increased CO_2 emissions and the consequent severe changes in climate. The world's population is also increasing: the United Nations Department of Economic and Social Affairs estimates that there could be almost 9 billion people in the world by 2050. More people means more energy consumption. These alarming statistics of increasing energy demand and depleting fossil fuels necessitate a solution towards supplying this additional energy using a cleaner and more sustainable approach.

The idea of powering the earth with the sunlight it receives is a promising solution towards bridging the gap between energy supply and our ever-growing energy demand. Although fossil fuels will undoubtedly continue to represent a large portion of the global energy picture for the next 30 years, any long-term solution must include alternative energy technologies. Solar energy is the most abundant energy source available to us. In fact, the sun is so powerful that if we were able to harness all of its energy, it could provide almost 10,000 times as much energy as the world will ever need[1]. The integration of solar energy into our energy-infrastructure is therefore crucial in order to meet the growing energy demand of the future, and the development of devices that can convert solar energy into electricity more efficiently is one of the most pressing challenges for clean, renewable energy.

Photovoltaic (PV) technology is concerned with harnessing the sun's energy and converting it into useable electric energy, or electricity. In the last decade, the PV industry has experienced declining costs and exponential growth, with worldwide

installed PV capacity rapidly approaching the 200 gigawatts (GW) mark, which is enough to supply 1 percent of global electricity demand[3].

There are several branches of PV technology, differentiated by the type of material used in the cell's photoactive layer. Figure 1.1 illustrates a breakdown of current PV cell technology.
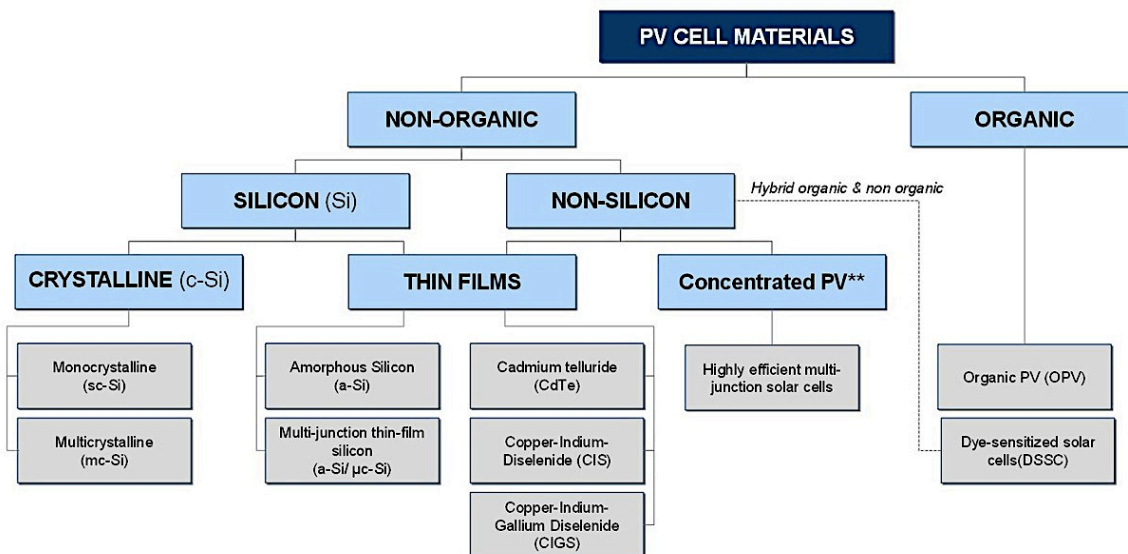
Figure 1.1: Classification of Solar PV Cells. Source: IPCC (2011), Special Report on Renewable Energy[4].

To date, silicon-based technologies have dominated the solar market by almost 90%[5,6]. Silicon (Si) is very favorable as a PV material; not only is it one of the most abundant elements in the earth's crust, but it is also an elemental semiconductor whose bandgap is nearly an ideal match to the solar spectrum[7]. Si-based cells exhibit the highest cell efficiencies (14-22%)[8-11] and have a longer lifespan than other technologies. However, the major drawbacks involved in fabricating Si-based solar cells are their high production costs, large energy consumption, and pollution, due to the high quality and thick layers of crystalline Si required for high performance[12].

Recently, nanomaterials have allowed for other types of solar cells to make their mark in the industry, which gives rise to the breadth of PV materials seen in Figure 1.1. Although Si cells still dominate in terms of production, thin-film solar cells are becoming a prime candidate for future photovoltaics, as they have the potential to significantly reduce production and manufacturing costs, for example, due to roll-to-roll production possibilities[13–15]. For instance, a particular class of thin film solar cell, called a dye-sensitized solar cell (DSSC), can be fabricated from inexpensive, abundant oxide nanoparticles. Despite their current lower efficiencies, the production of DSSCs avoids the expensive vacuum- and high-temperature-processing steps required for single crystal Si production, and can also be tailored for low-light or indoor light harvesting. This class of PV technology will be the focus of this dissertation.

1.2   Dye-Sensitized Solar Cells

Biomimicry is an approach to innovation that tries to design nature-inspired solutions to complex human problems. A dye-sensitized solar cell (DSSC) is a prime example of a biomimetic system, which tries to imitate the photosynthetic process in plants of converting sunlight into useful energy. DSSCs were first introduced by Grätzel and O'Regan in 1991 while studying photosynthesis and the photo-oxidation of chlorophyll, and how this process could be adapted to produce electricity from solar cells. Their device was based on a mesoporous nanocrystalline titania electrode sensitized to visible light by the adsorption of a ruthenium dye in the presence of an iodide/iodine redox electrolyte[16]. They achieved a light-to-electric energy conversion yield of 7%. Over the last two decades, reported cell efficiencies have gradually improved: values of up to 13% have been reported[17], though the certified value of 11.9%[18] was achieved by Japan's National Institute of Advanced Industrial Science and Technology.

DSSCs are regarded as one of the most promising solar cells among third-generation PV technologies, particularly due to their low cost, easy preparation, and minor environmental impact with respect to earlier-generation devices[18,19]. Although their

energy conversion efficiencies are not on par with commercially available PV cells[20], advances in their design[21,22], their incorporation onto flexible substrates[23–26] and their scalable fabrication techniques[14,27] have allowed DSSCs to move from the laboratory to real-life applications.

1.2.1 Structure and Operational Principle of a Dye-sensitized Cell

The working principle of solar cells varies slightly among the different types of PV cells. Nonetheless, all PV devices undergo the same two important steps to convert sunlight into electrical energy: radiation absorption via electrical excitation and charge carrier separation.

The most common solar cells are made with doped silicon, and are based on p-n junctions. When a traditional Si solar cell is exposed to sunlight, photogenerated electron-hole pairs are separated due to the internal electric field created by the p-n junction. Electrons migrate towards the front electrode and holes towards the back electrode, and electric current is created when the electrons flow through a wire that joins the two electrodes. Figure 1.2 shows the different layers of a conventional Si PV cell and how flowing electrons generate electric current.
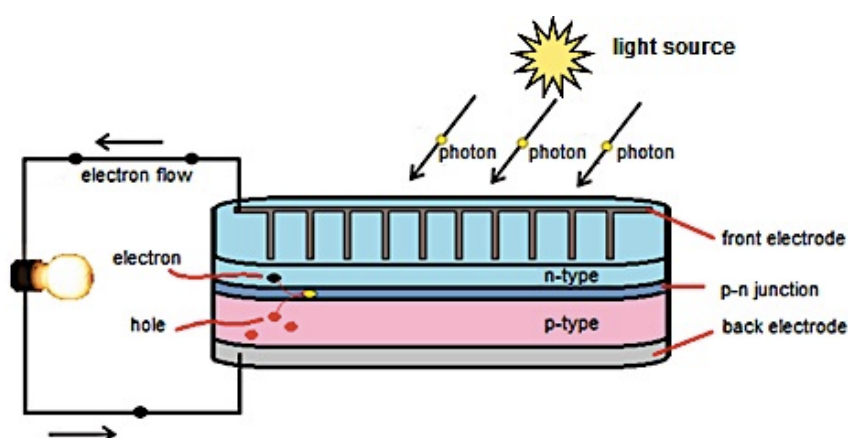
Figure 1.2: Layers and working principle of a conventional silicon solar cell[28].

DSSCs work much in the same way as conventional PV cells, only that the semiconductor is based on a photoelectrochemical system instead of silicon. A DSSC consists of a dye sensitizer, a nanocrystalline semiconductor film, an electrolyte, and a counter electrode (CE). The working electrode (WE) is composed of a mesoporous metal oxide semiconductor film coated onto a conducting glass substrate. The film is then sensitized with a dye for light absorption. The pores of the semiconductor film are permeated with an electrolyte that contains a redox couple, and the cell is sealed with a CE. These four major components are explained in further detail below.

Dye sensitizer

A dye is the light-active component of a DSSC that is chemically adsorbed onto the semiconducting material of the device. Due to the varieties of sensitizers that are available[13,29,30] and the possibility of panchromatic light absorption using co-sensitization[29,31,32], DSSCs have the potential to absorb energy from a broader light spectrum than conventional, Si-based solar cells. Figure 1.3 shows several WE's before being assembled into DSSCs. Different colored dyes will absorb different areas of the solar spectrum. Typical dyes are based on ruthenium(II)-polypyridyl complexes[19].
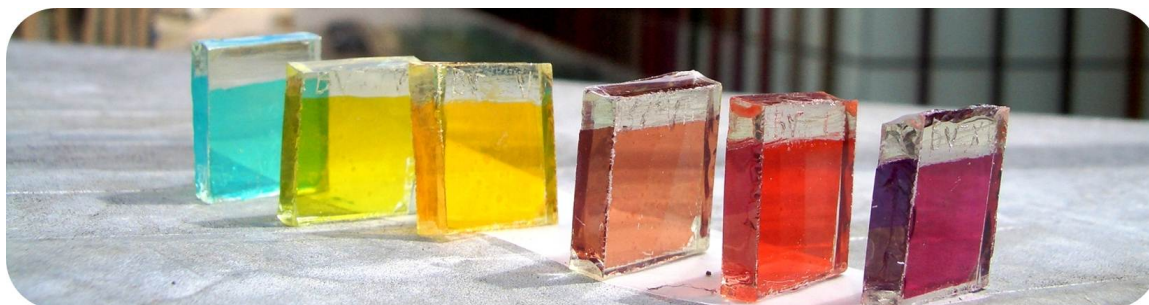
Figure 1.3: Working Electrodes containing various dyes, before being assembled into DSSCs. (Image source: www.thesolarspark.co.uk)

Semiconductor

The semiconducting material is composed of fused titanium dioxide (TiO_2) nanoparticles (NPs), creating a semi-transparent film with thicknesses ranging from 3-20μm[15]. The TiO_2 is mesoporous, meaning that the interconnected NPs create pores with diameters in the range of 2 to 50nm[33], in turn providing an internal surface area. The NPs are crystalline to allow for efficient electron mobility[34]. Since the dye, which is responsible for light harvesting, is chemically adsorbed onto the surface of the TiO_2, NPs provide a high specific surface area that allows for maximal photoabsorption.

Electrolyte

The basic function of the electrolyte is the regeneration of the dye and itself. More specifically, it acts as a charge carrier, or a shuttle, between the CE and the dye, and it creates a stable interfacial contact with the dye-TiO_2. An electrolyte should present good charge mobility, be thermally and photochemicaly stable, and should not absorb in the visible spectrum to avoid competition with dye molecules. The conventionally used electrolyte is based on an iodide/triiodide ($3I^-/I_3^-$) redox couple. Its charge transport is mainly attributed to the exchange reaction of $I^- + I_3^- \rightarrow I_3^- + I^-$ instead of the diffusion or migration of the redox couple itself[35], which ensures a fast reaction rate. During cell fabrication, the liquid electrolyte interpenetrates the dye-coated TiO_2 nanoparticles.

Counter Electrode

The CE is made of an ITO or FTO conductive glass sheet coated with an electrocatalyst, typically platinum (Pt)[13], to facilitate the redox couple regeneration reaction and the collection of electrons from the external circuit. With regard to device cost, a Pt CE is the most expensive component in DSSCs.

Figure 1.4 illustrates the device structure and operational principle of a typical DSSC. When the cell is exposed to light, (1) the dye absorbs the incident photons and promotes an electron to an excited state, which is then (2) injected into the conduction band (CB) of the TiO_2 semiconductor. (3) The electron diffuses towards the current collector (FTO) and flows through the external circuit towards the CE to do work. Meanwhile, (4) the

oxidized dye molecule is regenerated with an electron donated from the electrolyte (iodide, I⁻), returning the dye to its ground state. Finally, this regenerative cycle is completed when (5) triiodide is reduced to iodide at the Pt CE. This continuous process occurs billions of times per second within the cell, and is how electricity is generated from a DSSC. Overall, the device generates electric power from light without suffering from any permanent chemical transformation.
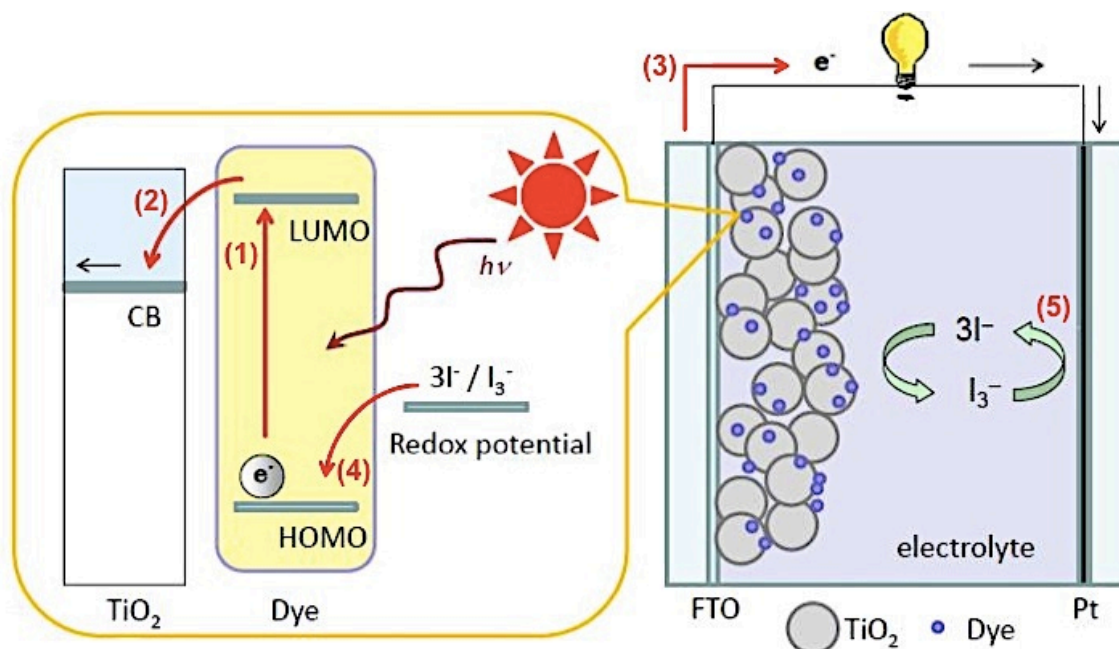
Figure 1.4: Working principle of a dye-sensitized solar cell[30].

In conventional Si cells, light absorption and charge transport occur in the same material (see Figure 1.2). In DSSCs however, these fundamental processes occur in different components of the cell (see Figure 1.4); here, the bulk of the semiconductor (TiO_2) is used solely for charge transport while the photoelectrons are separately provided by the photosensitive dye. This reduces the possibility of premature recombination of electrons and holes, which would impede current flow. As these processes do not happen in the same material, ultrapure materials are therefore not required for a high-performance DSSC[36]. This type of thin-film solar cell is thus a technically and economically viable alternative to traditional p-n junction Si solar cells.

1.2.2 Characterization of Solar Cells

The performance of a solar cell is qualified by how efficiently it can convert sunlight into electricity. A cell's current-voltage (IV) behavior is characterized under simulated solar illumination. The key parameters characterizing a cell's performance are discussed below.

Open Circuit Voltage (V_{OC})

When a photon with energy equal to or higher than the absorber's band gap is absorbed, the photogenerated electron moves to the anode and the hole to the cathode. With the accumulation of charges at the contacts, a photovoltage builds up. The V_{OC}, measured in volts (V), is the maximum voltage available from a cell, and occurs when the net current through the device is zero. When there is no current, this means that charge carriers are accumulating at the contacts, but are not being extracted. This parameter is essentially an indication of the amount of charge carriers that can be generated, and is analogous to the maximum pressure that a water system can hold.

Short Circuit Current (I_{SC})

The I_{SC} is the maximum current through a cell when the voltage across the device is zero (i.e. when the solar cell is short-circuited). This is the current value at which there is no charge accumulation at the contacts, where any charge carrier being created is being extracted (rate of accumulation = rate of extraction at contacts). This parameter is an indication of the number of charge carriers that can be extracted from the cell. Typical values are in milliamps (mA). The current density, J_{SC}, measured in mA/cm^2, is obtained by dividing the current by the cell's photoactive surface area. It is useful when comparing performances from literature, as cell dimensions and photoactive areas may vary.

Fill Factor (FF)

The FF is a parameter, which, in conjunction with V_{OC} and I_{SC}, determines the maximum power that can be extracted from a solar cell. It reflects the electrical (ohmic) and electrochemical (overvoltage) losses occurring during operation. More specifically, it is

the ratio of the maximum obtainable power ($V_{max}I_{max} = P_{max}$) to the product of the V_{OC} and I_{SC}, and is defined by the following equation:

$$FF = \frac{V_{Max} I_{Max}}{V_{OC} I_{SC}} = \frac{P_{Max}}{V_{OC} I_{SC}}$$

(eq. 1.1)

The FF is affected by all the components of this equation. A low V_{OC} indicates a poor electron-hole separation rate. A low I_{SC} indicates a high recombination rate. Consequently, a fill factor is difficult to optimize. Graphically, the FF is a measure of the "squareness" of the cell's IV profile, and is also the area of the largest rectangle that can fit within that IV curve. The IV curves of both high- and low-FF solar cells are illustrated in Figure 1.5. Both IV curves illustrated hold the same V_{OC} and I_{SC}, yet the lower-FF cell produces less power at its maximum power point compared to the higher-FF cell. Typical commercial solar cells have a FF above 0.7, while intermediate-grade cells will usually have a FF between 0.4 and 0.7[37].
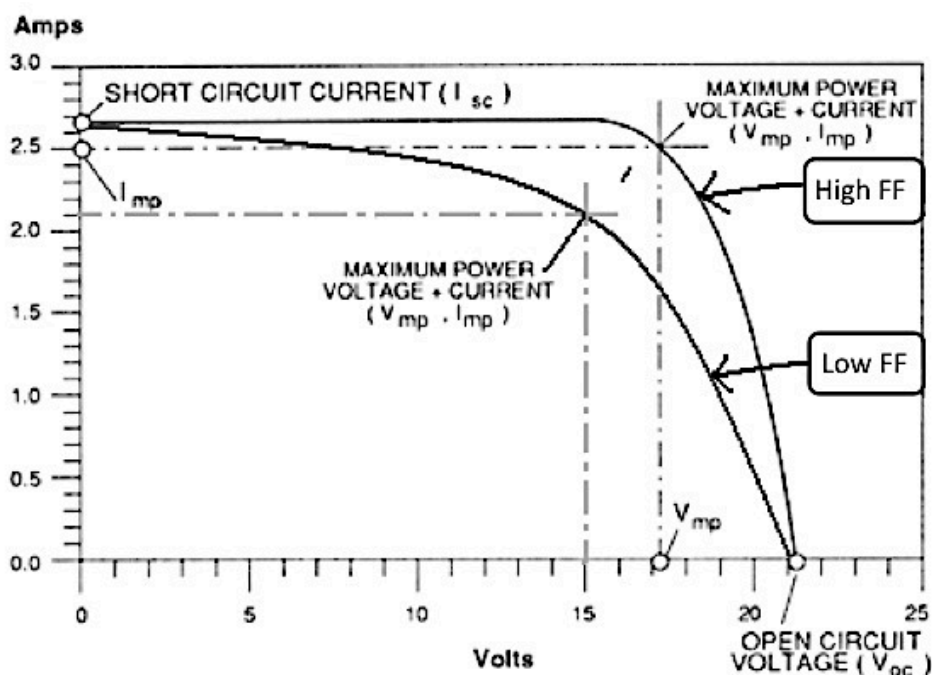
Figure 1.5: IV curves of two different solar cells demonstrating varying fill factors[38]. The FF expresses the "squareness" of a curve. The V_{OC} and the I_{SC} are also indicated.

This parameter is an indication of carrier transport efficiency. A low FF suggests that there is significant resistance in the cell, or that the carrier mobility is low. Inefficient carrier transport means that more voltage is needed to move the same amount of charge as would be needed in a cell with a higher FF. This essentially 'wastes' voltage to move carriers around, which could be compared to the analogy of driving a car with the emergency-parking break on (lower FF) as opposed to with it off (higher FF).

Power Conversion Efficiency (PCE)

A cell's overall performance is determined by its sunlight-to-electric power conversion efficiency (PCE). The PCE is characterized by measuring the current density as the voltage across the device is biased with variable load during device irradiation by light. The PCE is related to the short-circuit current density (J_{SC}) and the open circuit voltage (V_{OC}) by

$$PCE = \frac{P_{max}}{P_{in}} = \frac{J_{SC}\ V_{OC}\ FF}{P_{in}} \qquad \text{(eq. 1.2)}$$

where P_{in} is the incoming light's power density.

Another important parameter is the external quantum efficiency (EQE), which corresponds to the photocurrent density produced in the external circuit under monochromatic illumination of the cell divided by the photon flux that strikes the cell. The EQE as a function of wavelength can be expressed as follows:

$$EQE\ =\ LHE(\lambda)\Phi_{inj}\eta_{coll}\ =\ 1240\left(\frac{J_{SC}}{\lambda\phi}\right)\ =\ 1240\left(\frac{J_{SC}}{\lambda P_{in}}\right) \qquad \text{(eq. 1.3)}$$

where LHE (λ) is the incident light-harvesting efficiency for photons with wavelength λ (nm), Φ_{inj} is the quantum yield for electron injection from the excited dye in the conduction band of TiO_2, J_{SC} is the photocurrent density produced in the external circuit (mA/cm^2), η_{coll} is the charge collection efficiency, ϕ is the incident light flux, and P_{in} is the incident light intensity (mW/cm^2). EQE values provide practical information about

how well a solar cell is absorbing light at a specific λ. This parameter includes the effects of optical losses such as transmission and reflection.

1.2.3 Current and Future Applications of DSSCs

DSSCs are being developed in pilot plants and are already being commercialized by companies such as Dyesol, G24i, Sony, Sharp, Konarka and Heliatek. They are especially suited for building- and automobile-integrated photovoltaics (BIPV, AIPV) as well as portable or indoor light harvesting applications due to their workability under low-light conditions. In fact, DSSC panels have been shown to deliver even more electricity than their silicon and thin-film counterparts of similar power ratings when exposed to low light operating conditions and at higher temperatures[13,27,30]. Therefore, they are potential market leaders in BIPV and indoor light harvesting PV technology. The SwissTech Convention Center on the EPFL's campus in Lausanne, Switzerland was recently renovated to include a semitransparent façade composed of large DSSC panels of various colours (Figure 1.6a,b).

Although this technology has lower module efficiencies, their cost per Watt is estimated to be three to four times lower than conventional Si systems[39]. They also possess many features that motivate their further development, including their transparency, flexibility, conformability, and light weight. These attractive features allow us to be creative and innovative in their design, and their integration into different products opens up new commercial opportunities. Examples of existing products that have integrated DSSCs are shown in Figure 1.6c-e. These include remote controls, computer keyboards, smoke alarms and even wearable electronics such as bag packs and watches.

In a broader context, these modern devices have opened up new opportunities for economic development, providing a low-cost alternative for people without access to a centralized power grid and who cannot afford the high up-front costs of 1st and 2nd generation solar cells.
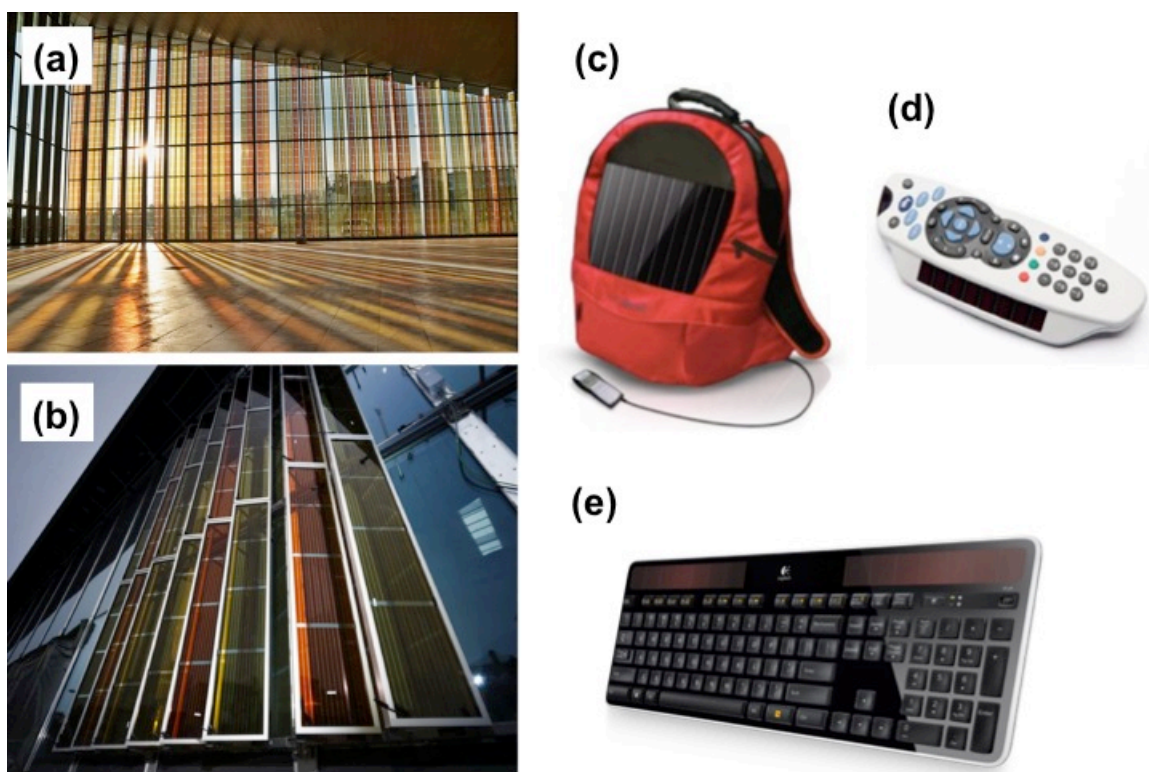
Figure 1.6: Examples of current DSSC applicaitons; (a, b) The SwissTech convention center's semitransparent façade on the EPFL campus in Lausanne, Switzerland, formed by large DSSC panels made by Solaronix (photo courtesy of Solaronix), (c, d, e) Commercial DSSC products available on the market: (c) Back pack equipped with a G24 Innovations flexible DSSC panel, (d) Remote control with a G24 Innovations DSSC panel, and (e) Logitech K750 Wireless Solar Keyboard with integrated DSSCs.

With DSSCs able to be cheap, versatile, printable and coloured, there is potential to design environmentally friendly gadgets that go with our decorating tastes and fit in seamlessly with the lifestyle we are used to. An ideal future will see everyday objects such as clothing, cars and even roads themselves turned into power-generating solar collectors. Although there is still need for improvement to achieve high performance DSSCs, their positive inherent features will facilitate their entry into the PV market.

1.3   Localized Surface Plasmons

A surface plasmon is a physical phenomenon that takes place in metal crystals when their electrons interact with an electromagnetic field. More specifically, it is the light-induced collective oscillation of free charge carriers at the interface between a dielectric material and a metal. When the metal is in the form of nanoparticles, these oscillations are referred to as *localized* surface plasmons (LSPs). In this geometry (Figure 1.7), the electric field of an incoming light wave induces a polarization of the free conduction electrons – a shift of electrons from their ionic core, which is relatively much heavier. This generates a restoring electric field to re-establish local electric neutrality. The combination of this restorative spring action with the inertia of electron mass leads to a collective harmonic oscillation[40]. The plasmon wave mainly presents a dipolar character (for particles up to a certain size), with its period being dependent on the particle size.
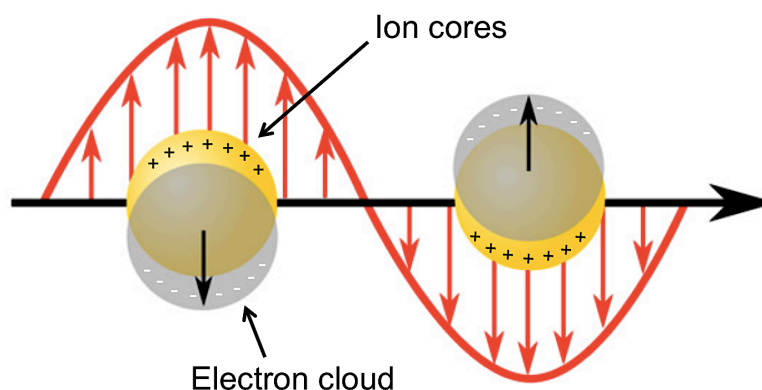
Figure 1.7: Schematic demonstrating the effect of an external oscillating electric field on the electron clouds in spherical metal nanoparticles. Incident electromagnetic radiation (red) displaces the free electron cloud, which then experiences a restoring force exerted by the positively charged ion cores. The collective electron density oscillation is defined as a localized surface plasmon (LSP).

The coherent oscillation of incoming light waves with the frequency of electron density oscillations is called localized surface plasmon *resonance* (LSPR). Two unique opto-electric properties arise from the resonance of LSPs with incident light:

1. **Amplification of electric field**: The electric field near the metal NP's surface is greatly enhanced. This corresponds to the coherent superposition of electromagnetic oscillations and the metal's electron density fluctuation[41]. This field is highly localized at the NP surface and decays rapidly away from the NP/dieletric interface into the dielectric background.

2. **Enhanced far-field scattering**: Plasmonic NPs have very good scattering capabilities, with scattering efficiency increasing with particle size. The scattering of light causes multiple reflections and redirections of photons between nanocrystals, increasing the average path length of photons in the medium.

All metal NPs exhibit LSPs, because they all have free conduction electrons. Figure 1.8a lists a selection of metals and the frequency range at which they experience LSPR. For the purpose of solar energy harvesting, oscillations that correspond to optical frequencies (400-700 nm) are of interest. Silver (Ag) and gold (Au) are examples of metals that exhibit strong LSPR in the visible range of the solar spectrum. That is, under illumination, their electronic oscillations resonate with the frequency of incident visible light, resulting in a huge increase in the intensity of the electric field and a strong confinement of the field. The wavelength at which the frequency of light matches plasmon frequencies is called the LSP resonance wavelength (λ_{LSPR}). Figure 1.8b shows a simulation demonstrating the local field enhancement around a Au NP embedded in a medium with a refractive index of n=1.5. A dipole resonance mode can be seen, which is expected for a particle of this size.
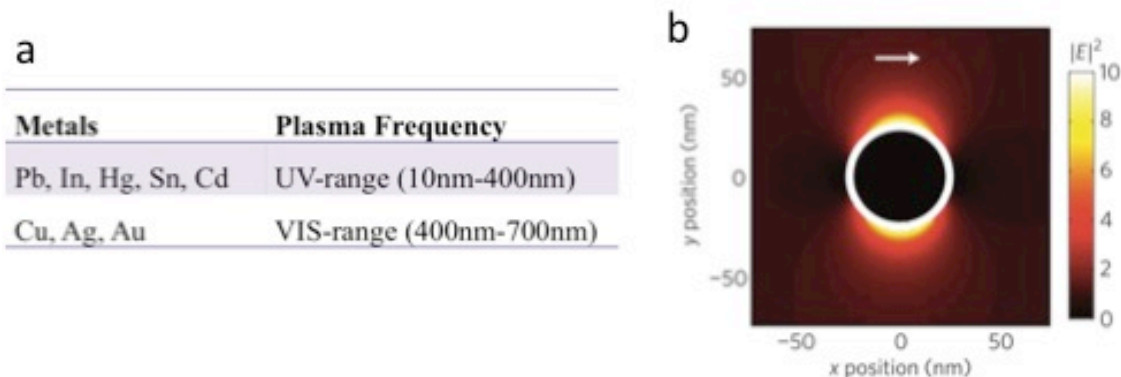
Figure 1.8: a) Various metals exhibiting LSPR at certain frequencies. For the purpose of solar energy harvesting, oscillations corresponding to optical frequencies are of interest. b) Simulation demonstrating electric field amplitude patterns for a 50-nm Au NP when irradiated at 500 nm, reproduced from Atwater *et al.*[40] The refractive index of the surrounding medium is 1.5. The magnitude of the electric field intensity E is indicated by the colour scale.

1.3.1 Incorporating Plasmon Nanoparticles into DSSCs

Plasmonic NPs can enhance the light absorption capability of their surrounding environment. Their unique optical properties can be exploited to improve the light absorption of dye molecules in DSSCs.

Upon integration into a DSSC, the strong local field enhancement of metal NPs under resonant conditions could be exploited by creating an antenna effect for incident sunlight. The charge separation in the surrounding dye molecules could then be significantly enhanced since the rate of electron excitation in the dye is proportional to the local light intensity[42]. The far field scattering effect of LSPR can also be used advantageously: metal NPs incorporated into the DSSC's photoactive layer could essentially act as nano-mirrors, increasing the optical path length. That is, during light irradiation, photons not initially absorbed by dye could be scattered by the metal NPs, effectively giving those photons multiple opportunities to pass through the photoactive layer and get absorbed by the dye. Improving photon absorption can improve a cell's photocurrent, and therefore it's efficiency.

Integrating metallic nanostructures into the photoactive cell layer and taking advantage of their resonance with incoming light is therefore an effective way to increase light absorption in DSSCs. Plasmon excitation and light localization effects can be used advantageously to improve photovoltaic efficiency. These effects can also lead to new solar cell designs with smaller semiconductor thicknesses and thus lower material costs[43].

1.4 Supercritical Fluids and Supercritical CO_2

In an age where pollution awareness is ubiquitous and environmental regulations are becoming increasingly stringent, supercritical fluids (SCFs) are quickly acquiring the role of alternative solvents to eventually substitute harmful chemicals. SCFs exhibit a range of unique properties that can be exploited for material processing and chemical reactions that would typically require the use of harsh solvents or volatile organic compounds.

Thermodynamically, a fluid reaches a supercritical state when both its temperature and pressure are above their critical values, T_C and P_C. Figure 1.9 shows a phase diagram for a typical material, where the supercritical region (shown in yellow) begins at the critical point (T_C, P_C). A fluid in the supercritical region exhibits liquid-like density, which enables it to function as a solvent, and gas-like viscosity and diffusivity, which provide superior mass and heat-transfer compared to a conventional solvent.
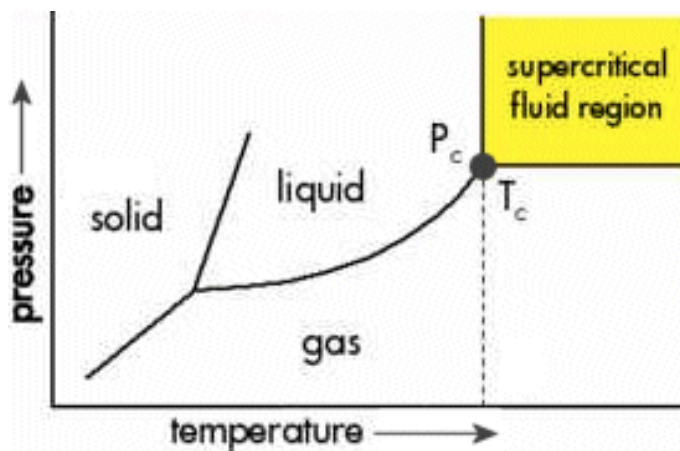
Figure 1.9: Schematic of a typical material's phase diagram. (Source: NASA – Harvesting Mars)

All fluids have a critical point, but only a few are deemed suitable for supercritical applications. Factors that contribute to a material's practicality as a SCF include their toxicity, cost, availability, environmental compatibility, and whether their critical values are easily achievable. CO_2 is a great SCF candidate because it meets all these criteria.

When CO_2 is compressed to a pressure of 73 atm and heated to 31.1 ºC, it becomes a supercritical fluid. It is an extremely useful solvent because its solubility can be effectively manipulated by varying its temperature and/or pressure, making it easy to recover material that has been dissolved. For instance, using supercritical CO_2 (scCO_2) as a co-solvent has been used for careful particle size control in a number of syntheses[44–46]. Particles of a desired size can be recovered by lowering the pressure of the CO_2, which causes the product to drop out.

1.4.1 Synthesis of TiO_2 in scCO_2

Although the sol-gel process is known for its control over the properties of its products, the solvents used are often deemed harmful to the environment. Supercritical CO_2 as a co-solvent offers the same control over product properties as harsher solvents do, with the added benefit of being ecofriendly and recoverable after reactions[47,48]. It also offers tunable polarity across a large range, which is advantageous for dissolving reactants and can control the degree of nanoparticle agglomeration during synthesis. The products can also be achieved at lower temperatures.

The literature shows that the direct sol-gel process in scCO_2 is a promising technique for synthesizing metal oxide nanomaterials[44,49,50]. Integrating this green chemical process as a step in the fabrication of DSSCs would further the sustainability of this technology, and encourage the development of an entirely green production process for nanomaterials that are required for next-generation advanced functional devices similar to DSSCs. In this thesis, the synthesis of TiO_2 was attempted using supercritical CO_2 as a co-solvent to compare the metal oxide's properties and performance in a DSSC to those of TiO_2 synthesized via the conventional sol-gel method. This study also used green bio-sourced

solvents coupled with scCO$_2$ to prepare TiO$_2$ nanoparticles, with the hope of encouraging the development of cleaner processes for nanomaterials used in DSSCs.

Chapter 2

2   Literature Review and Motivation

The progress of any PV technology hinges on three criteria: increasing light-to-electric energy conversion efficiency, improving long-term stability, and decreasing device cost. Although DSSCs have low production costs[13,24,51] and have shown great progress in design & materials composition to improve their stability[15,52], their main limitation is that their efficiencies are not on par with more established PV technologies[20]. Figure 2.1 shows the estimated annual generation of solar power by type of PV technology. From this figure, it is evident that Si-based cells remain the dominant force in the solar energy market (shown in orange, yellow and red). DSSC technology, shown in white, has a very small presence.
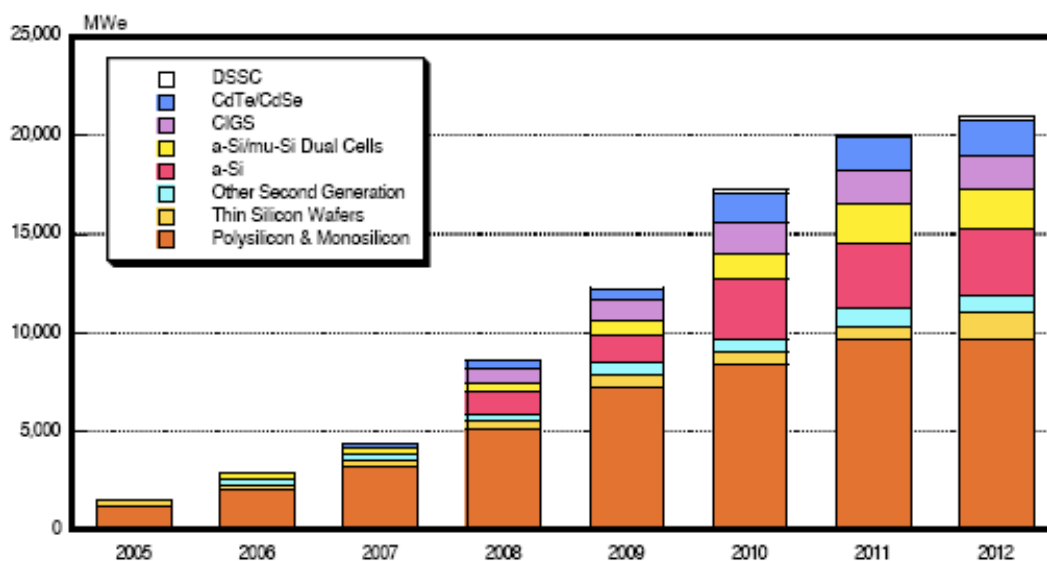
Figure 2.1: Estimated generation of solar power by type of PV technology[53]. DSSCs (white) have a very small contribution due to their relatively low efficiency in relation to Si technologies.

One of the biggest contributors to efficiency loss in DSSCs is inefficient sunlight absorption[40]. The sun emits photons of a wide range of energies because electromagnetic

radiation is made up of a range of different wavelengths. Unfortunately, most photoabsorbing materials possess unbalanced light harvesting (LH) across the solar spectrum[30]. In DSSCs, the dye that sensitizes TiO_2 NPs doesn't respond equally to all the wavelengths that make up the visible spectrum, limiting the amount of photons that can be converted into electricity. This can be seen in Figure 2.2a, where solar energy is strongly absorbed at λ_{Hi} (400-600 nm) and poorly absorbed at λ_{Lo} (600-800 nm). Some of the photons that hit the cell won't have enough energy to separate an electron-hole pair, and will simply pass through the cell as if it were transparent (Figure 2.2b).
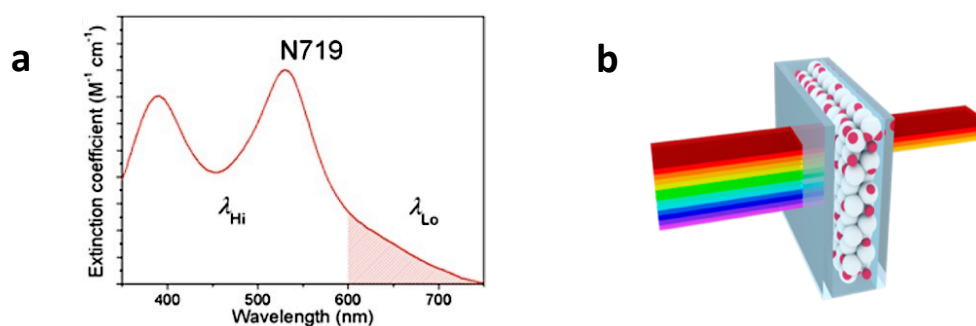
Figure 2.2: a) Extinction coefficient of N719, a commonly used dye in conventional DSSCs. The shaded area is the weak LH region (usually red-NIR), which requires thicker photoactive layers to more efficiently utilize solar energy; b) Schematic diagram of a DSSC inefficiently absorbing longer-wavelength (lower energy) light[54].

Over the last two decades, there has been significant progress in the design and materials composition of DSSCs to improve their light harvesting capabilities, particularly in the field of plasmonics. The following chapter describes recent progress in plasmon-enhanced sunlight absorption research, and the need for further improvements that motivate this thesis work.

2.1 Silver Plasmon nanoparticles

Factors that are critical for the improved performance of a cell include efficient photon absorption, fast electron transport and reduced charge recombination. Plasmonic NPs (p-NPs) have been drawing much attention due to their unique optical properties that contribute to effective charge collection and charge transport. Ag NPs lend themselves particularly useful due to their resonance wavelength being within the visible range of the solar spectrum[43,54–56], and several examples have been published that demonstrate enhanced photocurrents owing to their absorptive and scattering capabilities. For instance, significant absorption enhancement using Ag NPs has been observed for both thin-film and wafer-based Si solar cells[57]. Enhanced efficiencies have also been demonstrated in organic solar cells doped with Ag nanoclusters[58]. More recently, DSSCs have also been enhanced by embedding small Ag NPs within the photoactive layer[43,56,59,60]. Qi et al.[43] investigated the effects of LSPR on the performance of DSSCs by incorporating core-shell Ag-TiO_2 nanostructures (Figure 2.3a) into conventional TiO_2 photoanodes. They demonstrated that the light absorption of dye molecules was enhanced by the strong localized EF generated by LSPR. Figure 2.3b compares the I-V curves of plasmon-enhanced and TiO_2-only DSSCs having the same photoanode thickness.
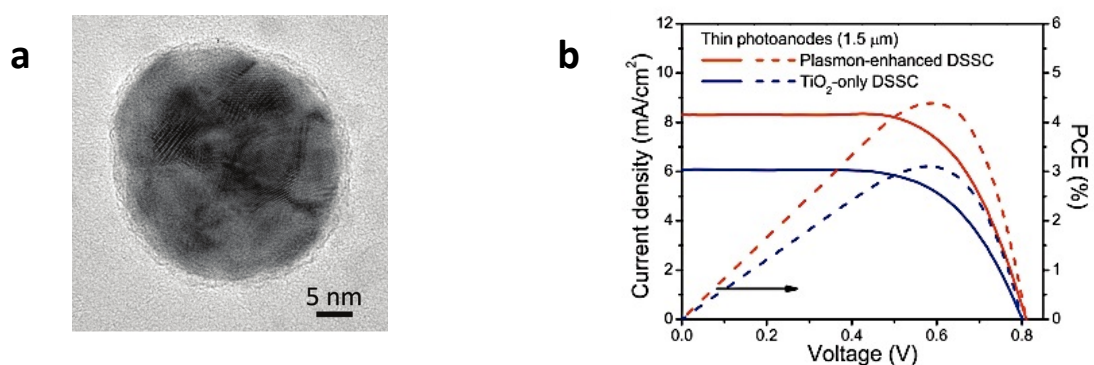
Figure 2.3: a) HRTEM image of an individual Ag-TiO_2 NP with the lattice fringes of Ag crystalline structure and an amorphous TiO_2 shell about 2nm thick; b) Current density (solid lines) and PCE (dashed lines) of a plasmon-enhanced DSSC (Ag/TiO_2=0.6 wt%, PCE=4.4%) and TiO_2-only DSSC (PCE=3.1%) with the same photoanode thickness of 1.5um[43].

Incorporating these Ag-TiO$_2$ NPs into their DSSCs increased the PCE by 42%, a direct correlation to the increased photocurrent, corresponding to enhanced dye absorption. However, they noticed a decrease in PCE when the concentration of plasmonic-NPs exceeded 0.6 weight %, due to them losing too much incident solar power to thermal energy. Other sources also report having observed doping limits when incorporating plasmonic nanostructures into their photoactive systems[56,61,62], or simply do not attempt doping concentrations above 1%. There are very few studies addressing the mitigation of plasmonic-NP doping limits, and even fewer addressing their effect on the performance of DSSCs. In this thesis, the use of zirconia (ZrO$_2$) as a thermostabilizer in DSSCs is investigated, which is described in further detail in section 2.2.

2.1.1 Plasmonic Design Specifications

Optimization of plasmonic light trapping in a solar cell is a balancing act in which several physical parameters must be taken into account. The resonance wavelength λ_{LSPR} of a plasmonic NP can be tuned by tailoring several parameters such as particle shape, size & orientation, as well as the nature of the surrounding medium[63]. This section describes the proposed NP and active layer designs for plasmon-enhanced DSSCs, and the justification for their specifications.

Ag@TiO$_2$ Nanoparticle Design

A core-shell Ag-TiO$_2$ nanostructure (Ag@TiO$_2$ NPs) is proposed as the plasmonic-NP design. This hybrid core-shell nanostructure is composed of a silver (Ag) core and a titania (TiO$_2$) shell. Ag is an ideal metal for plasmonic light trapping in DSSCs because it exhibits resonance in the visible range of the solar spectrum, and is considerably less expensive than Au. TiO$_2$ was chosen over other insulating material because electrons can be easily transferred to surrounding TiO$_2$ NPs that are in contact with the shell. This material selection essentially disguises the plasmonic-NPs as regular TiO$_2$ NPs in the photoactive layer.

When a metal NP interacts with incident light, both light absorption and light scattering occur, and their sum is characterized as the extinction of light (Figure 2.4). The relative amount of absorption and scattering depends on the size and geometry of the NP. The millennially-cited work of Link *et al.*[62] confirms that as metallic NPs increase in size, incident light shifts from being localized (absorbed) to being scattered during resonance. Briefly, they studied colloidal Au NPs ranging from 10-100 nm in diameter and demonstrated that 15 nm-sized NPs primarily localized an incident EM field while 100-nm particles primarily scattered the incident field.
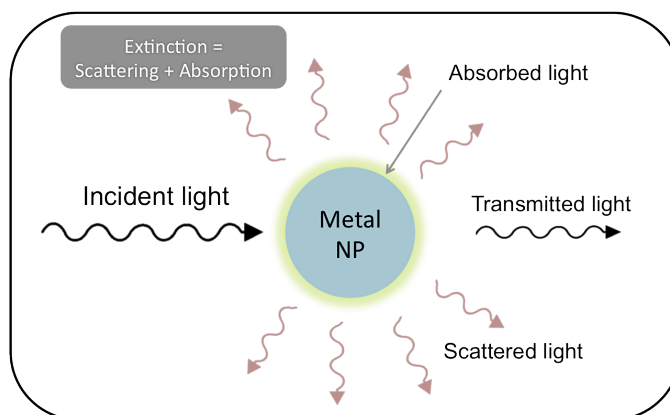
Figure 2.4: Schematic illustration of the interaction of light with a metal NP. The extinguished light is the portion of incident light that does not get transmitted through the particle.

Both of these effects are beneficial for effectively trapping light within the photoactive layer; exploiting the field-localizing behavior of smaller metal NPs increases light absorption, and utilizing the scattering behavior of larger NPs increases the optical path length. To benefit from a combination of these two effects, the size of the plasmonic NPs were chosen to be within this 10-100-nm range.

During cell operation, the Ag NPs cannot be in direct contact with the dye and the electrolyte. Previous geometries that contained metal NPs in direct contact with dye and electrolyte resulted in charge carrier recombination and back reaction of photogenerated electrons[60,64]. A core-shell nanostructure is crucial because it provides an energy barrier between the metal and dye/electrolyte. With a TiO_2 shell surrounding the Ag NP, only the

electrons can go through the shell (Figure 2.5a). The photogenerated holes cannot inject into the TiO$_2$ shell as this is energetically forbidden. A shell structure effectively prevents the photogenerated carriers from recombining at the Ag NPs[65], as shown in Figure 2.5b.
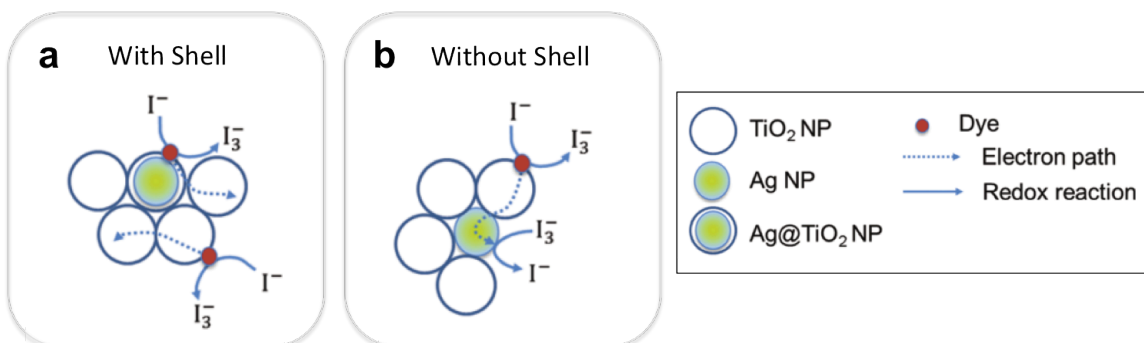
Figure 2.5: Schematic diagrams illustrating the charge transfer mechanism in a DSSC active layer containing a) Ag@TiO$_2$ NPs, and b) Ag NPs. Without a TiO$_2$ shell, there is direct contact between Ag and the electrolyte, and the surface of Ag NPs serves as a recombination site for the photogenerated electrons and the ions in the electrolyte.

The TiO$_2$ shell not only improves the stability of the Ag NPs by preventing their corrosion by the electrolyte, but by also preventing their aggregation during the high-temperature annealing process during cell fabrication. The use of a core-shell structure is therefore an effective way of protecting and isolating the Ag NPs.

The resonance wavelength of Ag@TiO$_2$ NPs can be fine-tuned by varying the thickness of the shell, which alters the dielectric constant of the surrounding matrix. For example small 7-nm Ag NPs in vacuum exhibit LSPR at ~360 nm[66], which can be redshifted in a controlled way across the visible and near-infrared spectral regions by increasing the shell thickness that surrounds them. Nonetheless, the shell thickness still needs to remain thin relative to the core in order to maximize the local field enhancement effect. Awazu *et al.*[67] studied the photocatalytic behavior of silica-coated Ag NPs. They found that the photocatalytic efficiency of the NPs increased with decreasing silica shell thickness, indicating that the induced electric field decreases quickly with increasing distance from the NP. These findings are applied to the proposed Ag@TiO$_2$ design to select an

appropriate shell thickness; a thinner shell corresponds to a stronger localized EF, which means more absorption enhancement for dye molecules surrounding the Ag@TiO$_2$ NPs.

Photoactive cell layer designs

The following photoactive layer designs attempt to concentrate incident light and increase the optical path length of photons by utilizing the unique optoelectronic properties arising from LSP resonance. The two proposed architectures offer different strategies to couple the Ag@TiO$_2$ plasmonic nanocrystals to the photoactive layer of DSSCs to maximize their efficiency.

The 'chocolate-chip' design has Ag@TiO$_2$ NPs distributed throughout the photoactive 'cookie batter' cell layer (Figure 2.6a). The 'blanket-array' design has Ag NPs functionalized onto the photoelectrode, upon which a uniform sheet (blanket) of TiO$_2$ is deposited by atomic layer deposition (ALD). During illumination, this Ag@TiO$_2$-NP array will be on top of the photoactive layer (Figure 2.6b).
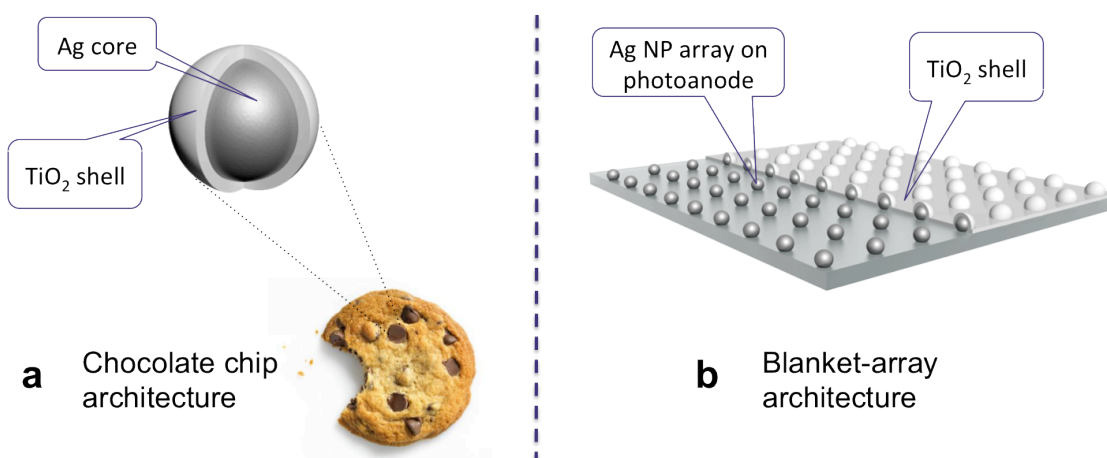
Figure 2.6: Schematic diagrams depicting the proposed active layer designs: a) the 'Chocolate chip' architecture, and b) the Blanket-array architecture.

In the 'chocolate-chip' design, Ag@TiO$_2$ NPs are used primarily as absorption antennas within the DSSC. By efficiently converting free-propagating optical radiation into localized energy, the plasmonic near-field is coupled to the dye, increasing its effective

absorption cross-section. Since the rate of electron excitation in the dye is proportional to the local light intensity[42], this effect encourages the creation of more electron-hole pairs, which should lead to higher photocurrent and thus increased photovoltaic efficiency.

There is now considerable experimental evidence that light scattering from metal NP arrays increases the photocurrent spectral response of thin-film solar cells[60,68]. The Ag@TiO$_2$ NPs in the blanket-array design are used primarily as nano-mirrors to trap freely propagating solar plane waves by essentially folding the light into the TiO$_2$ absorbing layer. When p-NPs are positioned at an interface between two dielectrics, light will scatter preferentially into the dielectric with the larger permittivity[69]. According to this configuration (see Figure 3.6), the permittivity of TiO$_2$ (ε~100[70,71]) is higher than that of the polymer (P4VP-10) (ε~2.56[72]) binding the Ag NPs to the electrode. Light is therefore preferentially scattered into the TiO$_2$ thin film and will acquire an angular spread in the absorbing layer, which should effectively increase the optical path length in the cell. Furthermore, since these Ag NPs will be larger than in the first design, increased scattering can be expected[62]. The scattering cross-sections can reach as high as ten times the geometrical area[68,73], and so ~10% coverage of the photoanode would therefore be enough to capture the majority of the incident sunlight by plasmonic excitations.

These active cell layer designs hold features that make them promising candidates for plasmon-enhanced DSSC designs. In both architectures, the amplification of electric field near the Ag NPs' surface and the increased scattering within the active layer increase the amount of dye molecules reached by light. This thesis work aims to determine which of the two designs yield a better overall cell performance.

2.2   Zirconia as a Thermostabilizer

When a DSSC's photoactive material is illuminated, the energy removed from the incident light is either scattered, or locally absorbed. The dissipation of energy due to absorption may give rise to a number of secondary effects, including local heat production. One of the assumptions of the Shockley-Queisser limit[74] is that excited electrons created by high-energy photons are immediately relaxed to the band edge – that is, the fraction of energy of photons with energy greater than the bandgap is immediately lost as heat, a phenomenon referred to as thermalization. This means we can always expect to have some temperature increase in the cell.

Although plasmonic nanostructures have shown to amplify photoabsorption in DSSCs, there is a limitation to their enhancement capabilities because their resonance with incoming light also releases heat, which further contributes to local heating in the cell. The electronic oscillations under resonant conditions can create a local electric field up to $\sim 10^3$ times the incident field[75,76] and the local temperature on the plasmonic NPs' surface may exceed 500 °C[63]. This excessive heat can lead to cell degradation, an unfavorable effect that has been identified in literature[43,56,63]. For example, Qi $et\ al.$[43] observed a decrease in PCE when the concentration of Ag-TiO$_2$ NPs in their DSSCs exceeded 0.6 weight %, a result of the p-NPs losing too much incident solar power to thermal energy. This effect poses a doping limit to the amount of p-NPs that can be incorporated into conventional photoanodes, thus imposing a limit on the cell's absorption improvement.

According to several studies[77–81], a small amount of transition metal doping has been found very effective in improving the thermal stability and activity of TiO$_2$. Zirconia (ZrO$_2$) is one of these suitable dopants, known to have very high thermostabilizing properties[82,83]. It has one of the highest dielectric constants for metallic oxides[84] and therefore exhibits good optical properties. Additionally, it is very chemically stable due to its multi-electronic configuration, including its d-orbital electrons, characteristic of transition metals. Ti and Zr are also in the same group of elements (IVB), which gives them comparable physicochemical properties.

The use of ZrO_2 as a thermostabilizer in plasmon-enhanced DSSCs has yet to be investigated, but there is plenty of evidence showing that this material can help increase thermal stability and help preserve structure at high temperatures[82,83,85,86]. Miao *et al.*[85] reported on the attractive thermal stability of mesoporous Zr-oxophosphate as a solid acid catalyst because its ordered structure could be maintained even when treated at 800ºC. Similarly, Lucky *et al.*[82] found that the presence of ZrO_2 in the matrix of their TiO_2 nanotubes helped preserve the structure during high-temperature heat treatment.

The crystal structures of zirconia and titania are similar enough that Zr^{4+} ions can substitute for Ti^{4+} ions in the anatase matrix. ZrO_2 can adopt a tetragonal crystal structure when being introduced as a dopant in another tetragonal (e.g. anatase) phase. Unlike anatase TiO_2, which features six-coordinate Ti atoms, tetragonal zirconia consists of seven-coordinate Zr centres. This difference is attributed to the larger size of the Zr atom relative to Ti.

There are several explanations given for zirconia's thermostabilizing properties on the anatase crystal lattice. For one, Zr^{4+} ions are more electropositive than Ti^{4+} and are therefore more inclined to donate their electron density to O^{2-}. As a result, the neighbouring Ti-O bonds in the lattice become more stable and more difficult to break, increasing the lattice's stability at higher temperatures. Zirconia's thermostabilizing properties can also be attributed to its relatively large band gap (~5eV), making it more of an insulator than TiO_2. This could prove useful in mitigating the heat created during plasmonic resonance.

The purpose of this thesis is to examine the effects of incorporating ZrO_2 into plasmon-enhanced DSSCs with the goal of counteracting thermal energy loss and correspondingly increasing the allowable p-NP concentration without negatively affecting cell efficiency. In this study, Zr doping concentrations between 0 and 15% were incorporated into TiO_2 photoactive material to determine which concentration provided the best thermostabilizing properties. These Zr-doped photoanodes were subsequently integrated into plasmon-enhanced DSSCs to see if the presence of this thermostabilizer allowed for a higher plasmon-doping concentration.

2.3 Thesis Outline and Objectives

A lot of work in the field of dye-sensitized solar cell research has tried to benefit from the unique properties of plasmon NPs, but the optimization of the device to be able to accommodate a higher doping content constitutes a smaller research field. The objectives of this thesis are to investigate the ability of ZrO_2 to counteract thermal energy loss due to silver plasmonic NPs in TiO_2, and to determine which plasmonic-DSSC architecture proposed gives superior performance. This thesis consists of 7 chapters, and their contents are as follows:

Chapter 1 provides an introduction on solar energy, DSSCs and their role in the renewable energy market.

Chapter 2 provides a literature review on the topics covered in chapter 1. It surveys the current advances in DSSCs, their limitations, and the role that plasmonic nanoparticles can play in their improvement. The role of zirconia as a thermostabilizer is also discussed, and shapes an understanding of the thesis objectives.

Chapter 3 explains the experimental procedures performed and the characterization techniques used. Details regarding the fabrication process for DSSCs used throughout the study are provided.

Chapter 4 provides the results regarding the zirconia-doped TiO_2 material and their performance when incorporated into DSSC. The selection of certain composite formulations that proceeded to plasmon testing is reasoned.

Chapter 5 discusses the effect of plasmon and zirconia doping on the performance of fabricated DSSCs.

Chapter 6 discusses an alternative supercritical CO_2 synthesis route for TiO_2 in DSSCs.

Chapter 7 summarizes the results of the thesis work and concludes the obtained results. It also acknowledges any assumptions and limits of certain characterization and fabrication techniques, and provides recommendations for future work.

Chapter 3

3 Experimental Methods

In this chapter, the synthesis, characterization and fabrication techniques employed in this thesis work are described in detail.

3.1 Syntheses

3.1.1 TiO$_2$ and Zr-doped TiO$_2$ Nanopowders

The sol-gel process is a well-established chemical method based on hydrolysis and condensation reactions for generating colloidal nanoparticles from a liquid phase. This versatile technique holds many advantages like low processing temperatures, morphological, physical and chemical control, and is one of the most practically useful techniques to prepare nanostructured complex oxide mixtures with atomic level mixing of its components[87]. This method can therefore easily accommodate doping by replacing the titanium ions in TiO$_2$'s crystal lattice with other transition metal ions. The main stages of the sol-gel method are summarized in Figure 3.1. In a typical sol-gel reaction, a colloidal suspension (sol) is formed from the hydrolysis and polymerization reactions of the precursors, which are usually inorganic metal salts or metal organic compounds such as metal alkoxides[88]. Complete polymerization and loss of solvent leads to the liquid sol transforming into a solid (gel) phase. This gel can then be dried and calcinated to form crystalline nanoparticles.
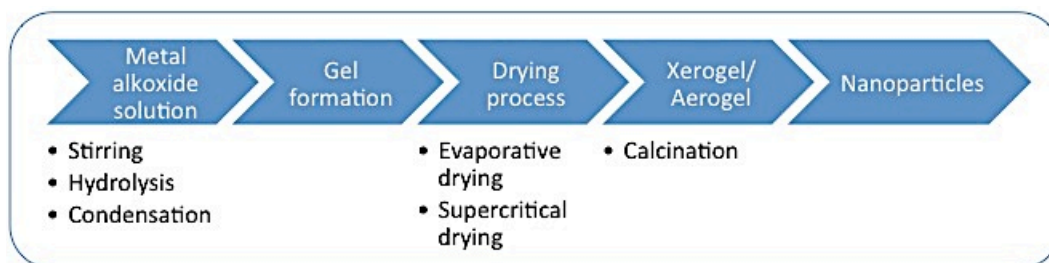
Figure 3.1: General overview of the sol-gel technique.

A sol-gel procedure adapted from Chen *et al.*[89] was used to prepare pure and Zr-modified titania nanoparticles. Titanium *n*-butoxide (TBO; 97%), zirconium *n*-butoxide (ZBO; 80%) acetylacetone (acac; >99%) and ethanol (EtOH; 99.7%) were all purchased from Sigma Aldrich. Hydrochloric acid (HCl; 37%) was purchased from Caledon.

The reaction setup is shown in Figure 3.2a. For the preparation of TiO_2 nanopowders, a solution of ethanol, HCl and H_2O were added dropwise to a mixture of TBO and acetylacetone in ethanol that was heated to 50ºC, and kept under vigorous stirring for 5 hours to ensure proper gel formation. Solvent evaporation was done by rotovap, and subsequently dried in a vacuum oven at 60 ºC overnight. The dry porous gel was separated into 4 equal portions and calcined at 400, 500, 600 and 700ºC for 4 hours (10 ºC/min ramp). The obtained powders were subsequently milled using a mortar and pestle (Figure 3.2b,c). In the preparation of Zr-modified TiO_2 nanopowders, the dopant was introduced into the reaction mixture by co-hydrolysis. This method allows for precise control of dopant concentration and homogeneous mixing of the precursors. Molar amounts of reactants for pure and doped titania are provided in Table 3.1. The Zr-doping concentrations ranged from 0-15% and refer to the molar amount of ZBO precursor added as a reactant.

Table 3.1: Precursors used in the sol-gel reactions. The Zr-doping concentration percentage refers to the molar amount of zirconium(IV) butoxide precursor added as a reactant.

Reagent	Amount (mol)			
	0% ZrBu	5% ZrBu	10% ZrBu	15% ZrBu
Ti *n*-butoxide	0.2	0.19	0.18	0.17
Zr *n*-butoxide	---	0.01	0.02	0.03
Acetylacetone	0.2			
EtOH	0.685 (x2)			
HCl	0.01			
H_2O	0.8			

In total, 16 samples were prepared: 4 different doping concentrations (0-15%) that were each calcined at 4 different temperatures (400-700 ºC).
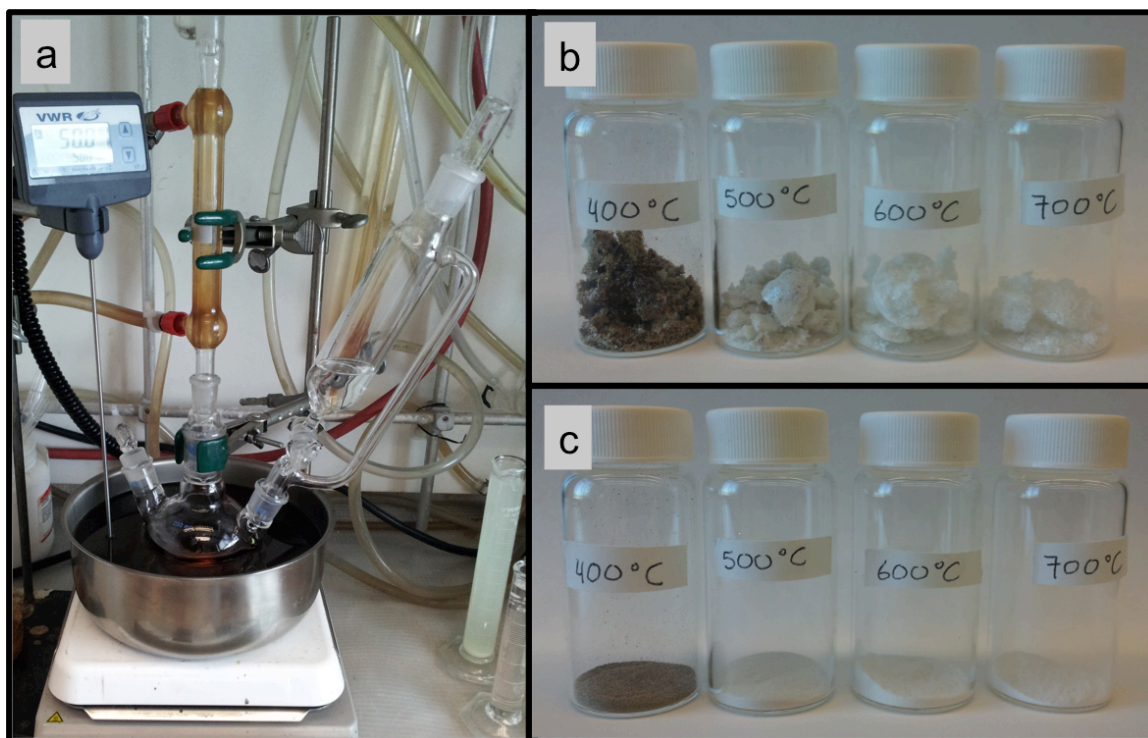
Figure 3.2: a) Sol-gel reaction setup; b) & c): Calcinated 10% Zr-doped-TiO$_2$ material before (c) and after (d) being ground with a mortar and pestle.

3.1.2 Synthesis of Plasmon Nanoparticles

3.1.2.1   Synthesis of Ag@TiO$_2$ Nanoparticles

To take advantage of inexpensive raw materials and ease of control of particle sizes, metals like gold and silver are largely only synthesized by bottom-up approaches, especially liquid phase synthesis. Large quantities of highly symmetric NPs with varying diameters can be produced by controlling the experimental conditions (temperature, metal salt concentration, growth time, etc.)[90]. It has previously been reported that dimethylformamide (DMF) has the ability to act both as a solvent and a reducing agent for noble metallic-NP synthesis[91,92]. To protect these particles from chemical corrosion and aggregation, controlled hydrolysis and condensation of an oxide-forming precursor

can be used to coat the particles by refluxing in the presence of a stabilizer, such as acetylacetone, to slow the hydrolysis[65,93].

The strategy of combining these two processes into a one-pot synthesis was used to produce Ag@TiO_2 nanoparticles for use as absorption antennas within DSSCs. DMF was used to reduce Ag ions and yield stable Ag particles in the presence of a stabilizer. This was followed by the direct growth of a TiO_2 shell on the plasmonic nanocrystals' surface by hydrolysis and condensation of the TiO_2 precursor. Titanium(IV) isopropoxide, (TIP; 97%), acetylacetone (acac; >99%) and silver nitrate (AgNO$_3$, >99.9%) were purchased from Sigma Aldrich. *N,N*-dimethylformamide (DMF; 99%), isopropanol (99.5%) and toluene (99.5%) were from Caledon.

The starting reaction mixture was prepared from two solutions. The first solution contained equimolar amounts of TIP and acac in isopropanol. A clear solution was obtained with mild sonication. The second solution was composed of 8.8 mM AgNO$_3$ and 13.88 M H_2O in DMF. 40 mL of the first solution and 20 mL of the second were transferred to a round-bottom flask and stirred for 10 minutes, before being heated to 65 ºC and refluxed for 1 hour. The colloid began as a yellow solution and gradually attained a green-black coloration as the reaction progressed (Figure 3.3a-d). The colloidal material was precipitated by the addition of toluene (Figure 3.3e), and then redispersed in isopropanol by sonication. This process was repeated three times to remove DMF and impurities formed in the reaction.

The solvent was evaporated and the dried powder ground to yield Ag@TiO_2 nanoparticles (Figure 3.3f). The shell thickness was varied by increasing the TiO_2 precursor concentration, keeping the reaction time constant. TIP concentrations of 20, 40 and 80 mM were attempted.
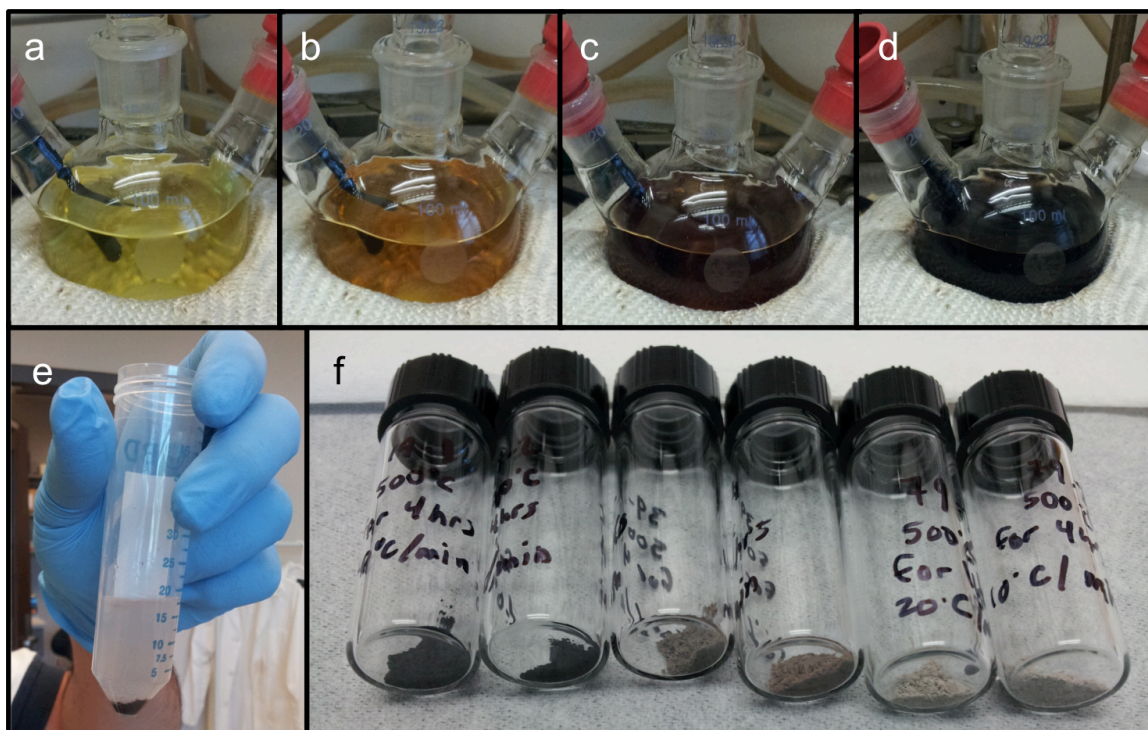
Figure 3.3: Ag@TiO$_2$ solution refluxing at 65 ºC after a) 5 minutes; b) 25 minutes; c) 45 minutes; d) 1 hour; e) precipitation of colloidal Ag@TiO$_2$ particles with toluene; f) Calcinated Ag@TiO$_2$ powder samples.

3.1.2.2 Synthesis of Neat Ag Nanoparticles

The reduction of silver oxide by hydrogen gas in water is a commonly used approach for synthesizing neat silver nanoparticles because hydrogen imparts no residual chemical impact on a system as a reducing agent, and silver oxide has sufficient solubility in water at elevated temperature[94]. There are also no separation or filtration steps needed, as the reaction yields solely Ag NPs dispersed in water. Here, a procedure was adapted from Evanoff *et al.*[94] where Ag NPs were synthesized in a saturated silver oxide aqueous solution at elevated temperature in equilibrium with hydrogen gas at elevated pressure. Silver(I) oxide (Ag_2O, 99.99%) was purchased from Alfa Aesar and water was of Milli-Q (ultrapure) grade. 5% (N_2 balance), 10% (Ar balance) and pure hydrogen gas (H_2) were purchased from PraxAir.

The reaction setup is shown in Figure 3.4a. In a typical reaction, 0.3 g of Ag_2O were added to 300 mL of ultrapure water and stirred vigorously. The mixture was then simultaneously heated to 70 ºC in an oil bath and the vessel flushed with Ar gas at 10 psi, without further agitation. Once the temperature was reached, the vessel was put under a hydrogen atmosphere and pressurized to 10 psi. Within a few minutes, the contents of the vessel became a faint yellow in colour, indicating the formation of Ag NPs. Aliquots were taken at regular intervals throughout the reaction with a custom-made spout (Figure 3.4b) to monitor the growth of the nanoparticles. The contents of the vessel continued to darken as the reaction progressed, indicating the size increase of the Ag NPs. Releasing the gas from the vessel stopped the reaction.

H_2 concentrations of 5, 10 and 100% were attempted as the vessel's atmosphere. Reactions proceeded much quicker with a higher H_2 atmospheric concentration, with pure H_2 reduction solutions reaching the same colour as a completed 5% H_2 reaction (230 minutes, right-most vial in Figure 3.4c) after only 30 minutes.
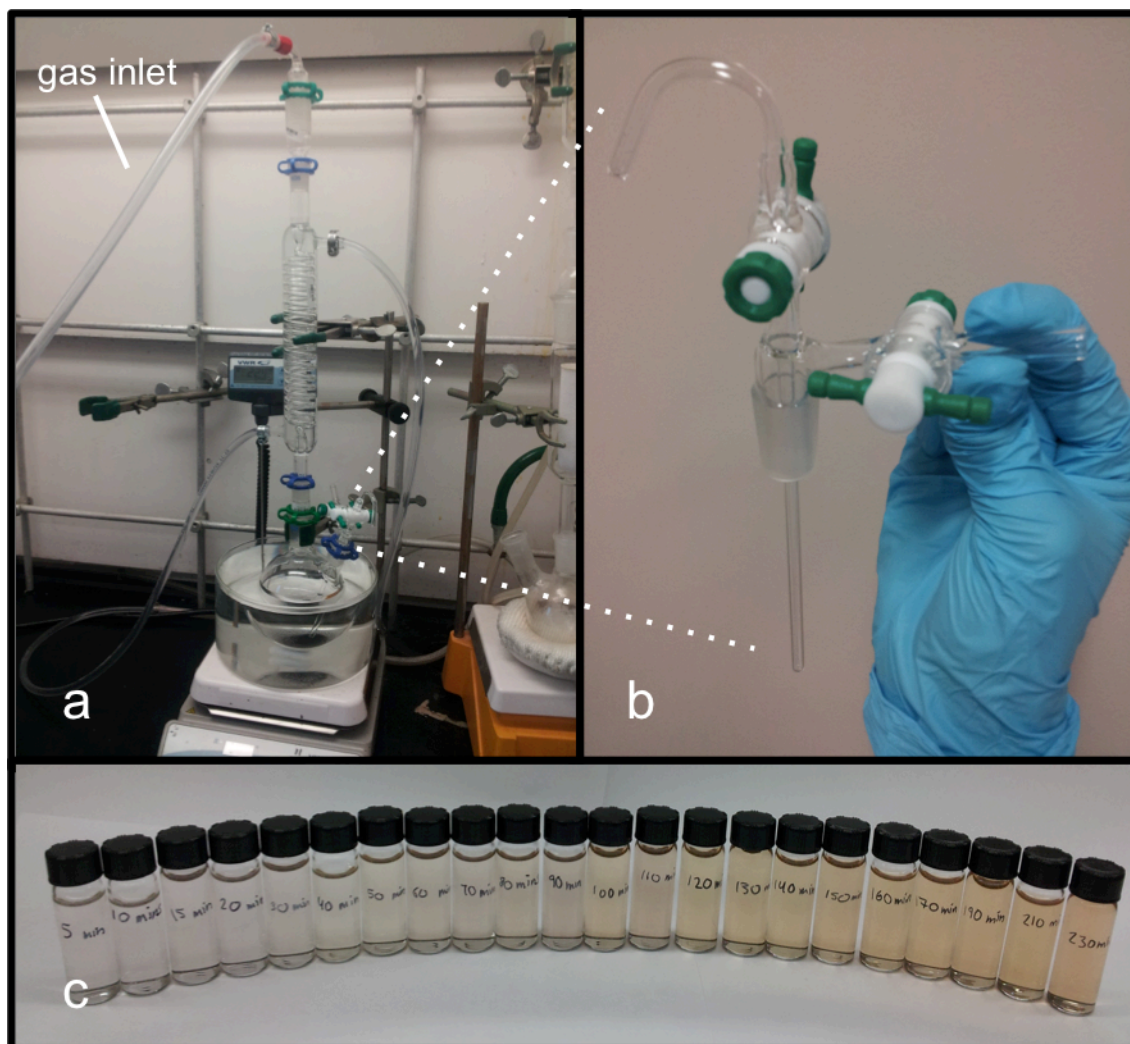
Figure 3.4: a) Reaction setup for Ag nanoparticle synthesis; b) Custom spout fabricated to prevent depressurization of the vessel during aliquot sampling; c) The colour evolution of Ag suspension aliquots taken at regular intervals throughout a 5% H_2 reduction reaction of ~4 hours.

The resulting colloidal suspensions were used to functionalize FTO glass electrodes with Ag NPs to make 'blanket-array' plasmon DSSCs. Section 3.3.2 describes the preparation procedure for blanket-array electrodes.

3.1.3 Atomic Layer Deposition

Atomic layer deposition (ALD) is a process in which a series of binary precursors are sequentially introduced into a sample chamber. The first precursor forms on the substrate as an intermediate monolayer with which the subsequent precursor reacts to form the product film. Purge periods between pulses are required to prevent chemical vapor deposition due to precursor intermixing. This mechanism allows for angstrom-level control over the thickness of the deposited film, and the ability to coat high-aspect-ratio substrates conformally[95]. These features make ALD an ideal TiO_2 fabrication methodology for DSSC photoelectrodes.

In this thesis, a Savannah 100 Cambridge Nanotech ALD instrument was used to coat TiO_2 onto Ag-functionalized FTO glass electrodes as part of the 'blanket-array' plasmon DSSC architecture. In order to form a pinhole-free (i.e. fully protective) TiO_2 layer, 300 cycles of TiO_2 precursor were needed, unless 2 cycles of an aluminum oxide (Al_2O_3) adhesion layer were first deposited, in which case only 211 cycles of TiO_2 precursor were necessary. Both precursor formulations were used in DSSCs to determine which of the two showed superior performance.

For TiO_2 deposition, alternating 0.1-second pulses of the precursors titanium isopropoxide (TIP) and H_2O were used to form TiO_2 layers, and alternating 0.015-second pulses of trimethyl aluminum (TMA) and H_2O were used for Al_2O_3 deposition. The precursors were held in the deposition chamber for 1 s before a 12 s pump. The chamber temperature was set to 200 ºC, and the N_2 flow rate was 20 sccm. TIP was held at 80 ºC and all other precursors were used at RT.

3.1.4 Synthesis of TiO_2 in Supercritical CO_2

Properties of sol-gel products depend on the precursors, processing temperature, catalyst solvents, and solvent removal process[87]. As a side project, the synthesis of TiO_2 was performed using supercritical CO_2 as a co-solvent to see how its inclusion in the conventional sol-gel method would alter the final properties of TiO_2, and as such how it would affect the performance of DSSCs.

TiO_2 NPs were synthesized in a high-pressure view-cell reactor. The high-pressure reactor contained a CO_2 inlet as well as temperature and pressure controllers. A syringe pump was used to deliver the pressurized CO_2 into the view cell using a 2-way valve injection loop. Detailed information about the reactants and experimental conditions is reported in chapter 6.2. A total of 8 products (T1-T8) were synthesized, and their list of reagents and operational conditions can be found in Table 6.1. The reaction volumes were limited to 35 mL to accommodate the maximum internal volume capacity of the reactor.

The first three samples were produced with the same precursors used in the conventional sol-gel synthesis described in chapter 4.2. Sample T1 was synthesized via the conventionally hydrolytic sol-gel (HSG) route where water serves as both a ligand and a solvent[87]. The non-hydrolytic sol-gel (NHSG) route is an alternative pathway for the preparation of metal oxides under the exclusion of water, where the oxygen for the metal oxide formation is provided by the solvent or by the organic constituent of the precursor[87] instead of water. The NHSG process is relatively slower than the HSG approach, but this lower reactivity makes the morphologies and microstructures of NHSG-derived metal oxides more controllable, which was the reasoning for trying the supercritical reaction of samples T2 and T3 in the absence of water.

The reaction procedure for the HSG and NHSG reactions are as follows. A solution of TBO and acetylacetone in ethanol was mixed directly into the view cell. Under constant stirring, the solution was allowed to reach the desired temperature of 50 ℃. Meanwhile, a solution of ethanol, hydrochloric acid and water was stirred separately, then added drop-wise to the view cell reaction once the temperature had reached 50 ℃. For the non-hydrolytic reactions (T2, T3), the volume of water was replaced by $scCO_2$. After sealing

the reactor, $scCO_2$ was added at the desired pressure, and the reaction was left to proceed for the allotted time under vigorous stirring. The reactions ran between 3-5 hours and at a pressure of 90 bar.

This study also used green bio-sourced solvents coupled with $scCO_2$ to prepare TiO_2 nanoparticles, with the hopes of encouraging the development of cleaner processes for nanomaterials used in DSSCs. Glycerol, ethyl lactate and ethyl acetate were used in conjunction with $scCO_2$ to synthesize samples T4 to T8. The esters were each used in conjunction with two different Ti precursors, titanium butoxide (TBO) and titanium diisopropoxide bis(acetylacetonate) (DIPBAT), to see how their variation in reactivity would affect the product's characteristics. DIPBAT is a less reactive precursor than TBO because its bonds are more stable.

In a typical bio-based solvent reaction, the reactants were added into the view cell all at once. The mixture was heated to 80 ºC, after which $scCO_2$ was pumped into the cell until the desired pressure was reached. Reactant volumes totalled approximately 20 mL and the remaining volume of the reactor was left for $scCO_2$. The reactions ran for 3 hours under constant stirring at a pressure of 150 bar.

For all samples, the solvent was evaporated by rotovap and in an oven overnight at 60ºC. The as-prepared TiO_2 nanopowders were amorphous, but readily converted to anatase by the same heat treatment subjected to the conventionally synthesized control TiO_2 NPs (4 hours at 400 °C). Crystalline oxides were obtained after calcination.

3.2   Characterization Techniques

3.2.1 Microscopy

Morphological characteristics of samples were observed using a LEO-Zeiss 1540 XB scanning electron microscope (SEM), a Phillips CM10 transmission electron microscope (TEM) and a FEI Titan 80-300 LB high resolution TEM (HR-TEM).

Scanning Electron Microscopy

An SEM uses a focused beam of high-energy electrons to create a 2-dimensional image of a specimen's surface. Several forms of emission are collected from the surface being illuminated from which an image is generated pixel-by-pixel that reveals information about the sample's surface features, the orientation of materials making up the sample, and its chemical composition. Secondary electron (SE) imaging, being more surface-sensitive, has greater resolution and is used to produce the classic topographic images that are most familiar. Images developed from back-scattered electrons (BSE) have the advantage of providing compositional contrast, as the intensity of backscattering is proportional to the mean atomic number of the atoms. As a result, heavier elements appear brighter than lighter elements in a backscattered electron image. Both SE and BSE modes have been used in this thesis. Before SEM analysis, samples were sputtered with 2-3 nm of Osmium using a coating machine to prevent surface charging.

Transmission Electron Microscopy and High Resolution TEM

The function of a TEM is much like the SEM, although the electron beam passes through the sample being imaged rather than bouncing off the surface. As such, a TEM specimen has to be electron transparent, meaning that it has to be thin enough to transmit sufficient electrons such that the intensity can be detected beyond the sample. Usually, the thickness of a TEM specimen is lower than 100 nm. TEM images can show internal structures of specimens with magnification up to 1 million times, revealing structures in atomic resolution. A HRTEM uses both transmitted and scattered beams to create an

interference image, and can go up to a maximum magnification of 1.5 million times. TEM and HRTEM were used to image $Ag@TiO_2$ nanoparticles.

Although TEM resolution is about an order of magnitude greater than SEM resolution, an SEM is able to image bulk samples and has a much greater depth of field. An SEM can therefore produce images that are a good representation of the overall 3D structure of the sample.

3.2.2 Spectroscopic Techniques

Ultraviolet-Visible Spectroscopy

Ultraviolet-visible spectroscopy (UV-Vis) provides information on electronic transitions in molecules. When UV or visible radiation is absorbed, electrons are excited from their ground state to an excited state. The energy absorbed is equal to the difference between the two levels. A spectrophotometer records the wavelengths at which absorption occurs, together with the degree of absorption at each wavelength. The energy associated with a given segment of the spectrum is proportional to the frequency of a given wavelength of radiation. The resulting spectrum is presented as a graph of absorbance versus wavelength. Compounds that absorb in the visible regions, such as some transition metal compounds and organic dyes, are coloured. Those that absorb only in the UV region are colourless.

A SHIMADZU UV-3600 UV-Vis-NIR spectrophotometer was used to measure the absorption spectra of Ag NPs aliquots sampled throughout their synthesis reaction within the spectral range of 300 to 700 nm. Standard PMMA cuvettes (VWR) with a 10 mm path length were used to hold sample solutions.

X-ray Diffraction

X-ray diffraction (XRD) is a technique that can provide valuable information about the phase and crystallographic structure of crystalline materials. X-rays are created by a

cathode ray tube dislodging electrons from a specified target such as copper (Cu). The X-rays are collimated towards the crystal holder, where the x-rays are either reflected or refracted against the crystalline lattice of the sample. The angle of incidence of X-rays against the crystalline lattice defines the spectrum produced.

In a DSSC photoanode, the interconnected TiO_2 particles that constitute the semiconducting film need to be crystalline in order to ensure proper charge transport throughout the cell. In this thesis, A Bruker AXS D2 Phaser diffractometer equipped with Diffract.EVA 2.0 software was used to confirm the crystal phase of synthesized TiO_2 material, and identify the ZrO_2 doping presence in samples having increasing doping concentrations and increasing calcination temperatures. XRD was also used to identify the crystallinity of the core and shell material of synthesized Ag@TiO_2 samples. Cu Kα radiation (k = 1.5418 Å) was used over the range of $20^\circ \leq 2\theta \leq 80^\circ$, with the intensity data collected at 0.2° intervals.

Energy Dispersive X-ray Spectroscopy

Energy-dispersive X-ray spectroscopy (EDS) is an analytical technique used for the elemental analysis and chemical characterization of a sample. It relies on the fundamental principle that each element has a unique atomic structure allowing for a unique set of peaks on its X-ray emission spectrum.

Atoms within a specimen contain ground state electrons in discrete energy levels. When a high-energy beam of electrons is focused onto a designated area of the sample, the incident beam excites an electron in an inner shell, creating an electron hole. An electron from a higher-energy shell then fills the hole, and the difference in energy between the two shells is released in the form of an X-ray. The number and energy of the X-rays emitted from the sample are detected and translated into a spectrum. As the X-ray emission corresponds to the difference in energy between the two shells, which is characteristic of the atomic structure of the element from which the X-rays were emitted, the sample's elemental composition can be resolved.

Ratios and chemical composition of samples in this thesis were determined through elemental mapping and EDS. Spectroscopes were attached to both the SEM and the HR-TEM.

X-ray Photoelectron Spectroscopy

X-ray photoelectron spectroscopy (XPS) is a quantitative technique that provides valuable information on the surface composition of a material. It measures the elemental composition, chemical states and electronic states of elements present within the top 7-10 nm of a sample. An XPS spectrum is obtained by measuring the number and kinetic energy of electrons that escape from the sample as a result of being bombarded with a beam of X-rays. Because the energy of the X-ray used is known, the electron binding energy ($E_{binding}$) of each of the emitted electrons can be determined using the equation

$$E_{binding} = E_{photon} - E_{kinetic} - \Phi \qquad \text{(eq. 3.1)}$$

where E_{photon} is the energy of the X-ray photons being used, $E_{kinetic}$ is the kinetic energy of the emitted electron as measured by the instrument, and Φ is the work function of the spectrometer. Since $E_{binding}$ corresponds to the minimum energy required to release an electron from a particular and distinct electronic configuration within the atom, characteristic information about a sample's surface composition can be resolved. All elements can be detected using this technique with the exception of hydrogen and helium, which do not have core electrons necessary for analysis.

XPS data obtained in this study used a Kratos AXIS Ultra spectrometer employing a monochromatic Al Kα X-ray source under high vacuum conditions. The survey scan analyses were carried out with an analysis area of 300 x 700 microns and a pass energy of 160 eV.

Electron Energy Loss Spectroscopy

Electron energy loss spectroscopy (EELS) is a very powerful technique that is known as being complementary to EDS, another common spectroscopy technique discussed

previously. Its incredibly high resolution capabilities make it the ideal analytical partner to the high spatial resolution provided with HRTEM.

During EELS analysis, a material is exposed to a beam of electrons. Some of the electrons will undergo inelastic scattering, meaning that they lose energy and have their paths slightly and randomly deflected. The amount of energy loss can be measured with an electron spectrometer.

In this thesis, EELS was used for elemental analysis of Ag@TiO$_2$ particles when being imaged on the HRTEM.

3.2.3 Other Techniques

N$_2$ Physisorption

Gas adsorption analysis is one of the most commonly used techniques for surface area and porosity measurements. During a N$_2$ physisorption process, a porous solid is exposed to N$_2$ gas within a range of pressures. At a low relative pressure, a monolayer of gas adsorbs onto the solid's surface. Beyond monolayer formation, the amount of adsorbed gas gradually increases as the relative pressure increases. At higher pressure, capillary condensation within the pores causes the amount of gas adsorbed to increase dramatically, until the pores are full. The capillary condensation is proportional to the equilibrium gas pressure and the size of the pores. After adsorption is complete, desorption occurs by withdrawing the adsorbed gas by reducing the pressure. Evaporation occurs until only a layer of adsorbed gas remains on the walls of the pores. The thickness of the remaining monolayer and the amount of condensed gas removed from the pores are used to calculate the pore volume and pore size distribution of the solid.

The specific surface area, pore size, and particle size of a DSSC's photoactive material are important features to consider for a cell's performance. Textural characterizations of pure and doped oxide powders were obtained from Nitrogen (N$_2$) adsorption-desorption isotherms measured at 77 Kelvin (K) using a Micromeritics TriStar II 3020 surface area

and porosity instrument. Approximately 0.3 to 0.6 g of powder were placed in a test tube and allowed to degas for a minimum of 5 hours at 150 ºC in flowing N_2 gas prior to analysis. This removes contaminants such as water vapour and adsorbed gases from the samples. The Brunauer, Emmett and Teller (BET) theory was used to calculate the specific surface area of samples from the number and cross-sectional area of N_2 gas molecules required to reach a monolayer adsorption on the powder samples' surface. For the case of nitrogen, the cross-sectional area is taken as 16.2 $Å^2$/molecule[96]. The pore parameters were also determined using the Barret-Joyner-Halenda (BJH) theory applied to the desorption branch of the isotherms.

Solar Simulation

The power conversion efficiency of a solar cell is determined from the current versus applied voltage (I-V) characteristics under illumination. The I-V characteristics of fabricated DSSCs were measured under the simulated AM 1.5 illumination of a Newport Oriel 92250A-1000 solar simulator at 100 mW/cm². Light intensity was calibrated with a certified Oriel 91150V monocrystalline Si reference cell. I–V curves were obtained by applying an external bias to the cells and measuring the generated photocurrent with a Keithley 2420 digital source meter. The voltage range and current limit were -0.1 – 0.8 V and -700 mA, respectively.

All cells had a working area of 0.1257 cm². For statistical purposes, the average characteristic values of 6 cells were taken for each sample.

3.3   Fabrication Techniques

3.3.1 Fabrication of DSSCs

Materials

The FTO working electrodes, Pt counter-electrodes, polymer gaskets, electrolyte (Iodolyte Z-150), rubber syringes and polymer sealings were all purchased from Solaronix. N719 dye [cis-Bis(isothiocyanato)bis(2,2'-bipyridyl-4,4'-dicarboxylato) ruthenium(II)] and *tert*-butanol (>99%) were purchased from Sigma-Aldrich. Isopropanol (99.5%) and acetonitrile-190 (99.8%) were purchased from Caledon. Anhydrous ethanol was purchased from Commercial Alcohols.

Fabrication and assembly

Figure 3.5 shows a selection of steps during a typical fabrication and assembly of a DSSC. 2.5 x 2.5 cm fluorine-doped tin oxide (FTO) glass electrodes (thickness, 2.2 mm; sheet resistance, 7 Ω/sq) were first cleaned in a detergent solution (Sparkleen) to remove residual organic contaminants, followed by deionized water and isopropanol. Between each wash, the electrodes were sonicated for 10 minutes. Clean electrodes were stored in isopropanol and were blown dry using Ar gas before use. 2 x 2 cm Pt counter-electrodes (thickness, 2 mm) were cleaned and stored in the same manner.

TiO_2 paste was prepared by mixing 30 mg of synthesized TiO_2 (or Zr-doped TiO_2) powder (see section 3.1.1) with 0.5 mL of a custom binder solvent, and grinding them in a mortar and pestle until a homogeneous gluey consistency was achieved (Figure 3.5a,b). The binder solvent was composed of a solution of 20% ethyl cellulose in ethanol, terpineol and acetic acid. TiO_2 thin films were formed by doctor blading a layer of paste onto a cleaned FTO glass electrode using a tape template of an area of 0.1257 cm^2 using a circular die cutter (Figure 3.5c,d). The paste was left to air dry at room temperature for 30 minutes, then calcined at 500ºC for one hour. The temperature ramp was set to 15ºC/min to avoid surface cracking of the film and ensure proper adhesion to the FTO glass.

After cooling to about 80 ℃, photoelectrodes were immersed into a 0.25 mM N719 dye solution containing a 1:1 volume ratio of *tert*-butanol and acetonitrile, and left to soak for 24 hours at room temperature. After dyeing, the sensitized photoanodes were washed with anhydrous ethanol to remove any excess dye molecules to ensure that the porous TiO_2 film was covered with a monolayer of dye.

After reactivating the Pt counter-electrodes by heating them on a hotplate at 120 ℃ for a few minutes, the sensitized photoanodes and the Pt counter-electrodes were assembled in a sandwich-like configuration and sealed with a hot-melt gasket at 120℃ (Figure 3.5e). The electrolyte containing 150 mM iodide/tri-iodide redox couple was introduced into the cells through a predrilled hole in the counter electrode using a rubber syringe. The Pt electrodes were purchased with one predrilled hole, but a secondary hole was drilled to facilitate air displacement while filling the cell with the electrolyte. Finally, the holes were sealed with a hot-melt polymer and a cover glass (Zeiss, 0.17 mm thickness) to avoid leakage of the electrolyte (Figure 3.5f). All fabrication was performed under atmospheric conditions. For statistical purposes, 6 cells were fabricated for each sample to ensure consistency in results.
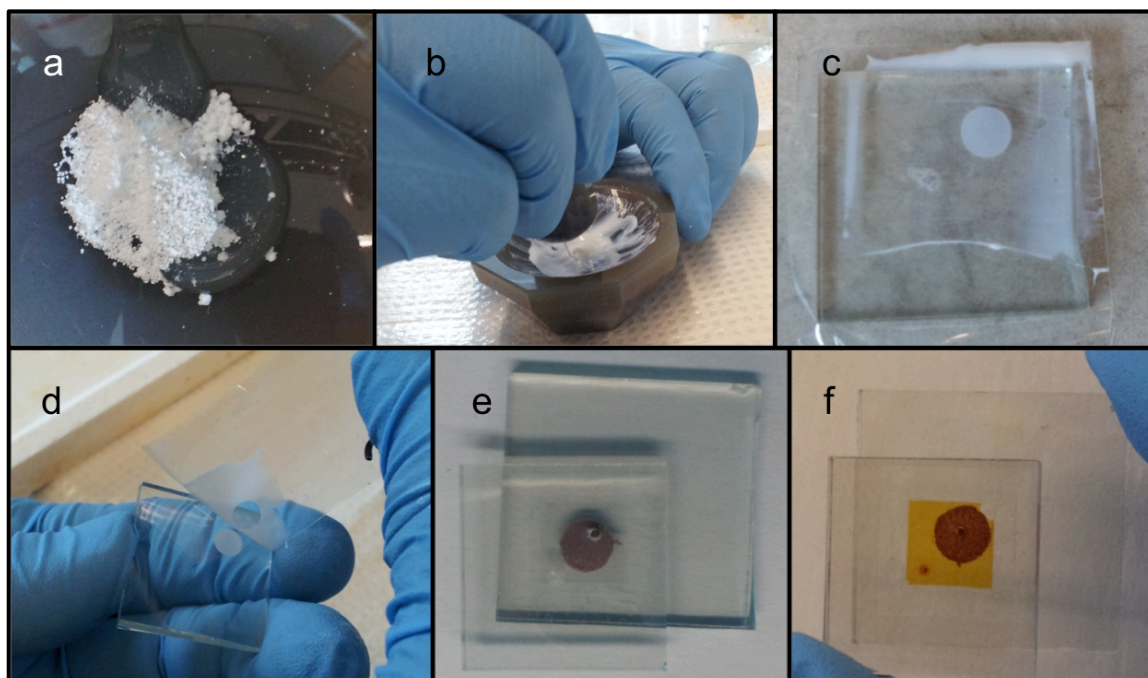
Figure 3.5: Progression of a DSSC fabrication; a) and b) show paste preparation, c) and d) show photoanode preparation, e) shows a sensitized photoanode assembled with the counter electrode, and f) shows an electrolyte-filled and sealed completed DSSC.

Plasmon-doped cells were fabricated in the same manner. The only modification to the 'chocolate chip' cell fabrication was in paste preparation, where the applicable amount of $Ag@TiO_2$ powder was added to the TiO_2 (or Zr-doped) powder in the mortar and mixed with the solvent to create a plasmon-doped paste. The only modification to the 'blanket array' cell fabrication was in the glass electrode preparation, where the FTO glass was functionalized with $Ag@TiO_2$ NPs (as described in section 3.3.2) before having TiO_2 paste doctor bladed onto them.

3.3.2 Preparation of 'Blanket-Array' Electrodes

In the blanket-array design, Ag@TiO$_2$ NPs are used primarily as nano-mirrors within the DSSC to increase the optical path length. The titania barrier prevents direct contact between the Ag NPs and the electrolyte, slowing the back reaction of electrons to the redox couple medium during cell operation. ALD was used as the methodology to protect the Ag NPs with TiO$_2$ because it ensures well-defined, conformal growth.

FTO electrodes (thickness, 2.2 mm; sheet resistance, 7 Ω/sq) were purchased from Solaronix. Sulfuric acid (H$_2$SO$_4$, 98%) was purchased from Caledon. Hydrogen peroxide (H$_2$O$_2$, 30 wt. % in H$_2$O) and poly(4-vinylpyridine) (P4VP, average MW ~60,000) were purchased from Sigma-Aldrich. The silver suspensions were synthesized according to the procedure in section 3.1.2.2. ALD was performed following the procedure and specifications described in section 3.1.3.

To prepare a 'blanket-array' electrode, FTO-coated glass electrodes were first cleaned with piranha solution (3:1 H$_2$SO$_4$:H$_2$O$_2$) for 30 minutes at room temperature. This treatment not only removes all organic contaminants from the FTO surface, but also leaves it with a high surface energy by introducing hydroxyl groups (Figure 3.6a). Note: This solution reacts violently with most solvents, and extreme caution was exercised when carrying out this cleaning step. After piranha treatment, the electrodes were thoroughly rinsed with deionized water before being blown dry with Ar gas.

The cleaned FTO substrates were functionalized with P4VP by soaking them in an ethanolic solution of 2 wt % P4VP for 3 hours. The electrodes were then rinsed with ethanol to remove any unadsorbed polymer and heated in an oven for 1 hour at 100 ºC (20 ºC/min ramp). This is meant to relax the monolayer of P4VP to facilitate the even distribution of Ag NPs on the surface. The P4VP-functionalized electrodes were then soaked in the synthesized silver suspensions. Having empty d-orbitals characteristic of transition metals, the Ag NPs in the solution bind strongly to P4VP through the lone pair of electrons on the nitrogen of the pyridine ring (Figure 3.6b,c).

After 12 hours of soaking, the Ag-functionalized electrodes were rinsed with deionized water and dried with Ar gas before finally undergoing atomic layer deposition to create a uniform layer of TiO_2 on the Ag-NP array (Figure 3.6d). In order to have a pinhole-free (i.e. fully protective) titania layer, 300 cycles of TiO_2 precursor were needed, unless 2 cycles of Al_2O_3 were first deposited, in which case only 211 cycles of TiO_2 precursor were required. Both configurations were prepared to determine which performed better in DSSCs.
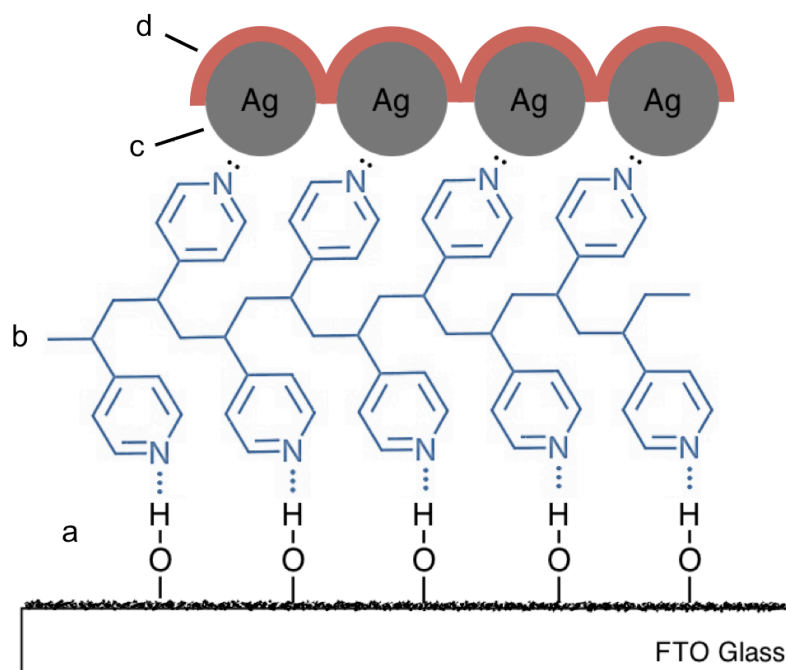
Figure 3.6: Schematic showing the breakdown of layers of an ALD-coated electrode.

Chapter 4

4 Synthesis and characterization of a binary oxide ZrO_2-TiO_2 and its application in dye-sensitized solar cells

4.1 Introduction

When a DSSC's photoactive material is illuminated, the energy removed from the incident light is either scattered, or locally absorbed. The dissipation of energy due to absorption may give rise to a number of secondary effects, including local heat production. One of the assumptions of the Shockley-Queisser limit[74] is that excited electrons created by high-energy photons are immediately relaxed to the band edge – that is, the fraction of energy of photons with energy greater than the bandgap is immediately lost as heat, a phenomenon referred to as thermalization. This means we can always expect to have some temperature increase in the cell.

According to several studies[77–81], a small amount of transition metal doping has been found very effective in improving the thermal stability and activity of TiO_2. Zirconia (ZrO_2) is one of these suitable dopants, known to have very high thermostabilizing properties[82,83]. It has one of the highest dielectric constants for metallic oxides[84] and therefore exhibits good optical properties. Additionally, it is very chemically stable due to its multi-electronic configuration, including its d-orbital electrons, characteristic of transition metals. Ti and Zr are also in the same group of elements (IVB), which gives them comparable physicochemical properties.

There is plenty of evidence showing that ZrO_2 can help increase thermal stability and help preserve structure of the photoactive material of DSSCs at high temperatures[82,83,85,86] yet an extensive study on the optimal doping concentration has yet to be investigated. Miao *et al.*[85] reported on the attractive thermal stability of mesoporous Zr-oxophosphate as a solid acid catalyst because its ordered structure could be maintained even when treated at 800ºC. Similarly, Lucky *et al.*[82] found that the presence of ZrO_2 in the matrix of their TiO_2 nanotubes helped preserve the structure during high-temperature heat treatment.

In this study, Zr doping concentrations between 0 and 15% were incorporated into TiO_2 photoactive material to determine which concentration provided the best thermostabilizing properties. These Zr-doped photoanodes were subsequently integrated into DSSCs to see if the presence of this thermostabilizer improved photovoltaic efficiency. The structural and compositional properties of the prepared binary oxide photoactive materials were investigated using XRD, BET, SEM and EDX. Solar simulation was used to determine the power conversion efficiencies of the composite photoactive materials in DSSCs. Zr was selected as a dopant since it has been widely used in industry, and well investigated as a thermostabilizer.

4.2 Experimental

In this study, a sol-gel procedure adapted from Chen *et al.*[89] was used to prepare pure and Zr-modified titania nanoparticles. For the preparation of Zr-modified TiO_2 nanopowders, the dopant was introduced into the reaction mixture by co-hydrolysis. This method allows for precise control of dopant concentration and homogeneous mixing of the precursors. Molar amounts of reactants for pure and doped titania are provided in Table 4.1. In total, 16 samples were prepared: nanopowders of 4 different doping concentrations (0-15%) were each calcined at 4 different temperatures (400-700 ºC) to see how their stability at higher temperatures was affected by Zr modification. Titanium *n*-butoxide (TBO; 97%), zirconium *n*-butoxide (ZBO; 80%) acetylacetone (acac; >99%) and ethanol (EtOH; 99.7%) were all purchased from Sigma Aldrich. Hydrochloric acid (HCl; 37%) was purchased from Caledon.

Table 4.1: Precursors used in the sol-gel reactions. The Zr-doping concentration percentage refers to the molar amount of zirconium(IV) butoxide precursor added as a reactant.

Reagent	Amount (mol)			
	0% ZrBu	5% ZrBu	10% ZrBu	15% ZrBu
Ti n-butoxide	0.2	0.19	0.18	0.17
Zr n-butoxide	---	0.01	0.02	0.03
Acetylacetone	0.2			
EtOH	0.685 (x2)			
HCl	0.01			
H$_2$O	0.8			

The crystal structure of the TiO$_2$ powders was analyzed by X-ray powder diffraction (XRD) using a Bruker AXS D2 Phaser diffractometer with Cu Kα radiation, as well as JCPDS 00-021-1272 and JCPDS 79-1771 for TiO$_2$ anatase and tetragonal ZrO$_2$ crystal structure identification. The specific surface area of the powders was determined by applying the Brunauer-Emmett-Teller (BET) theory to N$_2$ adsorption-desorption isotherms obtained from a Micromeritics TriStar II 3020 surface area and porosity instrument. The pore size distributions were also calculated using the Barret-Joyner-Halenda (BJH) theory. The morphology and average particle size of the samples were further confirmed by scanning electron microscopy (SEM) using a LEO-Zeiss 1540 XB microscope equipped with an Oxford Instruments x-ray system allowing for in-situ elemental mapping and analysis (EDS). Finally, the power conversion efficiency of dye-sensitized solar cells (DSSCs) comprising the synthesized powders as the photoactive layer was measured using the simulated illumination of a Newport Oriel 92250A-1000 solar simulator and a Keithley 2420 digital source meter. DSSCs were fabricated according to the procedure in section 3.3.1.

4.3   Results and Discussion

Zr-modified TiO$_2$ nanopowders were synthesized using a sol-gel technique described in section 3.1.1. Incorporating Zr^{4+} into the TiO$_2$ crystal inevitably introduces lattice

defects, and although the presence of a few defects can improve the photoelectrochemical activity of a dye-sensitized solar cell based on a $Zr_xTi_{1-x}O_2$ photoactive layer, an excess of defects can promote charge recombination. That is, a low Zr-doping concentration can be beneficial in that it can reduce the TiO_2-band gap by introducing states just below the conduction band (CB), thereby reducing the energy threshold of light waves required to excite electrons into the CB. However, increasing the concentration further plays a role in creating charge-trapping centers[97] that have a deleterious effect on travelling electrons. Additionally, the literature discusses how Zr-doping over 50% can cause the increase of band gap values attributable to the quantum-size effect[98]. Widening the already-large bandgap of TiO_2 would be unfavorable for low-energy photon harvesting. Therefore, the doping concentrations attempted did not exceed 15%.

4.3.1 Effect of Zr-Doping Concentration on TiO_2

Powder X-ray diffraction (XRD) measurements were performed to examine the effect of doping and thermal treatment on the crystal structure of TiO_2. The as-prepared samples did not exhibit any diffraction peaks, indicating the initial amorphous nature of the samples. Upon thermal treatment, the samples were readily converted to crystalline oxides. XRD spectra of TiO_2 samples with doping concentrations in the range of 0-15 mol% Zr calcined at 500 °C are shown in Figure 4.1a. The peaks in the diffraction patterns correspond to the reported characteristic peaks of anatase TiO_2 (JCPDS 00-021-1272).

Zirconia has 4 strong diffraction peaks at 30.55°, 35.40°, 50.70° and 60.35°, which can be attributed to the (111), (200), (220), and (311) diffraction planes of tetragonal zirconia corresponding to the standard JCPDS 79-1771. The XRD spectra for 10 and 15% Zr-doped TiO_2 in Figure 4.1a showed the slightest hint of a ZrO_2 peak at 30.55°. The weakness of the peak is likely attributed to the relatively low Zr doping content and may also indicate that the Zr ions are well dispersed within the TiO_2 phase. The other ZrO_2-characteristic peaks may be blurred and merged with the characteristic peaks of TiO_2, as they were not detected. These other peaks would perhaps be more pronounced at higher

doping concentrations, but at these low concentrations, it can be assumed that the Zr^{4+} ions are well dispersed within the TiO_2 phase.

This assumption can further be validated by a slight spectral shift of the doped samples in comparison to the pure titania sample (0% Zr, green). The crystal structures of zirconia and titania are similar enough that Zr^{4+} ions can substitute for Ti^{4+} ions in the anatase matrix. The lattice structure of TiO_2 is locally deformed during Zr^{4+} substitution however, because of the difference in ionic radius between the two cations (Ti^{4+} = 61 pm, Zr^{4+} = 72 pm)[99,100]. It can therefore be concluded that Zr doping causes an expansion of the anatase lattice parameters with respect to the pure anatase phase at the locations where Zr ions have replaced Ti, which causes the slight shift in the XRD peaks. This shift becomes more pronounced with increasing doping concentration, and is most noticeable at the 38.0, 48.6, and 63° diffraction peaks for the 15% Zr sample (red).

In Figure 4.1b, the doping concentration of the TiO_2 samples was kept constant at 10%, and the calcination temperature was varied between 400 and 700 °C. These results show that Zr doping retards not only the crystallite growth of titania (shown in BET results below), but also the anatase-to-rutile phase transformation[101]. No phase change from anatase to rutile was found across the 10% Zr samples, although they were calcined at temperatures expected to cause an anatase-to-rutile phase transformation[102]. Instead, the anatase crystal structure was maintained at all temperatures, with the relative peak intensities even increasing with temperature. This stabilization of the anatase phase can be explained by the fact that Zr^{4+} is more electropositive than Ti^{4+}. As such, the electronic cloud in TiO_2 nanoparticle containing Zr doping will be more loosely held, thus favouring the formation of the less dense anatase phase over the rutile phase[103]. In other words, the tight packing arrangements required for rutile phase formation is fully suppressed by the framework substitution of Zr^{4+}. Furthermore, the larger size and higher electropositivity of Zr^{4+} compared to Ti^{4+} allows the lattice to exhibit better bonding properties, and thus higher thermal stability than pure TiO_2[103,104]. The diffraction peaks in Figure 4.1b maintaining and even improving their sharpness when submitted to high calcination temperatures is evidence of zirconia's thermostabilizing properties.
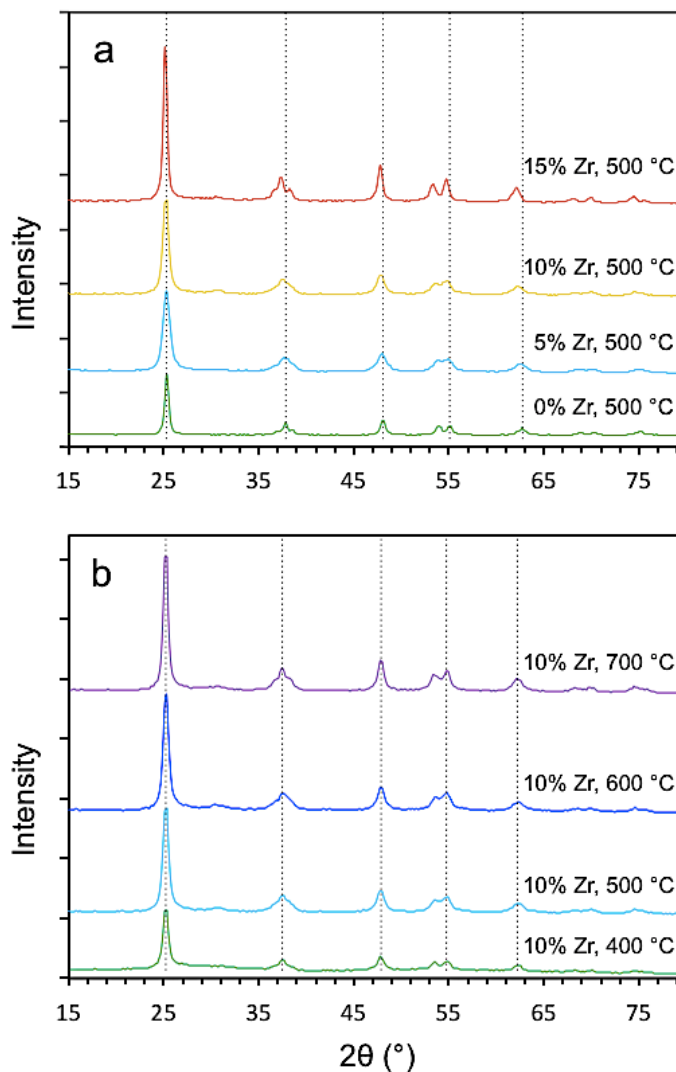
Figure 4.1: XRD spectra of TiO$_2$ samples; a) various doping concentrations calcined at 500 ºC; b) 10% Zr doping at various calcination temperatures.

Again, the slightest indication of a ZrO$_2$ peak at 30.55º can be seen in the spectra of all 10% Zr samples, but its weakness suggests the effective incorporation of Zr into the TiO$_2$ crystal lattice. Rather than having a secondary phase segregated from TiO$_2$ NPs, the diffusion of Zr into the TiO$_2$'s crystal lattice creates one single phase, which is beneficial for uninterrupted electron transport during DSSC operation. Travelling electrons run a smaller risk of recombination, as they do not encounter any phase boundaries, which are common places for traps to be located.

The effect of Zr-doping concentration on specific surface area and pore structure at various calcination temperatures was studied by N_2 physisorption and BET analysis. The adsorption-desorption isotherms of a selection of TiO_2 and Zr-doped TiO_2 samples are shown in Figure 4.2, and the corresponding specific surface areas (SSA), average particle sizes and average pore sizes of the samples are listed in Table 4.2. All samples demonstrated type IV isotherms regardless of doping and thermal treatment, indicating that the samples are of a porous nature[105]. The hysteresis loops are all of the type H1, indicating that the samples are composed of agglomerated spherical NPs. The locations of the hysteresis loops lie between 0.4 and 0.8 relative pressure (P/Pº), which is an indication of mesoporous capillary condensation[106]. This is confirmed by the experimental BET results listed in Table 4.2c, where the average pore diameters fall within the mesoporous range of 2-50 nm[106]. Of the isotherms shown, the pure titania (0% Zr) samples demonstrated a slight right-shift of their hysteresis loops towards higher relative pressures. A shift in capillary condensation towards higher pressures suggests an increase in pore width because a larger volume requires more pressure for condensation of the N_2 to occur. Indeed, the values presented in Table 4.2c confirm the larger average pore sizes of the pure titania samples compared to those of the doped (5% and 10% Zr) samples.
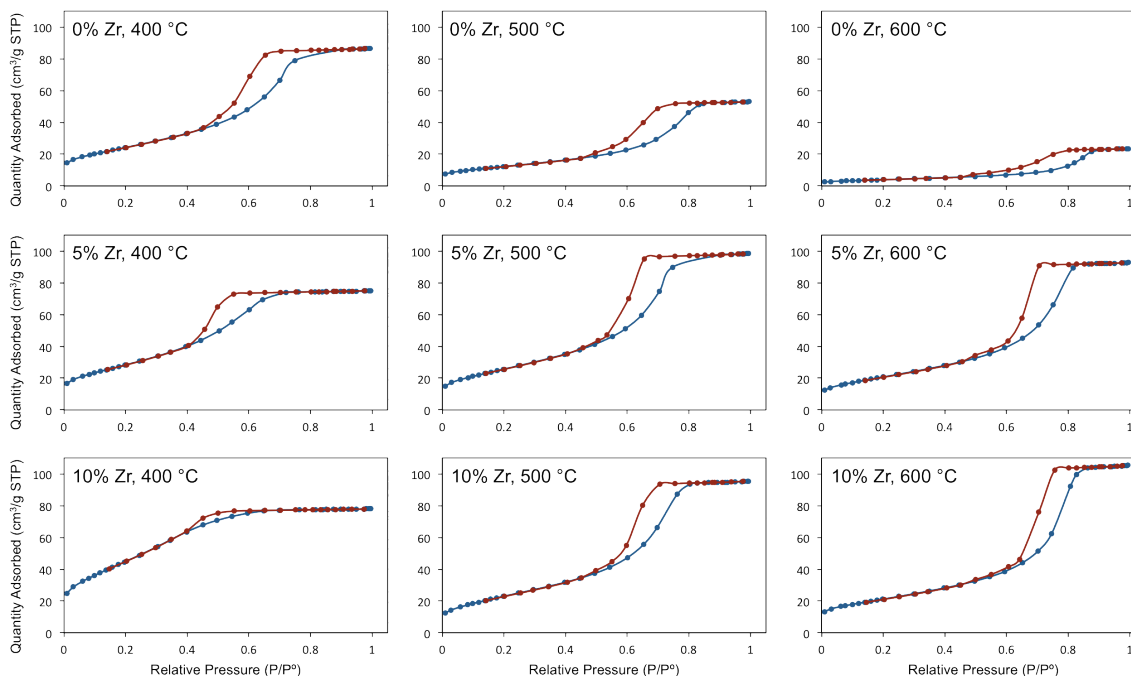
Figure 4.2: N$_2$ adsorption (blue curves) and desorption (red curves) isotherms of a selection of TiO$_2$ samples with various Zr doping concentrations calcined at various temperatures. Isotherms for samples with 15% Zr doping and samples calcined at 700 ºC are not shown, though they show similar trends.

Semiconductor crystallinity, which is critical for efficient electron transport in a DSSC, is achieved by calcination at high temperatures (~500 ºC). A large specific surface area is also necessary to maximize the amount of dye molecules that can adsorb onto the porous semiconductor substrate to allow for maximal sunlight absorption. Unfortunately, these are competing effects, as some surface area is inevitably lost during thermal treatment due to the porous semiconductor matrix collapsing on itself. The extent to which zirconia doping mitigates this tradeoff can be seen in the data obtained from the N$_2$ isotherms summarized in Table 4.2.

Table 4.2a compares the specific surface area (SSA) of the prepared samples at various doping concentrations and calcination temperatures. The highest SSA of 167 m^2/g was achieved with 10% Zr doping at 400 ºC. It can be seen that surface area is lowered as the

calcination temperature is increased at each respective doping concentration. The undoped TiO_2 sample (0% Zr) loses nearly all of its surface area (99%) at 700 ºC. The doped samples calcined at 700 ºC however experience considerably less structural collapse, with the 5% Zr sample retaining nearly half of its SSA. It can therefore be concluded that the SSA of TiO_2 is reduced to a considerably lesser extent during high-temperature treatment when it is doped with Zr, demonstrating the thermostabilizing properties of zirconia. The average particle and pore size results, summarized in Table 4.2b and Table 4.2c respectively, correlate well with the BET surface area data, where similar trends can be observed. As with the SSA, the sample with 10% Zr doping at 400 ºC also achieved the smallest average particle size and pore size. As with the surface area retention, the 5% Zr sample also demonstrated the best particle and pore size retention, exhibiting the best durability against thermal treatment.

Table 4.2: Experimental data obtained from N_2 physisorption of TiO_2 samples doped with 0-15% Zr and calcined between 400-700 ºC: a) Specific surface area; b) Average particle size; and c) Average pore size.

A - Surface area (BET) (m²/g)

T (°C)	0% Zr	5% Zr	10% Zr	15% Zr
400	87.9	103.5	166.8	149.0
500	44.2	93.9	85.9	65.9
600	14.3	75.7	76.4	62.2
700	1.0	48.8	54.0	51.5
SA Loss	99%	53%	68%	65%

B - Average particle size (nm)

T (°C)	0% Zr	5% Zr	10% Zr	15% Zr
400	68.3	58.0	36.0	40.3
500	135.8	63.9	69.9	91.1
600	420.5	79.3	78.6	96.4
700	5904.3	123.0	111.2	116.6
% Gain	8650%	212%	309%	290%

C - Average pore size (nm)

T (°C)	0% Zr	5% Zr	10% Zr	15% Zr
400	6.1	4.5	2.9	3.2
500	7.4	6.5	6.8	9.4
600	10.1	7.6	8.5	12.0
700	18.2	10.7	11.0	-
% Gain	299%	239%	382%	377%

For better visual representation, Figure 4.3 shows the variation in specific surface area as a function of dopant concentration. The TiO_2 samples produced in the absence of dopant have the lowest SSA at all temperatures. For each respective calcination temperature, the SSA generally increases with increasing Zr content. This is a consequence of the average particle sizes in each sample generally decreasing with higher Zr doping concentrations as a result of the zirconia's retarding effect on anatase crystallite growth[101]; doping suppresses nucleation of particles, keeping particle sizes small[104]. This correlates well with the above XRD data (see Figure 4.1a), which shows that the crystallinity of the TiO_2 samples improved with increasing Zr concentration, because the relative intensity of the diffraction peaks increased. Smaller particles are more easily crystallized than larger particles, which usually contain multiple crystallites.
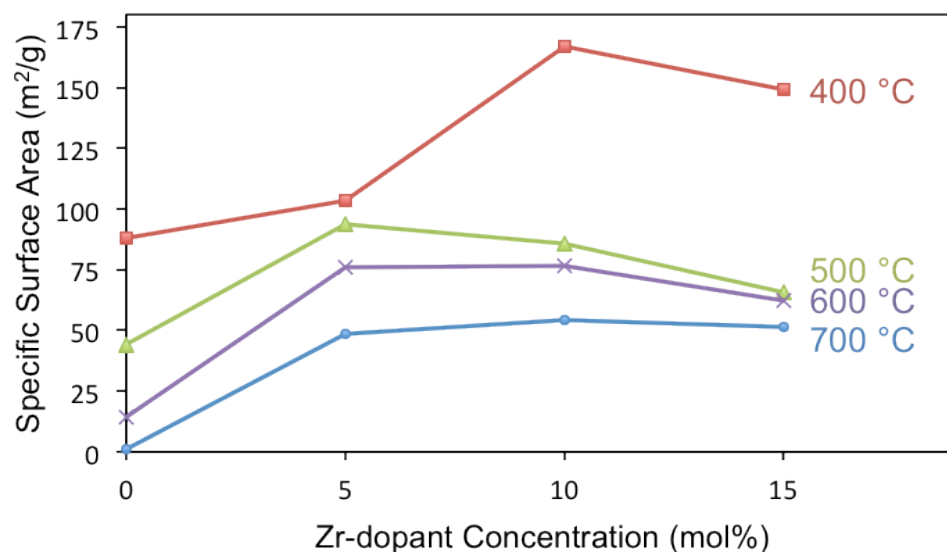
Figure 4.3: Specific surface areas of the Zr-doped TiO_2 samples as a function of dopant concentration.

The morphology of the samples was observed with a LEO 1540 scanning electron microscope (SEM). It can be seen from the SEM micrographs in Figure 4.4 that the porous nature of the TiO_2 and the spherical shape of the nanoparticles constituting the material did not change with increasing doping concentrations, though particle sizes did seem to decrease with higher Zr concentrations. For instance, at the highest doping concentration of 15% Zr, we can start to see slightly smaller particle sizes. This is consistent with BET analysis showing a general decrease in average particle size with increasing Zr doping concentration (see Table 4.2b). This is also in agreement with the findings in literature, where many studies have observed suppression in the crystal growth and an increased surface area as a consequence of Zr doping[104].
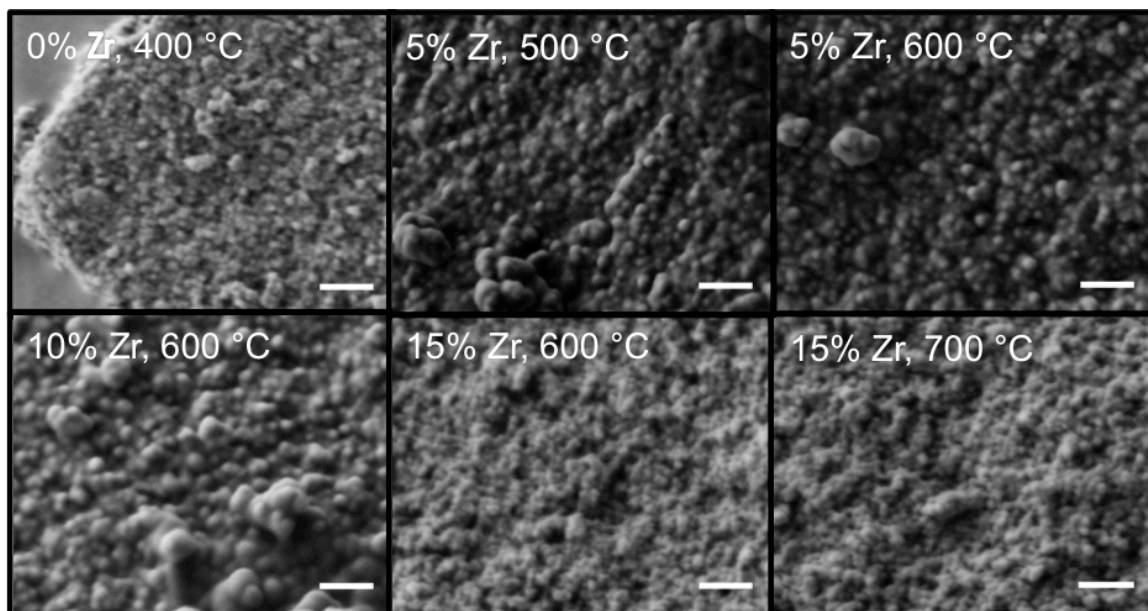
Figure 4.4: SEM images of a selection of TiO$_2$ samples with various Zr doping concentrations (0% to 15%) calcined at various temperatures (400-700 ºC). All image are magnified 50K times. The scale bars are 200 nm.

The SEM was equipped with an energy dispersive X-ray spectrometer (EDS), which was used to verify the elemental composition of the samples. EDS spectra of TiO$_2$ samples at 5, 10, and 15% Zr precursor doping concentrations are shown in Figure 4.5. The resulting values indicate the average atomic % of Zr detected in each sample, which was calculated against the amount of Ti present in the sample. The amounts of Zr detected correspond well to the intended doping percentages, suggesting that most of the precursors were fully reacted during synthesis. This confirms that there is a clear distinction in the doping concentrations, as corroborated by the XRD results. Osmium peaks are present in the spectra because the samples were coated with 2-3 nm of osmium before analysis to prevent charging. The samples in Figure 4.5 were calcined at 500 ºC, but elemental compositions agreed with doping concentrations at all calcination temperatures.
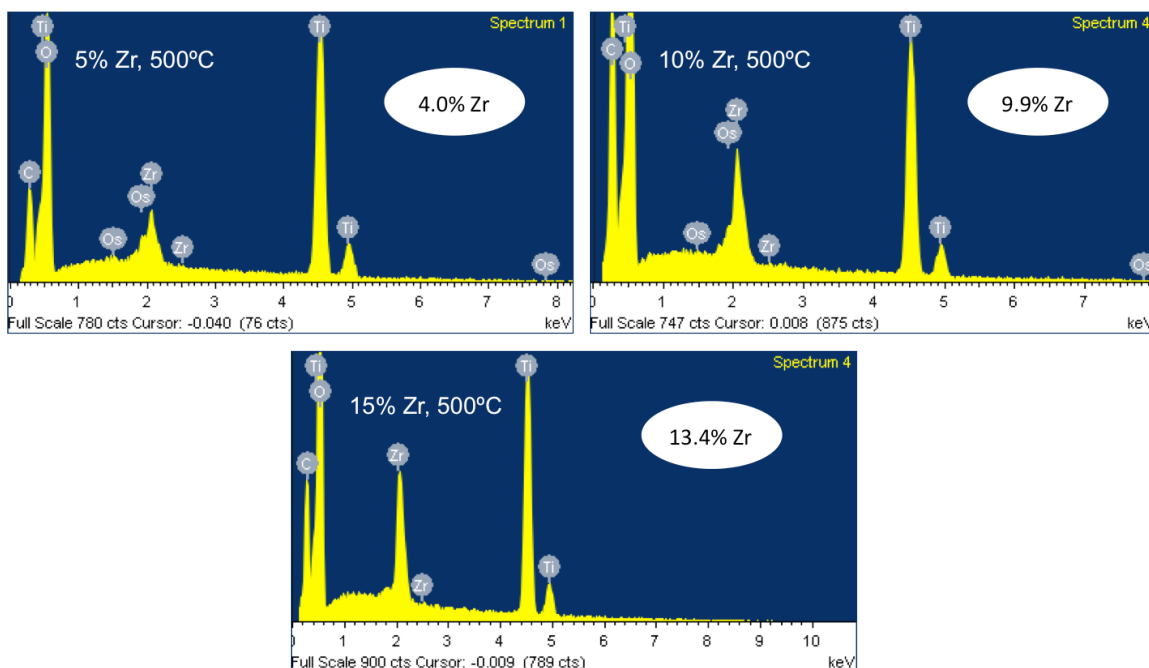
Figure 4.5: Energy dispersive X-ray spectra of 5, 10 and 15% Zr-doped TiO$_2$ samples calcined at 500 ºC.

4.3.2 Performance of DSSCs using Zr-Doped TiO$_2$

Dye-sensitized solar cells (DSSCs) were fabricated using the Zr-doped TiO$_2$ samples as the semiconducting layer of the cell. Cells were fabricated according to the procedure in section 3.3.1. For statistical purposes, 6 cells were fabricated for each sample, and the average of their performance taken to ensure representative results. The cells were tested under 1-sun simulated sunlight, and their IV characteristics were evaluated to identify any trends in performance. In total, 16 different photoactive layer compositions were tested: 4 different doping concentrations, each calcined at 4 different temperatures. Figure 4.6, compares the resulting cell efficiencies. With no doping (blue), cell efficiencies drop as expected; higher calcination temperatures cause the porous semiconducting structure to collapse, reducing the surface area and thus the potential dye adsorption sites, decreasing the light absorption capability of the cell. Upon addition of Zr ions into the TiO$_2$ matrix (red, green, purple), the trend of decreasing efficiency with

increasing calcination temperature is no longer observed. Rather, the efficiencies become relatively consistent at their respective doping levels, taking into account the error bars. These efficiencies correlate well with the specific surface areas listed in Table 4.2a. The best results were achieved with 5% doping, surpassing all other cells of different doping concentration, with the exception of pure TiO_2 at 400 ºC. This relates well with the data obtained from N_2 physisorption experiments, where 5% Zr samples demonstrated the best resistance to thermal degradation, achieving the best retention of surface area, particle size and pore size.
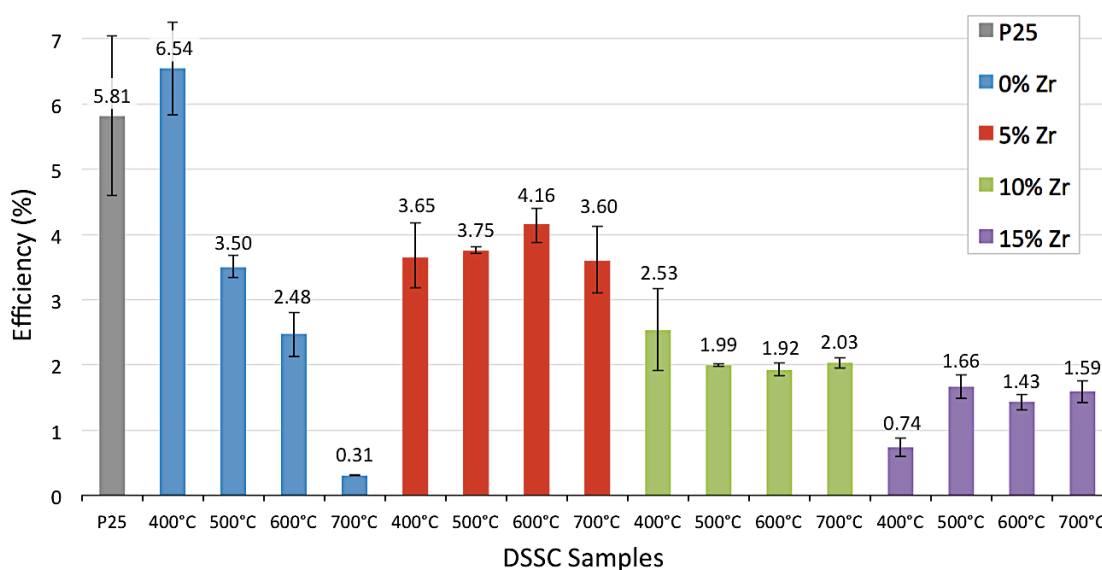
Figure 4.6: Performance of DSSCs containing the TiO_2 and Zr-doped TiO_2 samples as the semiconducting layer. Each value displayed is an average of 6 cell efficiencies for statistical consideration.

Figure 4.7 compares cell efficiencies by increasing doping concentrations at constant calcination temperatures, which allows us to see some trends that are less apparent in the 2D bar graph in Figure 4.6. At relatively low temperatures (400ºC), the addition of zirconia appears to progressively decrease efficiency. However at higher temperatures (500-700 ºC), the doping concentration and cell efficiencies no longer follow an inversely proportional relationship. For the cells tested at these higher temperatures, the best

performance was achieved with 5% doping. Furthermore, the difference in efficiencies between 0% and 5% doped samples increases with temperature, there being a more drastic difference in efficiencies as temperature is increased. It appears that the zirconia has a more positive effect as a dopant in TiO$_2$ when it is present at higher processing temperatures. This is relevant because many processing techniques require temperatures above 400 and 500 ºC. If a material is processed at low temperatures, zirconia doping may not be necessary. Yet if elevated temperatures are used, the addition of zirconia dopant to the material may help prevent thermal degradation and improve the overall product.
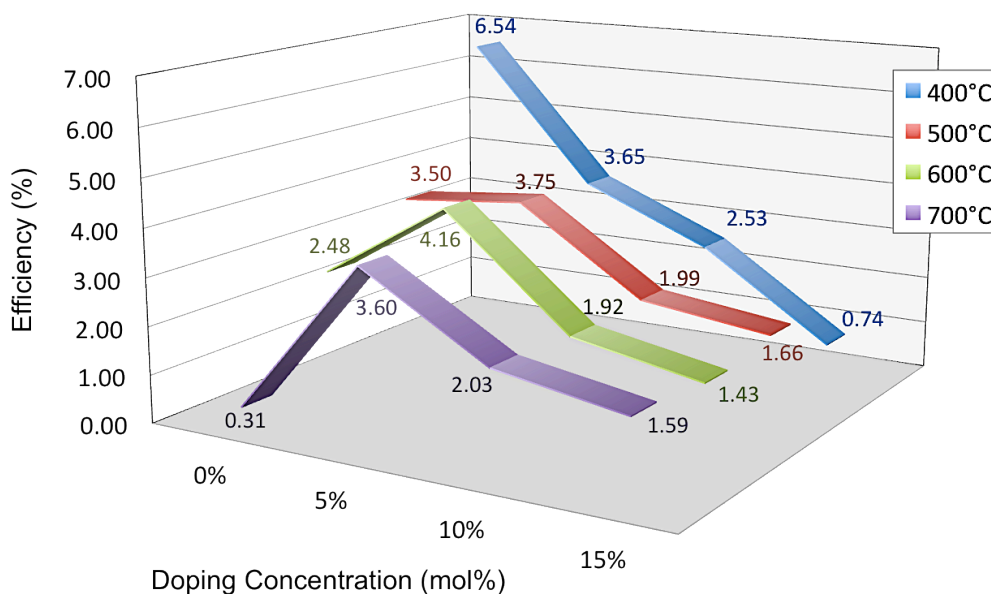
Figure 4.7: Performance of pure and Zr-doped TiO$_2$ DSSCs with respect to doping concentration.

The characteristic photocurrent density-voltage (J-V) curves of the samples are shown in Figure 4.8. The corresponding photovoltaic characteristics derived from the JV curves, including the open-circuit voltage (V$_{OC}$), short-circuit current density (J$_{SC}$), fill factor (FF) and energy conversion efficiency (η) are listed in Table 4.3. At low temperatures (400 ºC), pure titania (blue) achieved the highest average efficiency of 6.54% due to its high current density of 15.65 mA/cm^2. Without zirconia however, the titania crystal structure collapses when calcined at 700ºC (Figure d), diminishing viable surface area for

dye adsorption sites, and reducing its current density to 1.08 mA/cm^2. An addition of 5% zirconia helps the TiO$_2$ matrix preserve its structure at this high calcination temperature and maintain its surface area, evidence that zirconia induces thermal stability. The increase in the SSA, as confirmed by the BET data, allows for more electron pathways and increases the current density. The improved efficiency was indeed a result of enhanced photocurrent, as the V$_{OC}$ remained relatively consistent.
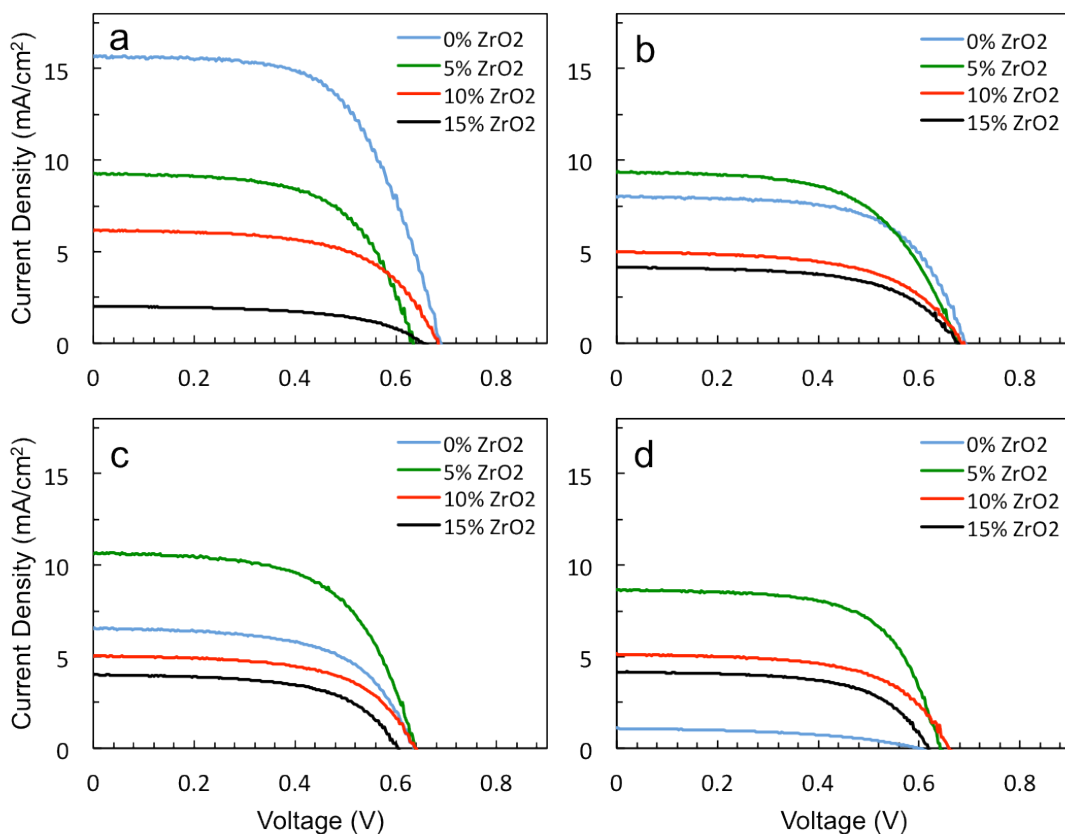
Figure 4.8: JV Curves for 0-15% Zr-doped TiO$_2$ DSSCs calcined at a) 400 ºC; b) 500 ºC; c) 600 ºC; d) 700 ºC.

Table 4.3: J-V characteristics of DSSCs containing 0-15% Zr doping.

Sample		V_{OC} (V)	J_{SC} (mA/cm^2)	FF	η (%)
400 °C	0% Zr	0.69	15.65	0.61	6.54
	5% Zr	0.63	9.26	0.62	3.65
	10% Zr	0.68	6.17	0.60	2.53
	15% Zr	0.65	2.02	0.55	0.74
500 °C	0% Zr	0.69	8.01	0.63	3.50
	5% Zr	0.67	9.34	0.60	3.75
	10% Zr	0.69	4.99	0.58	1.99
	15% Zr	0.68	4.16	0.59	1.66
600 °C	0% Zr	0.63	6.55	0.60	2.48
	5% Zr	0.64	10.66	0.61	4.16
	10% Zr	0.64	5.04	0.60	1.92
	15% Zr	0.60	4.01	0.59	1.43
700 °C	0% Zr	0.63	1.08	0.45	0.31
	5% Zr	0.65	8.65	0.64	3.60
	10% Zr	0.66	5.12	0.60	2.03
	15% Zr	0.62	4.19	0.62	1.59

15% Zr-doped DSSCs (black) performed poorly at all calcination temperatures. ZrO_2 has a wide band gap (~5.0 eV), and its reducing potential is more negative in its CB (and more-positive in its VB) relative to those of TiO_2[107]. This means that the bottom of zirconia's CB is ~1.3 eV higher than titania's CB, and the high doping concentration may be interfering with the electronic transport processes of the semiconducting layer by widening the already-wide band gap of TiO_2. If this is the case, the excited state of the dye molecules could be below the raised conduction band, and may be unable to inject electrons into the semiconducting CB as a result. The electrons therefore transfer back to the dye, increasing the amount of recombination occurring, which could explain the observed lower current density in the 15% Zr doped cells in comparison to their lesser doped counterparts.

Overall, the results demonstrate that performance was optimal at intermediate doping concentrations of Zr (5%). The samples showing the best performance were used as the base photoactive layer for future work with plasmon-enhanced DSSCs.

4.4   Conclusions

In summary, this work represents an extensive study on the optimal Zr-doping concentration needed for improved photovoltaic performance of dye-sensitized solar cells. We demonstrated that the addition of zirconia into the photoactive layer of DSSCs has a distinct positive influence on the thermal stability of the semiconducting oxide's pore structure, and consequently device performance.

TiO_2 samples at varying Zr doping concentrations and calcination temperatures were successfully synthesized using a modified sol-gel technique. XRD characterizations confirmed that Zr ions were incorporated within the crystal structure of TiO_2 forming one phase, which is beneficial for superior charge transport in DSSCs. The presence of Zr in the TiO2 matrix inhibited the anatase-rutile phase transformation, and stabilized the lattice at high temperatures. The binary oxide powder has a larger surface area than that of pure TiO_2. The 5% Zr samples demonstrated the best resistance to thermal degradation, achieving the best retention of surface area, particle size and pore size.

Solar simulation studies demonstrated that performance was optimal at intermediate doping concentrations (5% Zr), yet too much doping (15%) promoted recombination. The samples showing the best performance will be used as the base photoactive layer for future work with plasmon-enhanced DSSCs.

Chapter 5

5 The Effect of Zirconia Doping on the Performance of Plasmon-Enhanced DSSCs

5.1 Introduction

DSSCs are regarded as one of the most promising solar cell designs among third-generation PV technologies, particularly due to their low cost, easy preparation, and minor environmental impact with respect to earlier-generation devices[18,19]. Advances in their design[21,22], their incorporation onto flexible substrates[23–26] and their scalable fabrication techniques[14,27] have allowed DSSCs to move from the laboratory scale to real-life applications. Although their positive inherent features can facilitate their entry into the PV market, there is still a need for improvement to achieve higher performance DSSCs. One of the biggest contributors to efficiency loss in DSSCs is inefficient sunlight absorption[40]. The dye that sensitizes the TiO_2 photoabsorbing material does not respond equally to all the wavelengths that make up the visible solar spectrum[30]. This causes unbalanced light harvesting, limiting the amount of photons that can be converted into electricity.

Over the last two decades, there has been significant progress in the design and materials composition of DSSCs to improve their light harvesting capabilities, particularly in the field of plasmonics. A surface plasmon is a phenomenon that takes place in metal crystals when their electrons interact with an electromagnetic field. More specifically, it is the light-induced collective oscillation of free charge carriers at the interface between a dielectric material and a metal[40]. When the metal is in the form of nanoparticles, these oscillations are referred to as *localized* surface plasmons (LSPs). All metal NPs exhibit LSPs, because they all have free conduction electrons. For the purpose of solar energy harvesting, oscillations that correspond to frequencies of visible light (400-700 nm) are of interest. Silver (Ag) is an example of a metal that exhibits strong LSP resonance in the visible range of the solar spectrum[55,56]. That is, under illumination, its electronic oscillations resonate with the frequency of incident visible light, resulting in a large

increase in the intensity of the electric field and a strong confinement of that field at the nanoparticle surface. These unique optical properties of Ag NPs can enhance the light absorption capability of their surrounding environment, and several examples have been published that demonstrate enhanced photocurrents owing to their absorptive and scattering capabilities[43,54–56]. Ag NPs can therefore be exploited to improve the light absorption of dye molecules in DSSCs.

Although silver plasmonic nanostructures have been shown to amplify photoabsorption in DSSCs, there is a limitation to their enhancement capabilities because their resonance with incoming light also releases heat, which further contributes to local heating that is already a factor in the cell's proper operation. The electronic oscillations under resonant conditions can create a local electric field up to $\sim10^3$ times the incident field[75,76] and the local temperature on the plasmonic NPs' surface may exceed 500 °C[63]. This excessive heat can lead to cell degradation, an evidently unfavorable effect that has frequently been identified in literature[43,56,63]. For example, Qi *et al.*[43] observed a decrease in power conversion efficiency of their DSSCs when the concentration of silver plasmonic NPs (p-NPs) exceeded 0.6 weight %, a result of the p-NPs losing too much incident solar power to thermal energy. This observed effect poses a doping limit to the amount of p-NPs that can be incorporated into conventional photoanodes, thus imposing a limit on the cell's absorption improvement. Other sources also reported having observed doping limits when incorporating plasmonic nanostructures into their photoactive systems[56,61,62], or simply did not attempt doping concentrations above 0.5%. There are very few studies addressing the mitigation of plasmonic-NP doping limits, and even fewer addressing their effect on the performance of DSSCs.

According to several studies[77–81], a small amount of transition metal doping has been found very effective in improving the thermal stability and activity of TiO_2, the most common photoactive material used in DSSCs. Zirconia (ZrO_2) is one of these suitable dopants, known to have very high thermostabilizing properties[82,83]. ZrO_2 has one of the highest dielectric constants for metallic oxides[84] and therefore exhibits good optical properties. Additionally, it is very chemically stable due to its multi-electronic configuration, including its d-orbital electrons, characteristic of transition metals.

There are several explanations provided for zirconia's thermostabilizing properties on the anatase crystal lattice. For one, Ti and Zr are in the same group of elements (IVB), which gives them comparable physicochemical properties. However, Zr^{4+} ions are bigger in size and more electropositive than Ti^{4+} and are therefore more inclined to donate their electron density to O^{2-}. As a result, the neighbouring Ti-O bonds in the lattice become more stable and more difficult to break, increasing the lattice's stability at higher temperatures[103,104]. Zirconia's thermostabilizing properties can also be attributed to its relatively large band gap (~5eV), making it more of an insulator than TiO_2. These factors could prove useful in mitigating the heat created during plasmonic resonance. The use of ZrO_2 as a thermostabilizer in plasmon-enhanced DSSCs has yet to be investigated, but there is plenty of evidence showing that this material can help increase thermal stability and help preserve structure at high temperatures[85,86].

The purpose of this investigation is to examine the effects of incorporating ZrO_2 into plasmon-enhanced DSSCs with the goal of counteracting thermal energy loss and correspondingly increasing the allowable p-NP concentration without negatively affecting cell efficiency. In this study, two plasmon cell-architecture designs were fabricated and incorporated into DSSCs that contained 5, 10, and 15% Zr-doped photoanodes. The Zr-doped plasmon-DSSCs were compared to plasmon-DSSCs to see whether the presence of zirconia exhibited any thermostabilizing effects on the heat loss created by plasmon doping and whether the photovoltaic performance of the cells was improved as a result.

5.2   Experimental

Synthesis of Ag@TiO₂ nanoparticles

A one-pot synthesis was used to produce Ag@TiO_2 nanoparticles for use as absorption antennas within the 'chocolate-chip' design of DSSCs. Titanium(IV) isopropoxide, (TIP; 97%), acetylacetone (acac; >99%) and silver nitrate ($AgNO_3$, >99.9%) were purchased

from Sigma Aldrich. *N,N*-dimethylformamide (DMF; 99%), isopropanol (99.5%) and toluene (99.5%) were from Caledon.

The starting reaction mixture was prepared from two solutions. The first solution contained equimolar amounts of TIP and acac in isopropanol. A clear solution was obtained with mild sonication. The second solution was composed of 8.8 mM AgNO3 and 13.88 M H_2O in DMF. 40 mL of the first solution and 20 mL of the second were transferred to a round-bottom flask and stirred for 10 minutes, before being heated to 65 ºC and refluxed for 1 hour. The colloid began as a yellow solution and gradually attained a green-black coloration as the reaction progressed. The colloidal material was precipitated by the addition of toluene, and then redispersed in isopropanol by sonication. This process was repeated three times to remove DMF and impurities formed in the reaction. The solvent was evaporated, and the dried powder ground to yield $Ag@TiO_2$ nanoparticles. The shell thickness was varied by increasing the TiO_2 precursor concentration, keeping the reaction time constant. TIP concentrations of 20, 40 and 80 mM were attempted.

Synthesis of neat Ag nanoparticles

Neat Ag NPs were used as a component of the 'blanket-array' electrodes. A procedure for the reduction of silver oxide by hydrogen gas in water was adapted from Evanoff *et al.*[94] where neat Ag NPs were synthesized in a saturated silver oxide aqueous solution at elevated temperature in equilibrium with hydrogen gas at elevated pressure. Silver(I) oxide (Ag_2O, 99.99%) was purchased from Alfa Aesar and water was of Milli-Q (ultrapure) grade. 5% (N_2 balance), 10% (Ar balance) and pure hydrogen gas (H_2) were purchased from PraxAir.

In a typical reaction, 0.3 g of Ag_2O were added to 300 mL of ultrapure water and stirred vigorously. The mixture was then simultaneously heated to 70 ºC in an oil bath and the vessel flushed with Ar gas at 10 psi, without further agitation. Once the temperature was reached, the vessel was put under a hydrogen atmosphere and pressurized to 10 psi. Within a few minutes, the contents of the vessel became a faint yellow in colour,

indicating the formation of Ag NPs. Aliquots were taken at regular intervals throughout the reaction to monitor the growth of the nanoparticles. The contents of the vessel continued to darken as the reaction progressed, indicating the size increase of the Ag NPs. Releasing the gas from the vessel stopped the reaction.

Preparation of blanket-array electrodes

In the blanket-array design, neat Ag NPs, coated with a thin layer of TiO_2, were used primarily as nano-mirrors within the DSSC to increase the optical path length. FTO electrodes (thickness, 2.2 mm; sheet resistance, 7 Ω/sq) were purchased from Solaronix. Sulfuric acid (H_2SO_4, 98%) was purchased from Caledon. Hydrogen peroxide (H_2O_2, 30 wt. % in H_2O) and poly(4-vinylpyridine) (P4VP, average MW ~60,000) were purchased from Sigma-Aldrich.

To prepare a 'blanket-array' electrode, FTO-coated glass electrodes were first cleaned with piranha solution (3:1 H_2SO_4:H_2O_2) for 30 minutes at room temperature. This treatment not only removes all organic contaminants from the FTO surface, but also leaves it with a high surface energy by introducing hydroxyl groups. The electrodes were then thoroughly rinsed with deionized water before being blown dry with Ar gas. The cleaned FTO substrates were functionalized with P4VP by soaking them in an ethanolic solution of 2 wt % P4VP for 3 hours. The electrodes were then rinsed with ethanol to remove any unadsorbed polymer and heated in an oven for 1 hour at 100 ºC (20 ºC/min ramp). This is meant to relax the monolayer of P4VP to facilitate the even distribution of Ag NPs on the surface. The P4VP-functionalized electrodes were then soaked in the synthesized Ag suspensions for 12 hours, after which the Ag-functionalized electrodes were rinsed with deionized water and dried with Ar gas. A Savannah 100 Cambridge Nanotech atomic layer deposition (ALD) instrument was used to create a uniform layer of TiO_2 on the Ag-NP array.

In order to form a pinhole-free (i.e. fully protective) TiO_2 layer, 300 cycles of TiO_2 precursor were needed, unless 2 cycles of an aluminum oxide (Al_2O_3) adhesion layer were first deposited, in which case only 211 cycles of TiO_2 precursor were necessary. Both precursor formulations were used to determine which formulation showed superior

performance in DSSCs. For TiO_2 deposition, alternating 0.1-second pulses of the precursors titanium isopropoxide (TIP) and H_2O were used to form TiO_2 layers, and alternating 0.015-second pulses of trimethyl aluminum (TMA) and H_2O were used for Al_2O_3 deposition. The precursors were held in the deposition chamber for 1 s before a 12 s pump. The chamber temperature was set to 200 ºC, and the N_2 flow rate was 20 sccm. TIP was held at 80 ºC and all other precursors were used at RT.

Characterization

A Shimadzu UV-3600 UV-Vis-NIR spectrophotometer was used to measure the extinction spectra of Ag NPs aliquots sampled throughout their synthesis reaction within the spectral range of 300 to 700 nm.

The compositions of $Ag@TiO_2$ samples were characterized with a LEO-Zeiss 1540 XB SEM equipped with an Oxford Instruments x-ray system allowing for in-situ elemental mapping and analysis (EDS). Before analysis, samples were sputtered with 2-3 nm of Osmium using a coating machine to prevent surface charging. SEM was also used to examine the size and dispersion of Ag NPs, and the individual layers of 'blanket-array' electrodes to ensure successful assembly. A Kratos AXIS Ultra X-ray photoelectron spectrometer (XPS) employing a monochromatic Al Kα X-ray source was used to confirm the surface composition of each layer of the prepared 'blanket-array' electrodes.

The crystallinity of the $Ag@TiO_2$ nanoparticles was analyzed by X-ray powder diffraction (XRD) using a Bruker AXS D2 Phaser diffractometer with Cu Kα radiation. The standard reference cards JCPDS 04-0783 and JCPDS 00-021-1272 were used for identification of the Ag-core and TiO_2-shell crystal structure, respectively.

Initial morphology and particle size measurements of $Ag@TiO_2$ nanoparticles were observed on a Phillips CM10 tunneling electron microscope (TEM) with a digital camera output, operating at 80 kV. High resolution TEM (HRTEM) was carried out on a FEI Titan 80-300 LB at 200 kV to inspect the fine nanostructure of the plasmonic NPs. To obtain specimens for TEM and HRTEM analysis, samples were re-dispersed in ethanol, and then the diluted solution was drop-cast onto ultrathin carbon-coated copper grids

(holey carbon support film, 400 mesh, Cu, Ted Pella, Inc.). The grids were dried at ambient conditions one day prior to observation. The HRTEM system was also fitted with an electron energy loss spectrometer (EELS, Gatan 865 model) capable of 0.25-eV electron resolution. Electron energy loss spectroscopy (EELS) was used to determine the elements comprising the core-shell structure of the nanoparticles.

DSSCs were fabricated according to the procedure described in section 3.3.1. Plasmon-doped DSSCs were fabricated in the same manner. The only modification to the fabrication of 'chocolate chip' cells was in paste preparation, where the applicable amount of Ag@TiO$_2$ powder was added to the TiO$_2$ (or Zr-doped) powder in the mortar and mixed with the solvent to create a plasmon-doped paste. The only modification to the fabrication of 'blanket array' cells was in the glass electrode preparation, where the FTO glass was functionalized with Ag NPs and coated with TiO$_2$ via ALD, before having the photoactive TiO$_2$ paste doctor bladed onto them. The power conversion efficiency of the cells was measured using the simulated illumination of a Newport Oriel 92250A-1000 solar simulator and a Keithley 2420 digital source meter.

5.3   Results and Discussion

Two photoactive cell layer designs were fabricated and their performance in DSSCs compared to see which architecture delivered a better photovoltaic efficiency. As can be seen in Figure 5.1, the "chocolate chip" design (a) has Ag@TiO$_2$ NPs distributed throughout the photoactive 'cookie batter' cell layer, while the "blanket-array" design (b) has Ag NPs functionalized onto the photoelectrode, upon which a uniform sheet (blanket) of TiO$_2$ is deposited by atomic layer deposition (ALD). Both proposed architectures offer different strategies to couple Ag@TiO$_2$ plasmonic nanocrystals to the photoactive layer of DSSCs to maximize light absorption efficiency.
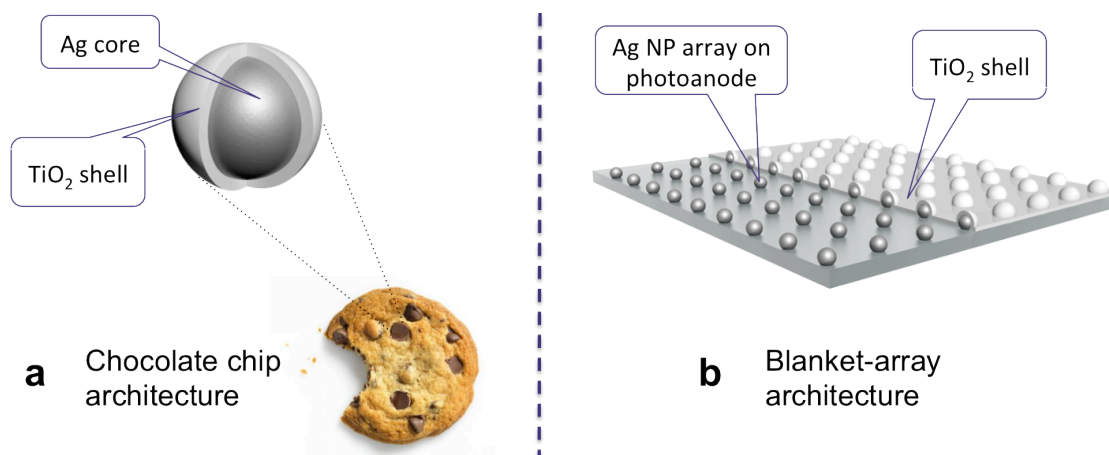
Figure 5.1: Schematic diagrams depicting the proposed photoactive cell layer designs: a) the 'Chocolate chip' architecture, and b) the Blanket-array architecture.

In the chocolate chip design, Ag@TiO$_2$ NPs are used primarily as absorption antennas within the DSSC. By efficiently converting free-propagating optical radiation into localized energy, the plasmonic near-field is coupled to the dye, increasing its effective absorption cross-section. Since the rate of electron excitation in the dye is proportional to the local light intensity[42], this effect encourages the creation of more electron-hole pairs, which should lead to higher photocurrent. In the blanket-array design, Ag@TiO$_2$ NPs are used primarily as nano-mirrors to trap freely propagating solar plane waves by preferentially scattering incoming light into the TiO$_2$ thin film[69]. The captured light acquires an angular spread in the TiO$_2$ absorbing layer, which increases the optical path length.

In each architecture, both the amplification of electric field near the Ag NPs' surface and the increased scattering within the active layer increases the amount of dye molecules reached by light. This thesis work aims to determine the best cell design for incorporating Ag@TiO$_2$ NPs into DSSCs.

5.3.1 Characterization of Ag@TiO$_2$ Nanoparticles for the 'Chocolate-chip' Architecture of DSSC Photoanodes

Ag@TiO$_2$ NPs were synthesized via the simultaneous reduction of silver ions by DMF and the direct growth of a TiO$_2$ shell on the surface of the silver nanocrystals by hydrolysis and condensation of the TiO$_2$ precursor Titanium (IV) isopropoxide (TIP). The shell thickness was varied by increasing the TiO$_2$ precursor concentration while keeping the reaction time constant. TIP concentrations of 20, 40 and 80 mM were attempted.

Energy dispersive X-ray spectra (EDS) were obtained in order to identify the compositional ratios of elements in the Ag@TiO$_2$ samples. Figure 5.2 shows the atomic % of the elements Ag, Ti and O detected by EDS analysis. The values displayed for each sample is an average of three sample areas tested. A small percentage of carbon and osmium were present in the samples, but are not shown.

The results suggest the existence of a core and shell structure. All samples presented consistent titanium and oxygen percentages, with the ratio of O to Ti being approximately double, suggesting the presence of TiO$_2$ in the sample. A trend of decreasing Ag content with increasing shell precursor concentration can be seen. More specifically, the % of Ag decreases by about half each time the TIP precursor concentration doubles, which is in agreement with the TiO$_2$ shell becoming twice as thick, shielding the silver X-ray signals from reaching the detector. In this technique, the electron beam penetrates up to ~1 μm of the sample, so the Ag cores can indeed be detected since the shells are thinner than 1 μm, although the collected signals are low due to the TiO$_2$ shells coating the Ag cores screening the signals.
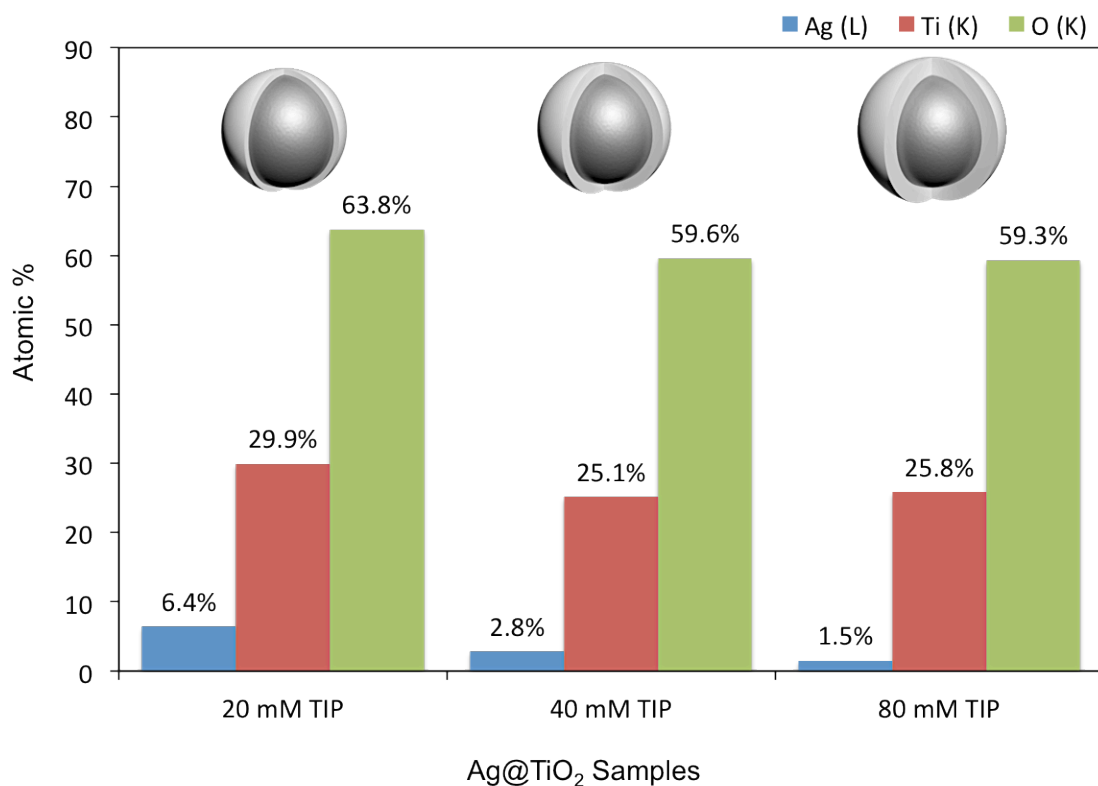
Figure 5.2: Atomic percentage of the elements Ag, Ti and O detected by EDS in the Ag@TiO$_2$ samples of varying shell precursor concentrations.

The crystallinity of the Ag@TiO$_2$ nanoparticles was examined by XRD. Figure 5.3 shows the diffraction patterns of the Ag@TiO$_2$ NPs with varying shell thicknesses, before and after calcination. No anatase TiO$_2$ peaks are observed in any as-prepared sample, suggesting that the titania shell was amorphous before calcination. The as-prepared 20 and 40 mM TIP samples (red and green dashed lines) have visible peaks at 38.0, 44.0, 64.5 and 77.5° corresponding to the (111), (200), (220) and (311) planes of cubic silver (JCPDS #04-0783), suggesting partial crystallinity of the Ag cores. These Ag peaks are not seen in the uncalcinated 80 mM TIP sample (blue dashed line), which may be due to the amorphous titania shell being too thick. Upon calcination at 500 °C for 1 hour (solid lines), additional peaks are observed corresponding to anatase TiO$_2$ (JCPDS 21-1272), indicating that the shells were converted to crystalline oxides upon thermal treatment. Therefore, it can be concluded that calcination of the synthesized Ag@TiO$_2$ NPs is

required to obtain crystallinity of the TiO$_2$ shells, which is necessary for efficient electron transport through the semiconducting layer of DSSCs.
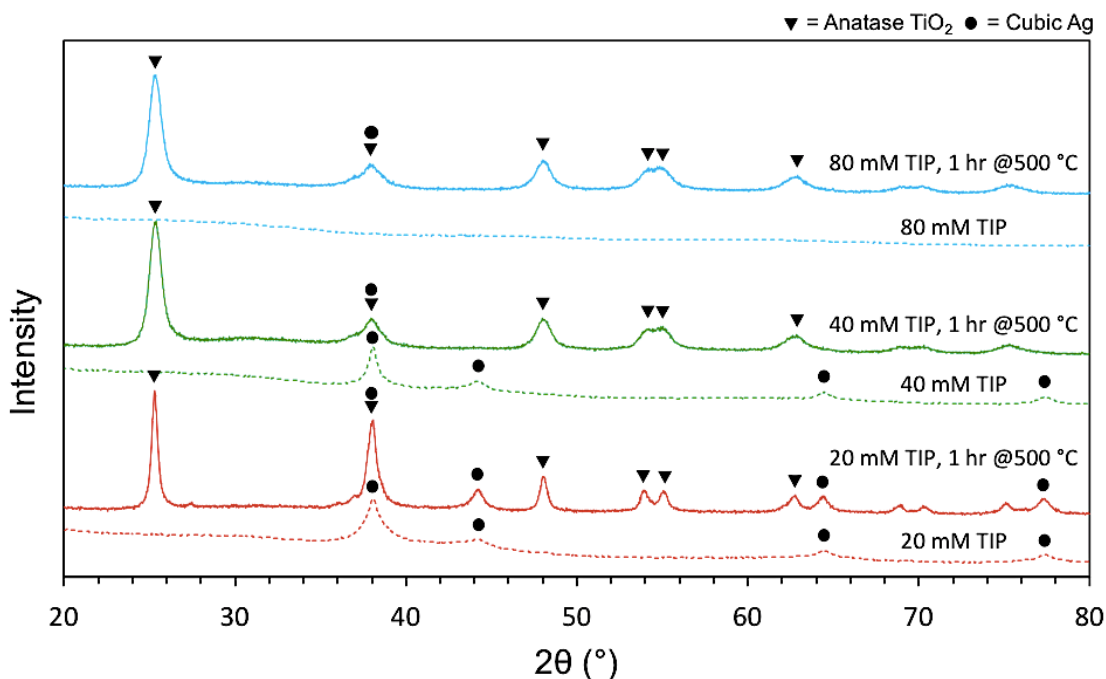
Figure 5.3: XRD patterns of Ag@TiO$_2$ NPs as synthesized (dashed lines) and after calcination at 500 ºC for 1 hour (solid lines). The inverted triangle symbols indicate the XRD patterns for anatase TiO$_2$, and the circles indicate the XRD patterns for cubic Ag.

The peaks characteristic of anatase TiO$_2$ at around 36-38º overlap with a cubic silver peak at 38º in the calcined samples. We know that in the uncalcinated sample, the peak at that diffraction angle belongs to Ag and not TiO$_2$ because no peak was detected at 25º, which is the strongest diffraction peak for anatase TiO$_2$, and would have been the first peak to appear in the event of any anatase crystallinity. The other Ag peaks in the calcined samples only show up clearly through the thin shell of 20 mM TIP Ag@TiO$_2$ NPs (red), and are muffled by the anatase signal in the thicker-shelled samples, as can be seen at 44 º, 64.5 º and 77.5 º. Therefore the crystallinity of the Ag NPs is also improved by calcination, though their signals get obscured by the strong anatase signals of thicker shells.

The morphology and particle size distribution (PSD) of the three different samples of varying shell thicknesses after calcination can be seen in the TEM images and corresponding histograms shown in Figure 5.4. The particle morphology for all samples was generally spherical. The average particle size (APS) for the 20 mM TIP sample (thinnest shell) was 5.5 nm, smaller than the ~20 nm size expected from literature[64,91]. The APS for the 40 mM shell concentration was expectedly larger than that of the 20 mM sample. The TEM image for the 80 mM sample showed agglomeration, suggesting that the TIP concentration was too high. The 20 mM sample offers the largest surface area because it is made up of the smallest particles. A large surface area can contribute to higher cell efficiencies because the more surface area there is for dye molecules to adsorb onto, the more sunlight the cell can absorb.

The PSD was not particularly narrow amongst the non-agglomerated samples. This is in fact beneficial for increasing a DSSC's light absorption since a wide PSD exhibits greater light scattering[63,108], increasing the likelihood of photons to be absorbed in the photoanode during illumination. This eliminates the need to synthesize plasmonic NPs with a very narrow size range, which can be challenging and/or may require the need for multiple filtration steps.
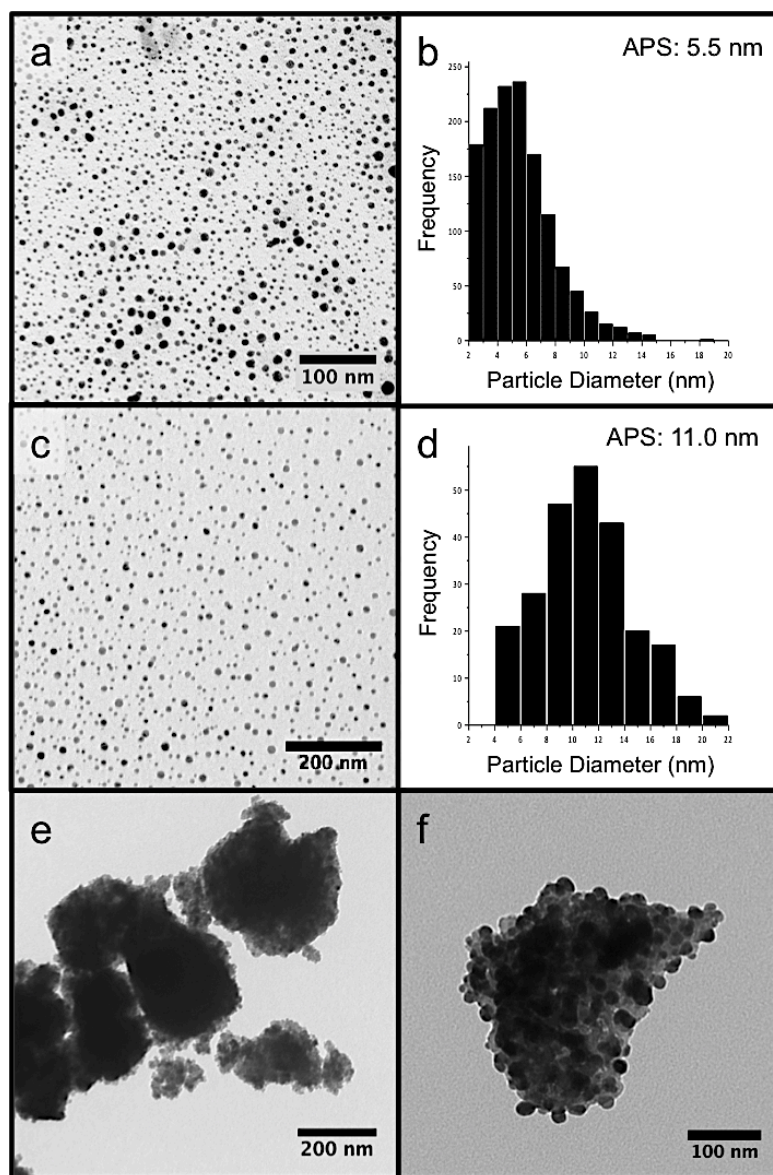
Figure 5.4: TEM images and corresponding histograms for Ag@TiO$_2$ nanoparticles. (a,b) 20 mM TIP sample; (c,d) 40 mM sample; (e,f) The 80 mM TIP sample does not have a corresponding histogram because particles were agglomerated.

The fact that the nanoparticles for the 20 mM and 40 mM TIP samples did not agglomerate suggests that the Ag cores were coated with a TiO$_2$ shell. A shell layer protects the Ag cores from aggregating and forming larger particles during the calcination process. The TiO$_2$ shell also physically isolates the Ag cores from the electrolyte, which

would readily etch and corrode unprotected metal during cell operation. The TEM image in Figure 5.5a shows the spherical, well distributed 40 mM TIP plasmon NPs, with sizes around 5-10 nm, but the magnification capability of a regular TEM however cannot display crystallinity or discern a core-shell structure. High resolution TEM was therefore used to measure shell thickness and distinguish between the shell and core structure of synthesized Ag@TiO$_2$ NPs. The same spherical morphology of a 40 mM TIP plasmon NP with a similar size can be seen in the HRTEM image in Figure 5.5b, with the addition of an orb-like shell around the particle. Unfortunately, assuming this layer to be the titania shell would be incorrect, as no crystallinity can be seen in the shell structure that would surely show some crystallinity after calcination at 500 ºC if it were TiO$_2$. The fact that the grid was not plasma cleaned before imaging also suggests that the shell-like structure could be organic residue leftover from the synthesis instead of TiO$_2$. Indeed, during the separation step of the synthesis, the Ag@TiO$_2$ nanoparticles were precipitated with toluene, which is notorious for leaving a stubborn residue. After plasma cleaning (Figure 5.5c), a core-shell structure was no longer visible.

The HRTEM system was also fitted with an electron energy loss spectrometer (EELS, Gatan 865 model) capable of 0.25-eV electron resolution. EELS was used to perform elemental mapping of the elements comprising the nanoparticles that were now revealed not to have a core-shell structure. As there was no protective shell, imaging the sample at the extremely high voltage required for EELS (300 kV) caused the particles to melt and agglomerate when exposed to the beam. This caused a complete distortion of the size and shape of the particles, as can be seen in Figure 5.5d, where the silver (brighter spots) is distributed amongst the (darker) TiO$_2$. Thus, the coating of the Ag metal nanoparticles with TiO$_2$ has proven difficult to achieve, which could be attributed to the fast nucleation of titanium precursor during the synthesis[63]. Alternatives to synthesizing core-shell nanostructures should be investigated.
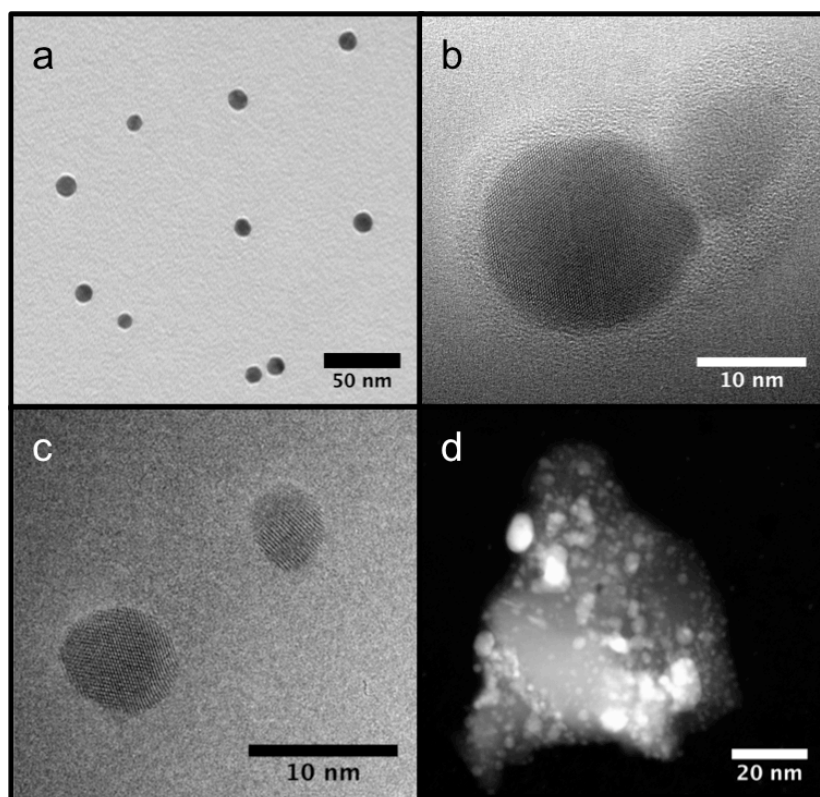
Figure 5.5: TEM (a) and HRTEM (b-d) images of Ag@TiO$_2$ NPs. Figure (a) is taken at 80 kV, (b) and (c) are taken at 200 kV, and (d) is taken at 300 kV. The appearance of a shell (b) disappears after plasma cleaning (c).

5.3.1.1   Performance of 'Chocolate-Chip' architecture DSSCs

Dye-sensitized solar cells (DSSCs) were fabricated according to the procedure in section 3.3.1, using Zr-doped TiO$_2$ samples synthesized in Chapter 4 as the photoactive material. In this 'chocolate-chip' cell architecture, Ag@TiO$_2$ NPs were dispersed throughout the photoactive layer of the cell. The cells were tested under 1-sun simulated sunlight.

The current density-voltage (J-V) curves for 80 mM TIP Ag@TiO$_2$ plasmon-enhanced 'chocolate-chip' DSSCs containing 10% Zr in the photoactive layer are shown in Figure 5.6. The Ag@TiO$_2$ NPs with the 'thickest shell' formulation were used to see how well they could disguise themselves as regular TiO$_2$ nanoparticles. A 15% improvement in efficiency from 1.24% to 1.46% can be seen by doubling the plasmon doping

concentration from 0.3% to 0.6%, and tripling the original plasmon concentration to 0.9%, results in another slight increase in efficiency to 1.57%. The inset lists the PV characteristics derived from the J-V curves, including the open-circuit voltage (V_{OC}), short-circuit current density (J_{SC}), fill factor (FF) and energy conversion efficiency (η). Despite HRTEM revealing that the Ag NPs were unprotected, doubling the plasmon doping concentration from 0.3 to 0.6% still increased the photocurrent, a sign of better carrier extraction. Electrons have a higher chance of escaping recombination when they move within an electric field by migration, rather than the slower diffusion process in the absence of a field[109]. The localized surface plasmons (LSPs) of Ag NPs provide this local field. These results suggest that the concentration of unprotected Ag NPs was still low enough that the plasmonic benefits (i.e. intensified local EF) outweighed the cost of exposed Ag acting as recombination sites for electrons.

Sample	V_{OC} (V)	J_{SC} (mA/cm^2)	FF	η (%)
0.3% Ag@TiO2	0.62	3.56	0.56	1.24
0.6% Ag@TiO2	0.62	4.12	0.56	1.46
0.9% Ag@TiO2	0.65	4.11	0.58	1.57
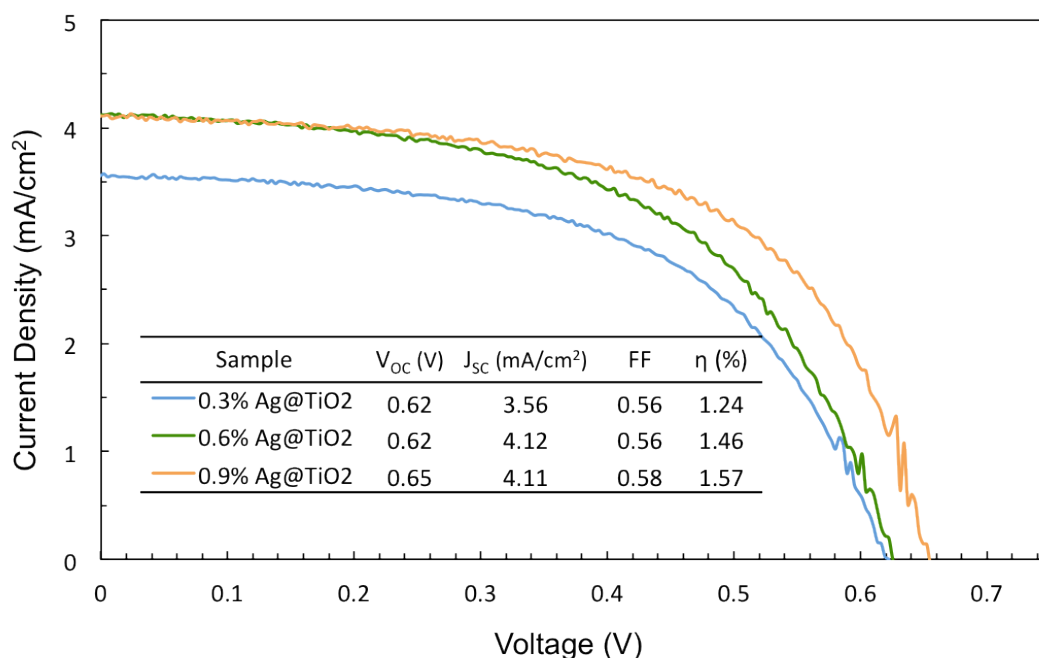
Figure 5.6: Current density–voltage curves for 10% Zr-doped DSSCs containing various concentrations of 80 mM TIP Ag@TiO$_2$ plasmonic nanoparticles. The inset shows the characteristic values corresponding to the curves. The DSSC design used was the 'chocoate-chip' architecture.

Tripling the plasmon concentration to 0.9% showed improvement in the V_{OC}, but the J_{SC} began to fall. The higher V_{OC} was expected, and reveals that the LSPs of Ag@TiO$_2$ NPs were indeed working as light absorption antennas, intensifying the local electric field felt by the dye and encouraging more efficient electron-hole separation. However, the lack of improvement in the J_{SC} is an indication that the extra charge carriers being created were not actually being extracted into the external circuit, but were rather recombining with the exposed Ag. This suggests that the concentration of unprotected Ag NPs reached a level where the cost of recombination outweighed the plasmonic benefits.

For curiosity, the plasmon doping concentration in the 10% Zr-doped DSSCs was increased until the photoactive material was solely composed of Ag@TiO$_2$ NPs. The power conversion efficiencies (PCE) of these cells are compared in Figure 5.7. Confirmation by HRTEM and EELS analysis that a core-shell structure did not in fact exist can help explain the global dampening of efficiencies observed relative to the plasmon-free control cell that achieved a PCE of 2.53%. The silver, being in direct contact with the electrolyte that permeated the porous TiO$_2$ film, created electron recombination sites, and prevented electrons from being extracted out into the circuit. Therefore, unprotected Ag NPs did more harm overall than good. Although the plasmon-doped cells performed relatively poorly compared to the control, a local improvement in efficiency with increased plasmon doping was still observed. The efficiency kept improving up to 5% doping, after which the efficiency began to decline. It is fitting that the lowest efficiency of 0.69% was achieved with 100% doping, as there was no zirconia present in the photoactive layer to thermostabilize the material. It can therefore be concluded that including zirconia into the photoactive layer permitted the plasmon-doping threshold to be increased past 0.6% before succumbing to a decrease in efficiency.
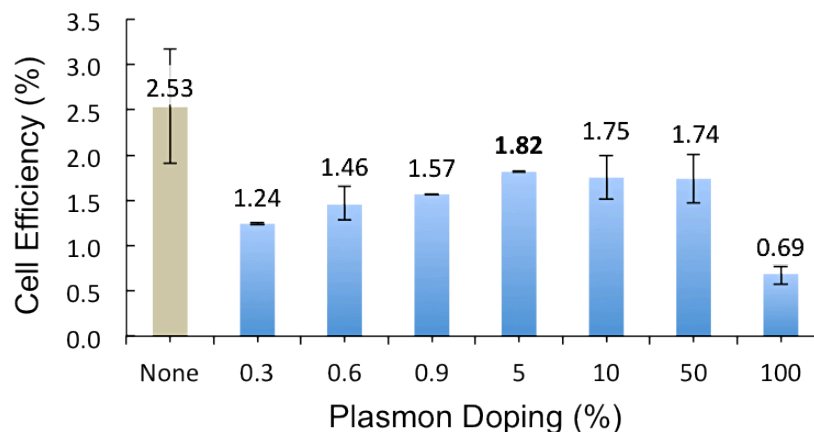
Figure 5.7: The effect of increasing the concentration of Ag@TiO$_2$ (80 mM TIP) NPs on the performance of 10% Zr-doped DSSCs.

Although it may be argued that these observed improvements are not statistically significant, at the least, it is shown that the efficiency was maintained upon addition of plasmonic NPs. This is therefore still an improvement on the results in previous literature[43], showing that a higher loading of plasmonic NPs can be incorporated into a zirconia-doped TiO$_2$ photoactive layer without negatively impacting the cell's PCE.

Having studied the effects of zirconia and silver plasmon NP doping in DSSCs individually, the effect of their concurrent presence on the performance of DSSCs was evaluated. Figure 5.8 compares the efficiency of DSSCs doped with Zr and Ag@TiO$_2$ NPs individually, as well as concurrently. The Ag@TiO$_2$ NPs used in the 'chocolate-chip' architecture DSSCs were composed of 20 mM TIP shell precursor. Because the plasmon NPs were discovered to not have a core-shell structure, the plasmon doping was kept at 0.6%, as the above results demonstrated that electron recombination was still negligible at this concentration. The Zr-doped cells contained 5% Zr, as this was determined to be the optimal zirconia concentration in the previous chapter. The photoactive material of all cells was calcined at 500 ℃. It can be seen that the zirconia had a very positive impact on the plasmonic cell's performance, improving the PCE by 44%, from 4.38 to 6.32%. The improvement in conversion efficiency reflects the variance of J$_{SC}$, as can be seen in the inset table.
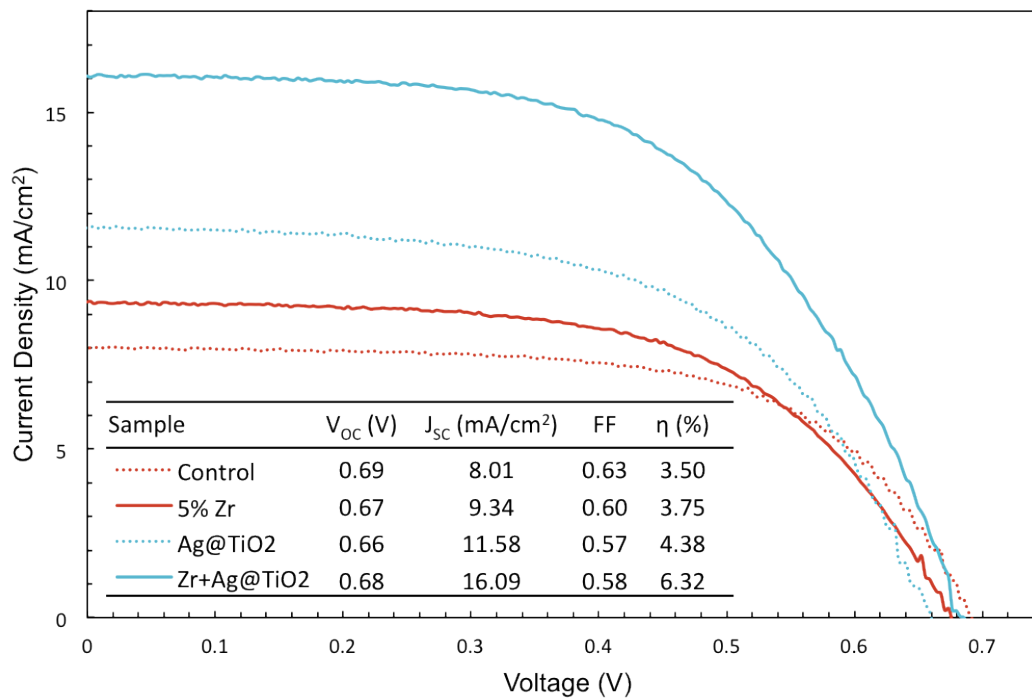
Figure 5.8: The effect of Zr and plasmon doping on the J-V curves of 'chocolate-chip' architecture DSSCs. The inset shows the characteristic values corresponding to the curves.

Another observation is that the FF values of the 'chocolate-chip' cells (blue curves) were lower than that of the plasmon-free cells (red curves), which reflects less efficient charge transport within the cell. Efficiencies (η) would likely have been higher if the Ag@TiO$_2$ NP synthesis had been successful and the silver would not have been exposed to the electrolyte during cell operation, creating electron recombination sites.

5.3.2 Characterization of Ag Nanoparticles for the 'Blanket-Array' Architecture of DSSC Photoanodes

Silver nanoparticle solutions were prepared through the reduction of silver(I) oxide by hydrogen gas in water. H_2 concentrations of 5, 10 and 100% were attempted as the vessel's atmosphere. A custom spout was made to facilitate the retrieval of aliquots at regular intervals throughout the reaction to monitor the growth of the NPs without depressurizing the vessel. The contents of the vessel continued to darken as the reaction progressed, indicating the size increase of the Ag NPs. Reactions proceeded much quicker with a higher H_2 atmospheric concentration, with pure H_2 reduction solutions reaching the same colour as a completed 5% H_2 reaction (230 minutes, right-most vial in Figure 5.9) after only 30 minutes. The colloidal Ag suspensions obtained from the pure H_2-atmosphere reduction reaction were used to functionalize FTO glass electrodes with Ag NPs to make 'blanket-array' plasmon DSSCs.
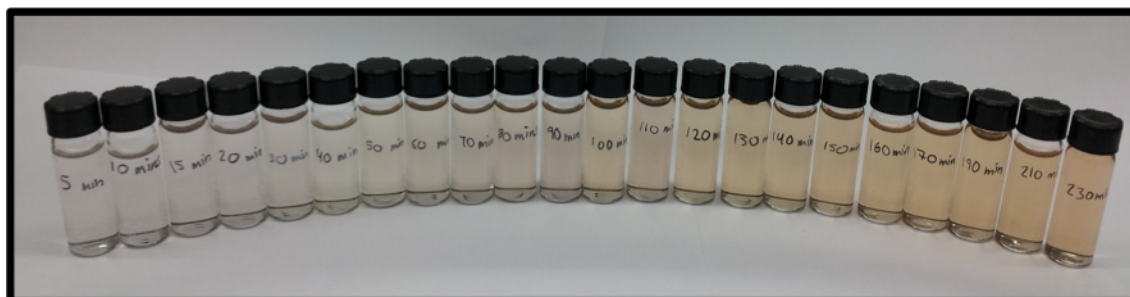
Figure 5.9: Colour evolution of Ag-suspension aliquots taken at regular intervals throughout a 5% H_2 reduction reaction of ~4 hours.

UV-vis spectrometry was used to measure the extinction spectra of the silver suspension throughout the course of the reaction within the spectral range of 300 to 700 nm. The extinction spectra of the collected aliquots are shown in Figure 5.10. The total reaction time was approximately 4 hours, and each curve corresponds to an aliquot taken in ~20-minute intervals. The extinction curves of all aliquots show a single localized surface plasmon resonance (LSPR) peak, representing the dipole component of the plasmon

resonance of small, spherical silver particles[94]. The absence of any other maxima is indicative that the particles are small, because quadrupole, octupole, and other multipole components of the plasmon resonance are still negligible[110]. A subtle evolution of the extinction maxima to longer wavelengths can be seen, which indicates the gradual increase of particle size. The consistent increase in resonance intensity (higher optical density) also indicates that more nanoparticles are being nucleated and increasing in size. This is because the molar extinction coefficient increases linearly with increasing volume of particles[111]. This corresponds well to the colour evolution seen in Figure 5.9, which shows that the solution became an increasingly darker shade of yellow as the reaction progressed.
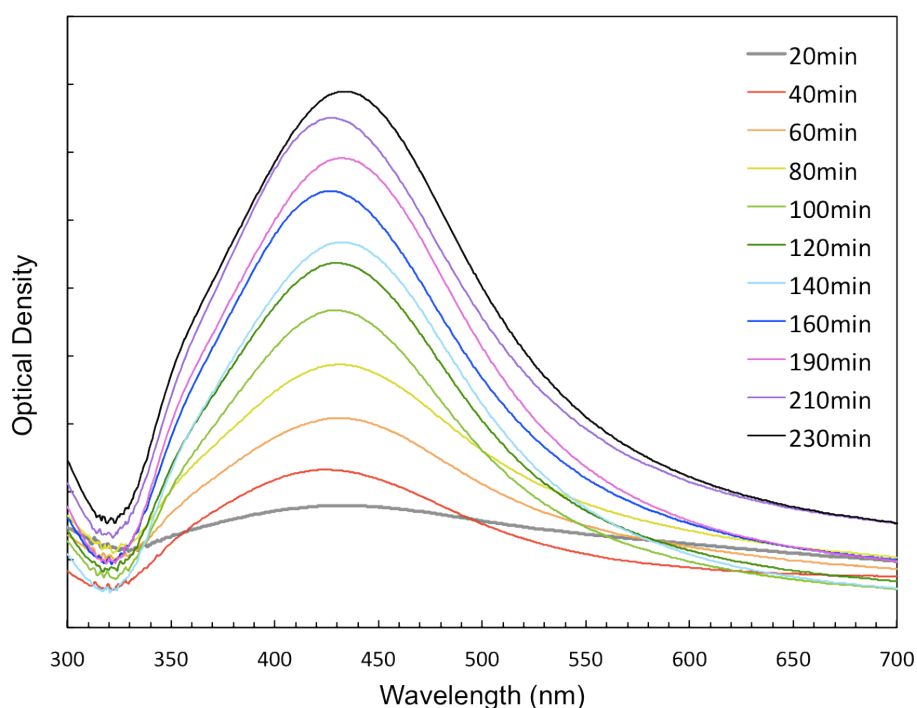
Figure 5.10: Extinction spectra of Ag-NP aliquots sampled throughout the course of a single synthesis reaction. The atmospheric concentration of H_2 was 5%.

A gradual evolution of the extinction maxima, which correspond to the position of the dipole component of the plasmon resonance, is more apparent in Figure 5.11. The extinction maximum starts at an initial peak position around 425 nm at the start of the

synthesis, and as the reaction progresses, its position shifts to longer wavelengths with increasing particle size. This redshift can be explained by Mie's theory, which states that larger particles interact with light to a much greater extent than smaller ones by virtue of a larger number of electrons participating in the plasmon resonance. This leads to an inhomogeneous polarization of the Ag NPs by the electromagnetic field (see section 1.3 for the basics of plasmon resonance)[112,113], which is usually ascribed to retardation effects causing lower (longer resonance) frequencies.
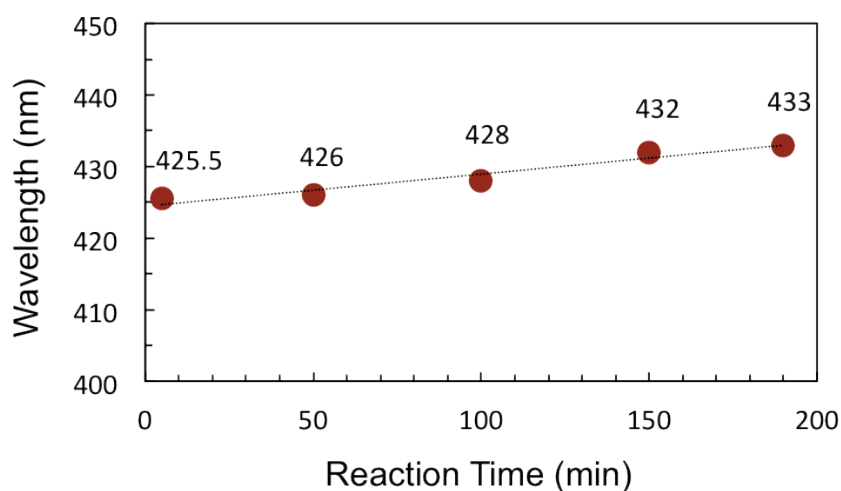
Figure 5.11: Peak extinction wavelengths of Ag nanoparticles throughout the synthesis reaction. These represent the localized surface plasmon resonance wavelengths (λ_{LSPR}) and correspond to increasing Ag particle sizes.

Since light-trapping effects are most pronounced at the peak of the plasmon resonance spectrum, the integration of these plasmonic NPs into the photoactive layer of DSSCs can therefore help absorb longer, less energetic frequencies of light, which are typically inefficiently absorbed by the cell, working towards achieving broader, panchromatic solar absorption.

Because the synthesized Ag NPs are bare, transmission electron microscopy (TEM) was not the most effective way of verifying the particles' true size and shape distributions. That is, the conventional method of drying a suspension of nanoparticles onto a TEM grid cannot accurately represent the particle distributions because as the solvent

evaporates, the capillary forces tend to segregate particles of different size and shape, and silver particles particularly are known to agglomerate if their surfaces are not functionalized[63]. Instead, particle morphology was observed by immobilizing the silver particles onto polymer-functionalized FTO glass electrodes (see experimental section for details). Having empty d-orbitals characteristic of transition metals, Ag NPs bind strongly to P4VP through the lone pair of electrons on the nitrogen of the polymer's pyridine ring. Additionally, since the pyridine ring has the same affinity for silver metal regardless of particle size, shape or aggregation state[94], an accurate representation of the shape and size distribution of the silver can be observed. This is true as long as the substrates are exposed to the Ag suspensions for the amount of time required to establish equilibrium between the surface and the suspension. The P4VP-functinoalized FTO electrodes were therefore soaked in silver suspensions for 12 hours, and the corresponding SEM images of Ag nanoparticles from those 3 different suspensions are shown in Figure 5.12. In agreement with the UV-vis results, analysis of these images by Image J software confirms that the Ag particles did indeed increase in size as the reaction progressed. Ag NPs from a suspension that was extracted after 30 minutes of reaction time are shown in Figure 5.12a, and had an average particle size of 34 nm. After 1 hour of reaction time, particles grew to an average 45 nm in diameter (Figure 5.12b). The NPs in Figure 5.12c correspond to a reaction time of 1.5 hours, and demonstrated a bimodal particle size distribution with average diameters of 33 and 60 nm, likely attributed to Ostwald ripening[114].

Resonance properties are strongly determined by the particle shape and dimensions their colloidal solution[64]. For Ag NPs, localized surface plasmon resonance gives rise to the vivid colour of their colloidal solutions, as seen in the top pictures of Figure 5.12. The suspension of the smallest particles appears yellow and completely transparent, as the absorption contribution of the dipole resonance dominates the extinction spectrum (recall extinction = absorption + scattering). For the larger particle suspensions, increased opalescence can be observed, as the resonant scattering contribution of the dipole resonance becomes a dominating spectral component[94]. Accordingly, the larger particles from the 1 & 1.5-hr reactions may provide an additional benefit to DSSC performance

because light scattering by larger particles increases the optical path of electrons during device operation[115].
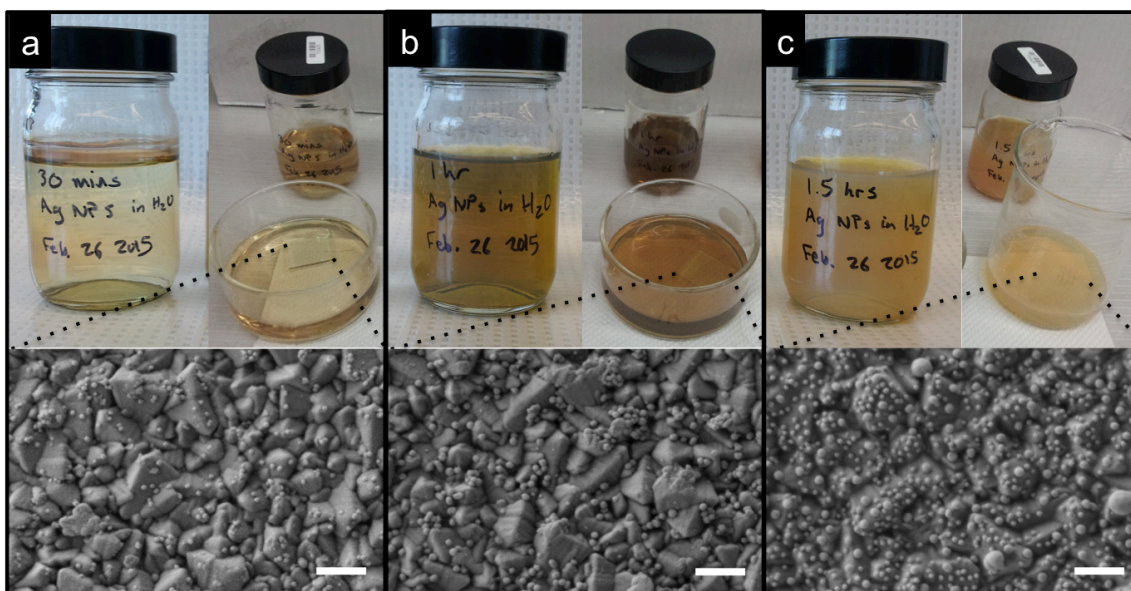
Figure 5.12: Ag suspensions and corresponding SEM images of Ag NPs adsorbed onto FTO glass. Slides were soaked in the Ag suspensions for 12 hours. a) 30-minute reaction with pure H_2; b) 1-hour reaction with pure H_2; c) 1.5-hour reaction with pure H_2. The scale bars are 300 nm.

The particles seemed to be the most uniformly dispersed along the electrode surface after the longest reaction time. For a 12-hour soak, Ag NPs seemed to collect in the kinks and valleys of the FTO surface for the 30-minute and 1-hour reaction times, suggesting that the substrates may not have been sufficiently exposed to the Ag suspensions to establish an equilibrium with the surface. The soaking time was therefore increased to 16 hours, and the additional 4 hours resulted in a more evenly distributed array of Ag NPs, as can be seen in Figure 5.13. These SEM images were taken in backscattering mode to show the contrast between the polymer-coated FTO and the Ag NPs.
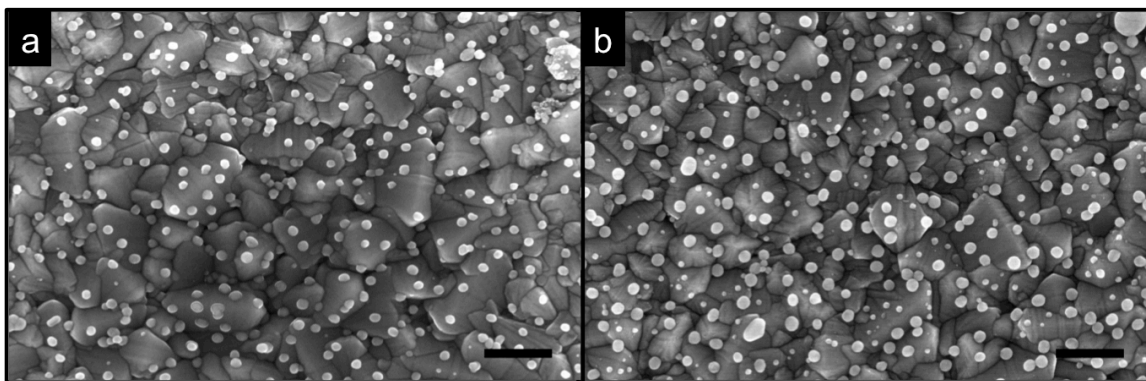
Figure 5.13: SEM images of P4VP-functionalized FTO electrodes soaked in Ag solutions for 16 hours. In backscattering mode, heavier metals appear brighter. a) 1-hour reaction with pure H_2; b) 1.5-hour reaction with pure H_2. Scale bars are 300 nm.

Atomic layer deposition was used as the methodology to protect the Ag-functionalized electrodes with TiO_2. The titania barrier prevents direct contact between the Ag NPs and the electrolyte, slowing the back reaction of electrons to the redox couple medium (electrolyte) during cell operation. To form a fully protective barrier (i.e. no pinholes), 300 cycles (~7.7 nm) of TiO_2 precursor must be deposited, unless 2 cycles (~0.2 nm) of an aluminum oxide (Al_2O_3) adhesion layer are first deposited, in which case only 211 cycles (~5.6 nm) of TiO_2 precursor are necessary[95]. The benefit of having a thinner ALD coating is to have a more pronounced plasmon effect; the enhanced field is highly localized at the NP surface (Figure 5.14), which decays rapidly with increasing distance from the surface[42]. These two ALD precursor formulations were compared to determine which formulation showed superior performance in DSSCs.
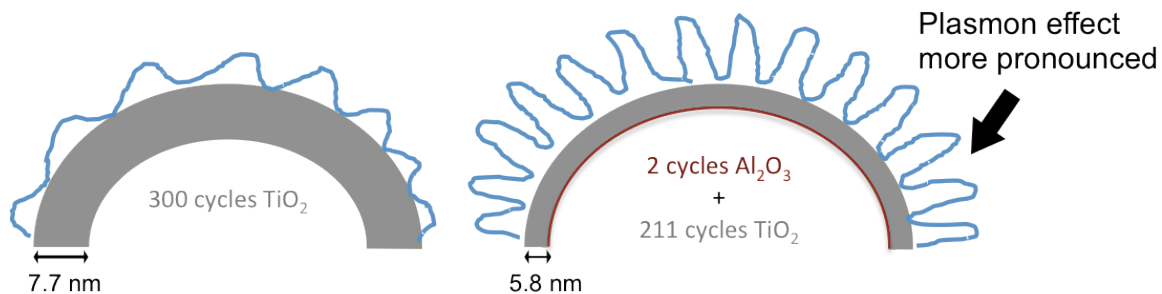
Figure 5.14: The two ALD precursor formulations tested in DSSCs. A thinner shell contributes to a more pronounced plasmon effect.

The layers comprising a 'blanket-array' electrode as well as corresponding SEM images taken throughout the electrode's fabrication process are shown in Figure 5.15.
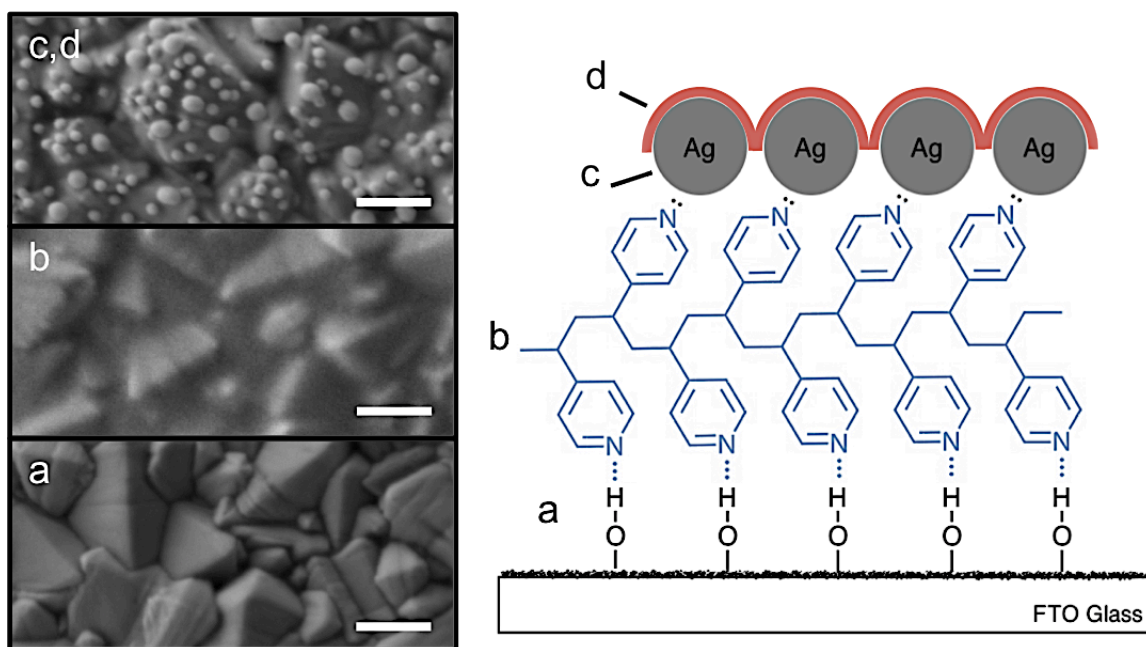
Figure 5.15: Composition of a 'blanket-array' electrode and corresponding SEM image taken throughout the fabrication process. a) Piranha-treated FTO glass; b) P4VP-functionalization; c) Ag NPs bonded to the pyridine ring of the polymer; d) Thin TiO_2 layer deposited via ALD. ALD-coated Ag NPs are indiscernible from uncoated Ag NPs by SEM. Scale bars are 200 nm.

Instead of EDS, XPS was used to confirm the elemental composition of each layer of the electrode, as this latter technique is better suited to target the top ~10 nm of a samples' surface. XPS survey scans confirmed the presence of Ag and titanium in the top two layers of the electrode. The spectra of the Ag-array coated surface of the electrode revealed that tin, oxygen, carbon, and small amounts of nitrogen were present in the sample. An Ag 3d peak appeared after soaking the P4VP-functionalized slides in silver suspensions. The major XPS peaks for the TiO_2-coated surface include Ag 3d, Ti 2p and O 1s. Because 300 cycles of ALD-coated TiO2 is only ~7.7 nm thick, the spectrometer can still detect an Ag 3d signal, although it was weaker than in the absence of the TiO_2 layer.

5.3.2.1   Performance of 'Blanket-Array' architecture DSSCs

'Blanket-Array' DSSCs were fabricated using the two different ALD precursor formulations to coat the photoelectrodes, under the same parameters as the 'chocolate-chip' DSSCs. The photoactive layers for both cells were calcined at 400 ºC. Ag NPs adsorbed onto the electrodes were synthesized in pure H_2 for 1.5 hours. The performance of the two formulations are compared in Figure 5.16a, which clearly shows that a higher cell efficiency is achieved in the absence of an Al_2O_3 adhesion layer. The source of the two formulations' variation in performance can be seen in their J-V characteristic curves (Figure 5.16b). Both cells exhibited similar open circuit voltages (0.69 V with an Al_2O_3 adhesion layer vs. 0.68 V without), but the cell with 300 TiO_2 cycles achieved a higher short circuit current density (11.76 mA/cm^2 with adhesion layer vs. 13.49 mA/cm^2 without). With the fill factors of both cells at 0.64, the improvement clearly stems from a greater amount of electrons being extracted in the DSSC having 300 cycles of TiO_2 coating the photoelectrode. The energy band diagram in Figure 5.16c shows that the conduction band edge (E_{CB}) of Al_2O_3 is higher than that of TiO_2, which blocks electron injection into the current collector. Therefore, the 300 TiO_2 cycle coating formulation demonstrated superior performance, and was used to test the effectiveness of zirconia thermostabilization in DSSCs.
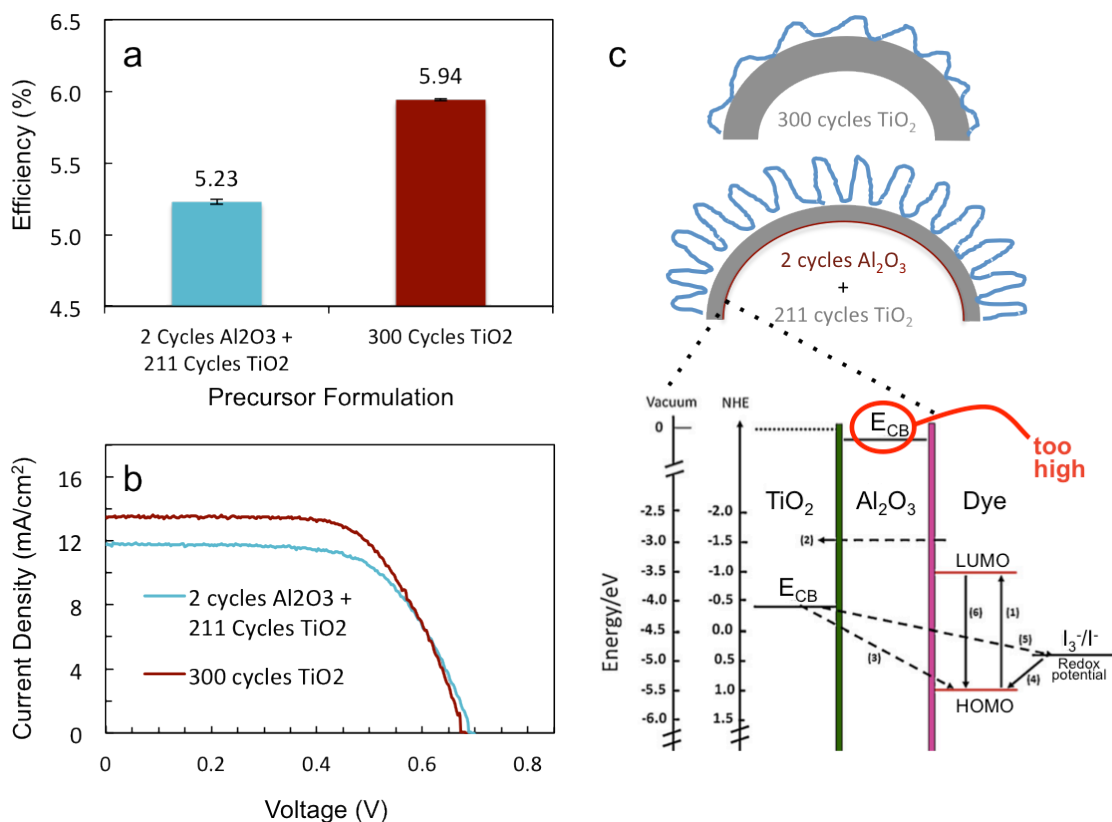
Figure 5.16: Performance of 'blanket-array' DSSCs comprising two different ALD precursor formulations (a) and their corresponding current density-voltage curves (b). The Al_2O_3 adhesion layer acts as barrier for electron injection (c) because of its high conduction band edge. The photoactive layers for both cells were calcined at 400 ºC. Ag NPs adsorbed onto the electrodes were synthesized in pure H_2 for 1.5 hours.

Figure 5.17 compares the efficiencies achieved by DSSCs with and without a plasmonic 'blanket-array' photoanode, and how the incorporation of zirconia into their photoactive layers affected their performance. The plasmonic NP array was composed of Ag NPs synthesized in pure H_2 for 1.5 hours, and the protective shell was composed of 300 cycles of TiO_2 precursor. The Zr-doped cells contained 5% Zr, as this was determined to be the optimal zirconia concentration in the previous chapter. The photoactive material of all cells was calcined at 500 ºC. The 'blanket-array' DSSCs showed a significant improvement in efficiency over the plasmon-free DSSCs. An increase in the PCE is a direct correlation to the increased photocurrent, as can be seen in the inset table of Figure

5.17, corresponding to enhanced light absorption by the dye. The deposition of a TiO_2-protected Ag-NP array onto the photoanode increased scattering within the active cell layer compared to the plasmon-free DSSCs, which increased the optical path, and thus increased the amount of dye molecules reached by light. The addition of 5% zirconia however only slightly improved the cell efficiency. The reason for such a small improvement is stipulated to be because the Ag NPs were not distributed throughout the photoactive layer, and so did not create any appreciable thermal deterioration in the titania matrix. Zirconia therefore did not play a significant role in the efficiency improvement of 'blanket-array' architecture plasmon-enhanced DSSCs.

Sample	V_{OC} (V)	J_{SC} (mA/cm^2)	FF	η (%)
Control	0.69	8.01	0.63	3.50
5% Zr	0.67	9.34	0.60	3.75
Ag@TiO2	0.70	11.13	0.67	5.25
Zr+Ag@TiO2	0.71	11.37	0.65	5.27
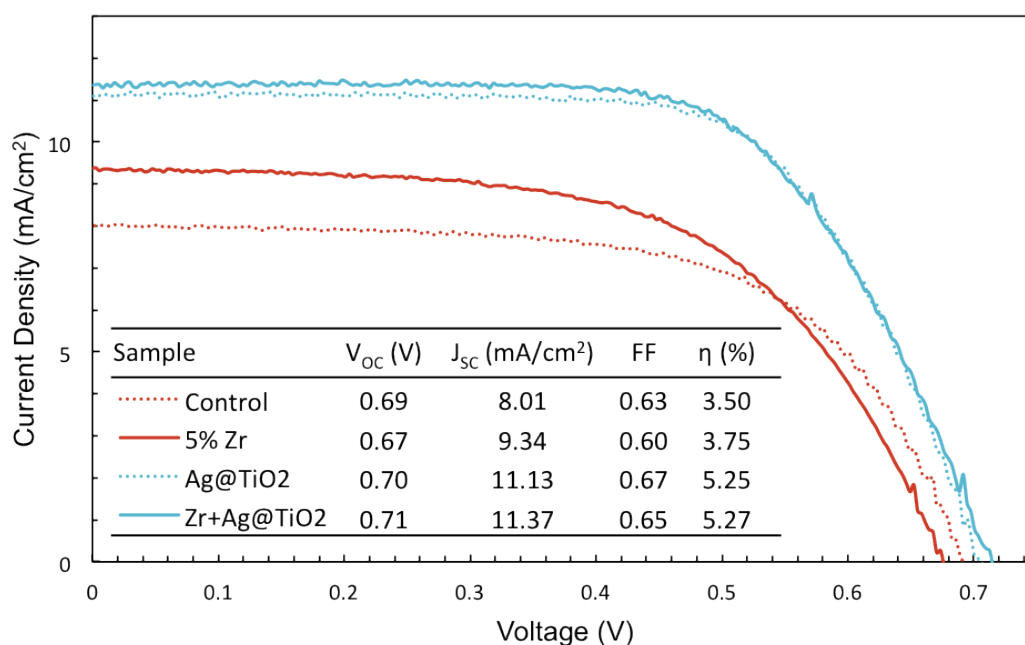
Figure 5.17: The effect of Zr and plasmon doping on the J-V curves of 'blanket-array' architecture DSSCs. The inset shows the characteristic values corresponding to the curves.

Better fill factor values were observed in the 'blanket-array' design cells compared to the 'chocolate-chip' cells (Figure 5.8), which is an indication of better overall electron transport within the cell. This correlates with the fact that the exposed Ag in the 'chocolate-chip' architecture acted as recombination centers for electrons, preventing them from reaching the exterior circuit.

5.3.3 Comparison of Both Plasmon-DSSC Architectures

The performance of the two proposed photoactive cell layer designs, notably the 'chocolate-chip' and the 'blanket-array' architectures, were compared to determine the best cell design for incorporating Ag@TiO$_2$ NPs into DSSCs. Table 5.1 shows that in all three cases – in the absence of plasmon NPs and in the two plasmonic cell architectures – doping with zirconia provided thermostabilization during cell operation and increased the efficiency.

Table 5.1: Comparison of the effect of Zr doping on the performance of different plasmon-enhanced DSSC architectures.

Cell Types*	Control	Zr-doped	Plasmon DSSCs		Zr-doped Plasmon DSSCs	
TiO2	100%	95%	100%	100%	95%	95%
ZrO2	-	5%	-	-	5%	5%
Plasmonic Component**	-	-	Ag@TiO$_2$ NPs	Ag@TiO$_2$ photoanode	Ag@TiO$_2$ NPs	Ag@TiO$_2$ photoanode
PCE (%)	3.50	3.75	4.38	5.25	6.32	5.27

* All photoactive material was calcined at 500 °C; ** Ag@TiO$_2$ NPs had 20 mM TIP shell precursor; Ag NPs were synthesized in pure H$_2$ for 1.5 hours; ALD coating was 300 cycles of TiO$_2$ precursor.

In the absence of a plasmonic component, the inclusion of 5% zirconia in the TiO$_2$ photoactive layer improved the PCE from 3.50% to 3.75%, which was previously found to be a result of the zirconia maintaining the crystal structure, and increasing the surface area. Between the two plasmonic cell architectures, the 'blanket-array' design achieved a better efficiency in the absence of Zr-doping (5.25%). The comparison for best cell design however cannot be made accurately due to the 'chocolate-chip' architecture suffering from increased electron recombination as a result of its Ag NPs not having a protective TiO$_2$ shell. Despite this defect, the performance of the 'chocolate-chip' cell surpassed that of the 'blanket-array' cell when zirconia was included in the photoactive layer. The PCEs of 4.38 and 6.32% achieved by the 'chocolate-chip' cells would likely have been even higher if the Ag@TiO$_2$ NP synthesis had been successful. Nonetheless, a

clear improvement in efficiency is seen with the inclusion of Zr, which helped the TiO_2 matrix preserve its structure and maintain its surface area in the presence of heat-creating Ag plasmons, evidence that zirconia induced thermal stability. Although the inclusion of Zr in the 'blanket-array' cell design increased the PCE, the improvement was marginal (5.25 to 5.27%). In this particular architecture, plasmonic NPs were not dispersed throughout the TiO_2 matrix, but were rather only in close proximity with TiO_2 particles at the interface of the plasmonic electrode and the photoactive layer. Therefore, zirconia provided limited thermostabilizing benefit in this architecture. It is only when the plasmonic particles are dispersed throughout the photoactive TiO_2 matrix, as in the 'chocolate-chip' architecture, that their thermal loss poses a threat to the collapse of the matrix, reducing the surface area and thus the photoabsorptive capabilities of the cell.

Zirconia exhibits thermostabilizing properties in both plasmonic cell architectures, but to a greater extent in the 'chocolate-chip' architecture, where the plasmonic nanoparticles are dispersed throughout the photoactive layer. The downfall of the 'blanket-array' design is that the enhanced local field by LSP resonance only enhanced charge separation for the limited number of dye molecules close to the $Ag@TiO_2$ array-photoactive material interface, leading to limited photocurrent enhancement. The enhanced photocurrent observed in the 'blanket-array' cells can thus be mainly attributed to plasmonic scattering, where the array of silver nanoparticles acted as nano-mirrors, trapping light within the active layer and give dye molecules multiple passes at absorbing photons. Therefore, the 'chocolate-chip' architecture is the superior cell design for incorporating $Ag@TiO_2$ NPs into Zr-doped DSSCs.

5.4 Conclusions

The use of zirconia (ZrO_2) as a thermostabilizer in DSSCs was investigated to counteract the thermal loss caused by plasmonic silver nanoparticles. In both cell architectures, $Ag@TiO_2$ NPs were used as absorption antennas or nano-mirrors within the DSSC to efficiently convert free-propagating optical radiation into localized energy or increase its optical path length, respectively.

HRTEM and EELS analysis revealed that the $Ag@TiO_2$ NPs synthesized for the 'chocolate-chip' architecture did not have a TiO_2 shell physically isolating the Ag cores from the electrolyte. Nonetheless, it was demonstrated that incorporating zirconia into the photoactive layer permitted the plasmon-doping threshold to be increased to 5% before submitting to a decrease in efficiency, which is an improvement on the 0.6% doping limit reported in literature.

SEM and XPS analysis confirmed the successful fabrication of 'blanket-array' electrodes. Silver nanoparticles reduced in water with pure H_2 for 1.5 hours provided an additional benefit to DSSC performance because light scattering by the larger particles increased the optical path of electrons during device operation. Of the two ALD coating formulations investigated, the one containing 300 cycles of TiO_2 precursor demonstrated superior photocurrent in DSSCs, and was used to test the effectiveness of zirconia thermostabilization in DSSCs.

Zirconia exhibited thermostabilizing properties in both plasmonic cell architectures. The 'chocolate-chip' architecture, having plasmonic Ag NPs dispersed throughout the active layer, demonstrated superior performance over the 'blanket-array' architecture in the presence of ZrO_2, despite the unsuccessful coating of TiO_2 on the silver NPs' surface. Both the photocurrent and fill factor were significantly enhanced, and a PCE of 6.32% was observed in the presence of zirconia, compared to a value of 4.38% without zirconia doping. Their performance would likely have been higher had the Ag NPs been properly protected, as their chemical corrosion likely contributed to their dampened efficiencies. Although the 'blanket-array' architecture resulted in better photovoltaic performance in

the absence of ZrO_2, the addition of 5% zirconia only marginally improved the cell efficiency from 5.25 to 5.27%. The reason for such a small improvement is stipulated to be because the Ag NPs were not distributed throughout the photoactive layer, and so did not create any appreciable thermal deterioration in the titania matrix. Consequently, ZrO_2 did not play a significant role in the efficiency improvement of 'blanket-array' DSSCs, as its thermostabilizing benefits were limited in this architecture.

It can therefore be concluded that the 'chocolate-chip' architecture is the superior cell design for incorporating $Ag@TiO_2$ NPs into Zr-doped DSSCs. Zirconia's thermostabilizing effect in plasmon-enhanced DSSCs can also lead to new solar cell designs with smaller semiconductor thicknesses, and thus lower material costs.

Chapter 6

6 The performance of TiO$_2$ nanoparticles synthesized in supercritical CO$_2$ as photoactive material in DSSCs

6.1 Introduction

Demand for high quality advanced materials such as nanoparticles, semiconductors and nanocomposites is growing enormously owing to the required high performance in applications as varied as telecommunications, air purification, smart surfaces, and photovoltaic cells. In particular, metal oxide nanoparticles such as titanium dioxide have tremendous functionality in dye-sensitized solar cells (DSSCs). Current preparation techniques for making metal nanoparticles use the sol-gel procedure. In this well-known technique, metal alkoxides undergo hydrolysis and condensation reactions in solution to form amorphous metal oxides, which become crystalline upon calcination. Although this technique is deemed reliable in forming nanoparticles of controllable size and morphology, it typically uses toxic and environmentally unfriendly solvents to control and optimize reaction conditions. Removal of these solvents results in uncontrollable reaction rates, and undesirable material characteristics.

Recent work has shown that TiO$_2$ nanoparticles can be synthesized via the sol-gel route in supercritical fluids with remarkable control by modifying the supercritical conditions and operational variables of the reaction. For instance, scCO$_2$ has been successfully used to develop new nanostructured materials, in particular well-controlled 1D high aspect ratio TiO$_2$ and Zr-doped TiO$_2$ nanostructures by the sol-gel method[83]. However, scCO$_2$ as a sole solvent demonstrated low solubilising capabilities, which required relatively high pressures using expensive equipment, which has limited its attractiveness for scale-up. To circumvent these drawbacks, a strategy used by some researchers has been to use scCO$_2$ in combination with co-solvents that exhibit gas-expandable properties[48,116,117]. A gas-expanded liquid (GXL) is a mixture of a condensable gas with a liquid phase, and where this liquid phase presents properties that are substantially different from those at

atmospheric pressure. An expansion of the liquid is frequently observed as concentration of the solubilised CO_2 increases, which changes both the solvent characteristics and physical properties of the liquid, reducing both the polarity and the hydrogen-bonding abilities of the expanded liquid[118]. Other properties that can be modified by CO_2 are the viscosity, dielectric constant and density, meaning that the solvent properties of the reaction mixture can be tuned with pressure[47]. Control of these properties is interesting from both a scientific and an engineering point of view, as it would allow the use of one solvent to perform several steps in a process that otherwise would require multiple solvents.

This study aimed at developing superior quality TiO_2 nanoparticles using supercritical CO_2 for applications in DSSCs. More specifically, TiO_2 was synthesized using a modified sol-gel technique in $scCO_2$ to investigate the purity, crystallinity and surface area of the material, and see how it compared to TiO_2 synthesized via the traditional sol-gel route. The possibility to modulate solvent properties by $scCO_2$ has yet to be extensively exploited to obtain materials for applications in DSSCs. This study also introduced the synthesis of TiO_2 NPs based on the coupling of green bio-sourced solvents (GBSs) with supercritical CO_2. Until now, GXLs have been used in some chemical reactions, but are conventionally volatile and toxic. In this present work, GBSs were used as co-solvents with $scCO_2$ to prepare TiO_2 nanoparticles, with the hopes of encouraging the development of cleaner processes for nanomaterials used in DSSCs and similar advanced functional devices. The GBSs used were glycerol, ethyl lactate and ethyl acetate. To the best of our knowledge, no research group has proposed the use of these GBSs as GXLs for the preparation of TiO_2 NPs.

6.2 Experimental

TiO_2 NPs were synthesized in a high-pressure, variable-volume view cell reactor. The high-pressure reactor contained a CO_2 inlet as well as temperature and pressure controllers. A syringe pump was used to deliver the pressurized CO_2 into the view cell using a 2-way valve injection loop. A total of 8 products were synthesized, and their list of reagents and operational conditions can be found in Table 6.1. The reaction volumes were limited to 35 mL to accommodate the maximum internal volume capacity of the reactor.

The first three samples (Table 6.1a) were produced with the same precursors used in the conventional sol-gel synthesis described in Chapter 4.2. Sample T1 was synthesized via the conventionally hydrolytic sol-gel (HSG) route where water serves as both a ligand and a solvent[87]. The non-hydrolytic sol-gel (NHSG) route is an alternative pathway for the preparation of metal oxides under the exclusion of water, where the oxygen for the metal oxide formation is provided by the solvent or by the organic constituent of the precursor[87] instead of water. The NHSG process is relatively slower than the HSG approach, but this lower reactivity makes the morphologies and microstructures of NHSG-derived metal oxides more controllable, which was the reasoning for trying the supercritical reaction of T2 and T3 in the absence of water.

In Table 6.1b, glycerol, ethyl lactate and ethyl acetate were solvents used in conjunction with $scCO_2$ to synthesize TiO_2 nanoparticles (T4–T8). These non-toxic, bio-sourced solvents were used to put emphasis on developing an overall clean process, using a 'green' technique to create nanomaterials that serve a purpose in 'green' technology. Two different Ti precursors were used with each ester, titanium butoxide (TBO) and titanium diisopropoxide bis(acetylacetonate) (DIPBAT), to see how their variation in reactivity would affect the product's characteristics. DIPBAT is a less reactive precursor than TBO because its bonds are more stable[44].

Table 6.1: Reagents and operational conditions used for different supercritical CO_2 reactions attempted; a) Reactions that used conventional solvents; b) reactions that used green bio-sourced solvents.

a	Reagents (mL)					CO_2 Conditions			Rxn Conditions	
	TBO	acac	EtOH	HCl	H_2O	mL	°C	bar	°C	Time
T1					2.1	13	2.0			
T2	8.5	3	5.7(x2)	0.142	--	14	1.6	90	50	5 hrs
T3					--	14	1.3			3 hrs

b	Reagents (mL)					CO_2 Conditions			Rxn Conditions	
	TBO	DIPBAT	Glycerol	Ethyl Lactate	Ethyl Acetate	mL	°C	bar	°C	Time
T4	5	--	5	--	--	17	1.4			
T5	1.8	--	--	18.2	--		0.2			
T6	--	1.9	--	18.1	--	13	0.4	150	80	3 hrs
T7	2.1	--	--	--	17.9		0.4			
T8	--	2.2	--	--	17.8		0.2			

During the hydrolytic and non-hydrolytic reactions (T1-T3), a solution of TBO and acetylacetone in ethanol was mixed directly into the view cell and heated to the desired temperature of 50 °C under constant stirring. Meanwhile, a solution of ethanol, hydrochloric acid and water was stirred separately, then added drop-wise to the reactor once the temperature had reached 50 °C. For the non-hydrolytic reactions (T2, T3), the volume of water was replaced by CO_2. After sealing the reactor, $scCO_2$ was added at the desired pressure, and the reaction was left to proceed for the allotted time under vigorous stirring. The reactions ran between 3-5 hours and at a pressure of 90 bar.

In the bio-based solvent reactions (T4-T8), the reactants were added into the view cell all at once. The mixture was heated to 80 °C, after which $scCO_2$ was pumped into the cell until the desired pressure was reached. Reactant volumes totalled approximately 20 mL and the remaining volume of the reactor was left for $scCO_2$. The reactions ran for 3 hours under constant stirring at a pressure of 150 bar.

For all samples, the solvent was evaporated by rotovap and in an oven overnight at 60ºC. The as-prepared TiO_2 nanopowders (Figure 6.1a,b) were amorphous, but readily converted to anatase by the same heat treatment subjected to the conventionally synthesized control TiO_2 NPs (4 hours at 400 °C). Crystalline oxides were obtained after calcination (Figure 6.1c,d).
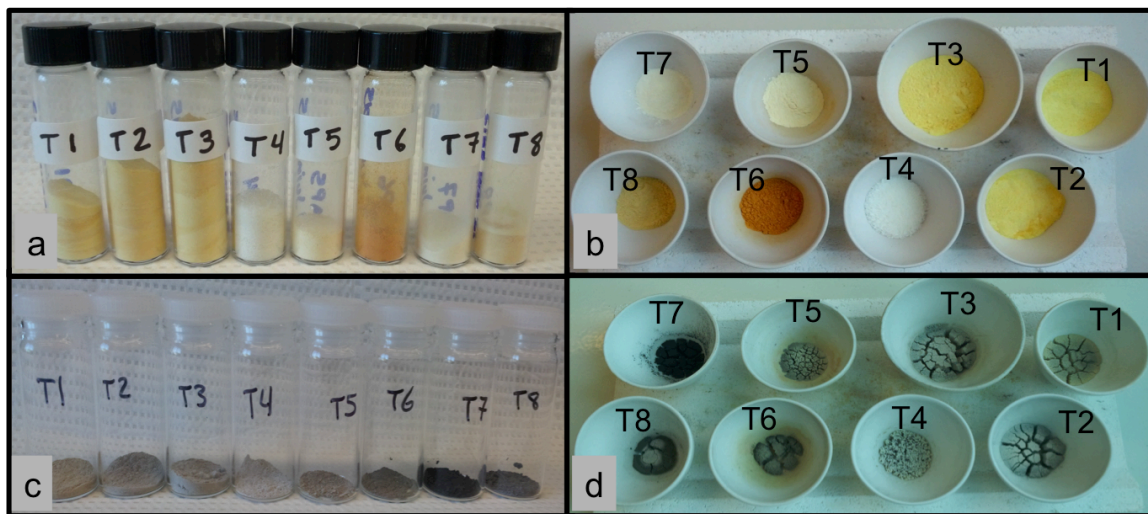
Figure 6.1: TiO_2 Samples prepared in supercritical CO_2 before (a,b) and after (c,d) calcination at 400 ºC for 4 hours.

The crystal structure of the TiO_2 powders was confirmed by X-ray powder diffraction (XRD) using a Bruker AXS D2 Phaser diffractometer with Cu Kα radiation and JCPDS 00-021-1272 for TiO_2 anatase crystal structure identification. The morphology and average particle size of the samples were characterized by scanning electron microscopy (SEM) using a LEO-Zeiss 1540 XB microscope. The specific surface area of the powders was determined by applying the Brunauer-Emmett-Teller (BET) theory to N_2 adsorption-desorption isotherms obtained from a Micromeritics TriStar II 3020 surface area and porosity instrument. The pore size distributions were also calculated using the Barret-Joyner-Halenda (BJH) theory. Finally, DSSCs comprising the synthesized powders as the photoactive material of the cells were fabricated according to the procedure in section 3.3.1. The power conversion efficiency of DSSCs was measured using the simulated

illumination of a Newport Oriel 92250A-1000 solar simulator and a Keithley 2420 digital source meter.

6.3   Results and Discussion

Chemical reaction mechanisms are difficult to predict, but once reactants are in the same phase (the supercritical phase), reactions occur very quickly because mass transfer limitations are eliminated. All reactions were monophased, except for sample T4 (TBO + glycerol) where two phases could be detected through the sapphire windows of the reactor. The proposed mechanism for TiO_2 formation in sample T4 is the hydrolysis of TBO according to the reaction:

$$Ti(OC_4H_9)_4 + 2H_2O \rightarrow TiO_2 + 4C_4H_9OH \qquad (eq.\ 6.1)$$

The water in equation 6.1 is formed from the decomposition of the alcohol in the presence of CO_2. Glycerol is a polar compound and therefore increases the TBO precursor solubility, also acting as a co-solvent. Pressure and temperature also sped up chemical reactions and therefore, precursor decomposition. Therefore, despite the T4 mixture not being completely miscible, titania formation still occurred, which is confirmed by the sample's anatase crystallinity revealed by its XRD spectrum below.

In a DSSC photoanode, the interconnected TiO_2 particles that constitute the semiconducting film need to be crystalline in order to ensure proper charge transport throughout the cell. Therefore, the degree of crystallinity is related to superior electronic and optical properties of TiO_2. XRD spectra of the 8 scCO$_2$-synthesized samples are shown in Figure 6.2. Upon thermal treatment at 400 ºC for 4 hours, all samples showed diffraction patterns characteristic of anatase TiO_2 corresponding to JCPDS 00-021-1272. The samples using conventional solvents (T1-T3), and the samples using glycerol (T4) and ethyl lactate (T5, T6) bio-based solvents demonstrated higher intensities in anatase signal relative to the control, suggesting that samples synthesized in the presence of scCO$_2$ yielded superior crystallinity. Samples synthesized in ethyl acetate (T7, T8)

showed a poorer degree of crystallinity, suggesting incomplete reactions and unreacted precursors.
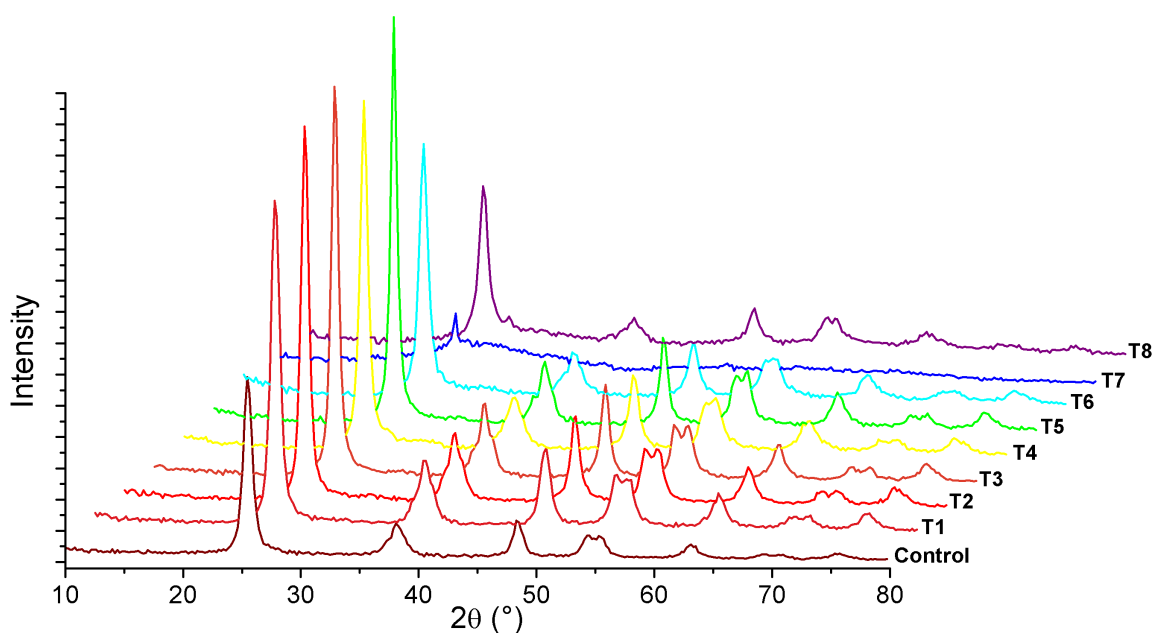
Figure 6.2: XRD spectra of TiO_2 synthesized in supercritical CO_2.

A selection of N_2 adsorption-desorption isotherms of TiO_2 samples calcined at 400 ºC is shown in Figure 6.3, and the corresponding structural characteristics in Table 6.2. All isotherms clearly indicate the porous nature of the samples, as their curve shape and the presence of a hysteresis loop are characteristic of Type IV isotherms[105]. The location of the hysteresis loops for all samples excluding T4 lie between 0.4 and 0.8 relative pressure (P/Pº), which is an indication of mesoporous capillary condensation[106]. This is confirmed by the experimental BET results listed in Table 6.2, where the average pore diameters fall within the range of 3.3 and 10.3 nm. The shift in capillary condensation towards higher pressures in sample T4 suggests an increase in pore width because a larger volume takes more pressure to condensate. Indeed, sample T4 presented the largest average pore size.
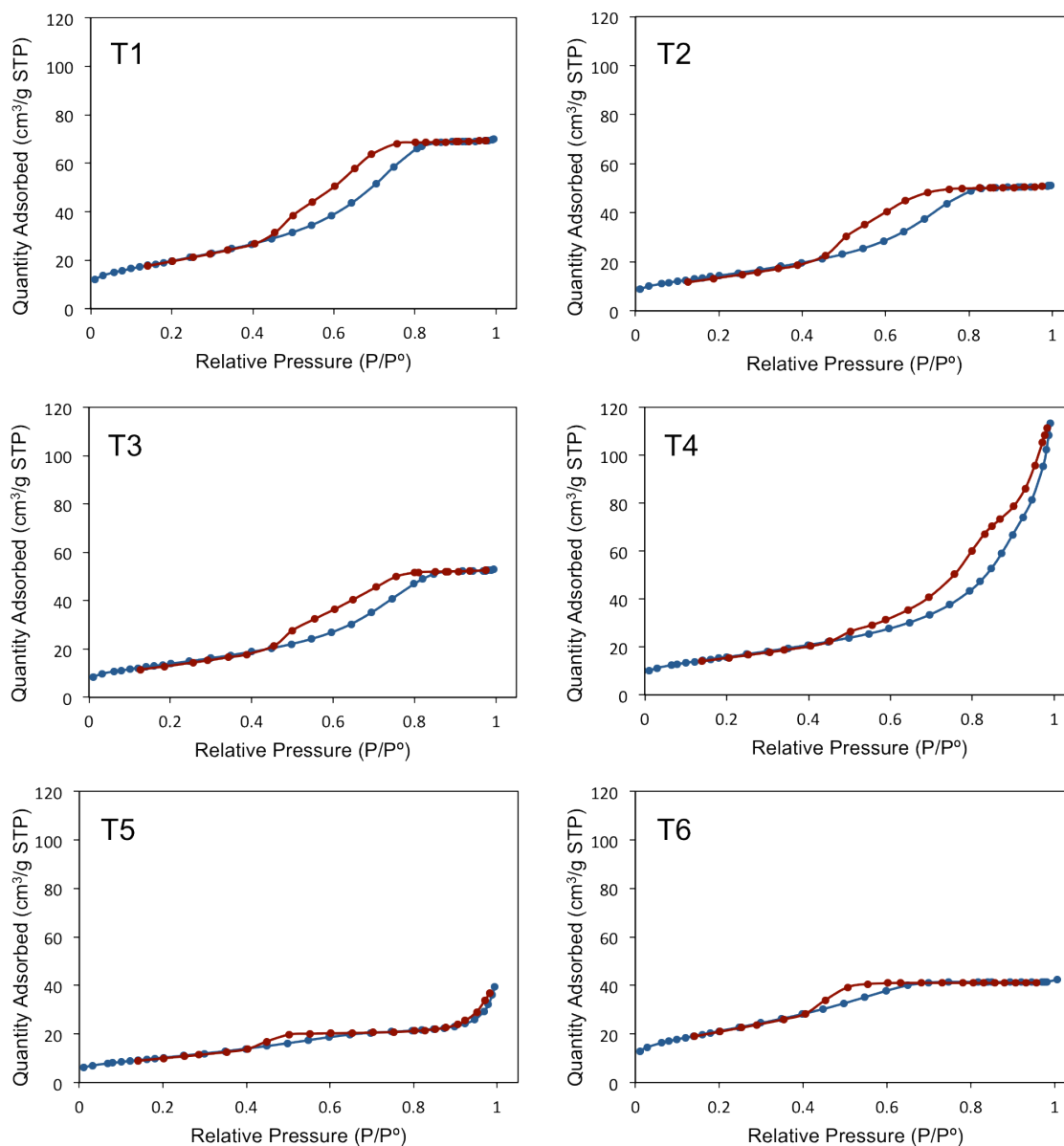
Figure 6.3: N$_2$ adsorption (blue curves) and desorption (red curves) isotherms of select TiO$_2$ samples calcined at 400 ºC. Isotherms for samples T7 and T8 are not shown.

The specific surface area (SSA) of the TiO$_2$ nanopowders calculated using the BET method were all lower than the control value of 87.9 m^2/g. Samples synthesized with conventional solvents in scCO$_2$ (T1-T3) all showed similar BET results because they all had similarly-sized hysteresis loops. The hydrolytic sample (T1) had the higher SSA. The non-hydrolytic samples (T2 and T3) varied only by a 2-hr difference in reaction time, and

therefore their textural characteristics were very similar. As expected, the average particle size was slightly smaller for T2 (115 nm) because it had a shorter reaction time of 3 hours rather than 5 hours. Samples T5 and T6, synthesized in ethyl lactate under $scCO_2$ both had smaller hysteresis loops, indicating a smaller mesopore volume, which is in accordance with their calculated average pore sizes.

Table 6.2: BET experimental results and pore structure parameters of TiO_2 samples synthesized in supercritical CO_2 and calcinated at 400ºC for 4 hrs.

Sample	Surface area (m²/g)	Average particle size (nm)	Average pore size (nm)
Ctrl	87.9	68.3	6.1
T1	71.3	84.2	6.0
T2	52.1	115.1	6.0
T3	50.4	119.0	6.4
T4	57.0	105.3	10.3
T5	32.0	187.3	5.3
T6	76.9	78.0	3.3
T7	7.0	857.6	1.8
T8	30.4	197.1	8.0

The experimental results show that the SSA of TiO_2 is related to its crystallinity. Samples that demonstrated higher crystallinity (T2-T5 in Figure 6.2) revealed a lower SSA. Generally, lower surface area was a result of bigger particle size.

SEM was used to confirm the morphology of the TiO_2 samples formed under supercritical conditions, and to compare these observations with the physical properties obtained by BET. SEM micrographs of the TiO_2 samples can be seen in Figure 6.4. Before SEM analysis, samples were sputtered with 2-3 nm of Osmium using a coating machine to prevent surface charging. The morphology of the formed TiO_2 nanoparticles was consistently spherical, although some particles appeared larger than others, and some samples experienced more particle fusion. All images are set to the same magnification (75K), so a clear distinction of size variation can be seen. The morphologies of the non-hydrolytic T2 and T3 samples are similar, as expected, since the only difference between them is a reaction time difference of 2 hrs. T4 appears to be composed of the largest nanoparticles, while T6 and T7's particles are so small that they cannot be resolved at this

magnification. The particle sizes obtained from the BET analysis do not agree completely with these observations. In some cases, a larger BET particle size may be misleading, as a group of fused particles may be counted as one larger molecule.
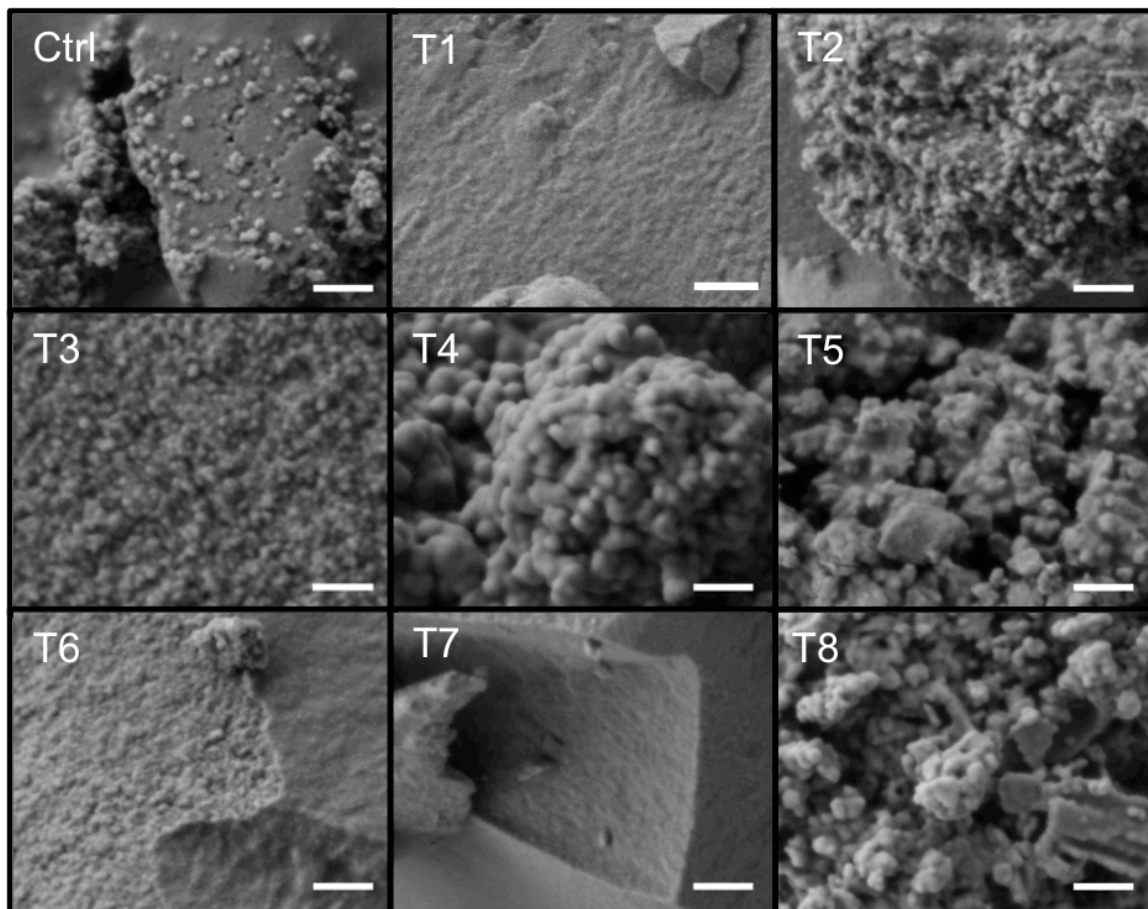
Figure 6.4: SEM images of TiO$_2$ samples synthesized in supercritical conditions. All image are magnified 75K times. The scale bars are 200 nm.

The main difference in morphology observed between the two precursors synthesized in ethyl lactate (T5, T6) is in the particle size. Particles with an average diameter of ~187 nm were obtained from TBO decomposition at 150 bar and 80 °C. Under the same operational conditions, TiO$_2$ particles were smaller (~78 nm) when DIPBAT was used as the precursor, as shown in Figure 6.4. The larger particle sizes of the TBO-based reaction can be explained by the materialization of Ti(OH)$_4$ nuclei during the reactor heating step.

These titanium hydroxide centers provide a head start for particle growth because they act as seeds for material agglomeration.

6.3.1 Performance of DSSCs using TiO_2 synthesized in $scCO_2$

Dye-sensitized solar cells (DSSCs) were fabricated using the TiO_2 samples synthesized under supercritical conditions as the photoactive material. Cells were fabricated according to the procedure in section 3.3.1. The cells were tested under 1-sun simulated sunlight, and their characteristic photocurrent density-voltage (J-V) curves are shown in Figure 6.5. The photovoltaic characteristics derived from the JV curves, including the open-circuit voltage (V_{OC}), short-circuit current density (J_{SC}), fill factor (FF) and energy conversion efficiency (η) are listed in Table 6.3.

The J-V curves of the hydrolytic and non-hydrolytic TiO_2 samples synthesized in $scCO_2$ are shown in Figure 6.5a. Despite having lower specific surface areas compared to the control, the supercritical samples using conventional solvents still performed well as photoactive layers, and in some cases better, compared to the DSSCs containing the control TiO_2 layer. Sample T3, the non-hydrolytic TiO_2 reacted for 3 hours, obtained the highest efficiency (6.7%), which was superior to the control's performance. In fact, both non-hydrolytic samples (T2, T3) gave superior performance to the hydrolytic-synthesized sample (T1), suggesting that sol-gel reactions performed in supercritical CO_2 should avoid the use of water to prevent excessive, uncontrolled growth of particles. This is because the hydrolysis of TiO_2 precursors in the presence of water already occurs very readily, and facilitating this reaction even further by eliminating mass transfer limitations (i.e. performing the synthesis under supercritical conditions where the reactants are in one phase) would not allow for uniform and controlled particle growth. If particles become too large, the crystallinity and surface area of particles are negatively affect, which in turn compromises the photovoltaic efficiency. This is confirmed by the XRD results in Figure 6.2, which show that the non-hydrolytic samples (T2, T3) have stronger anatase TiO_2 peaks than the hydrolytic T1 sample.
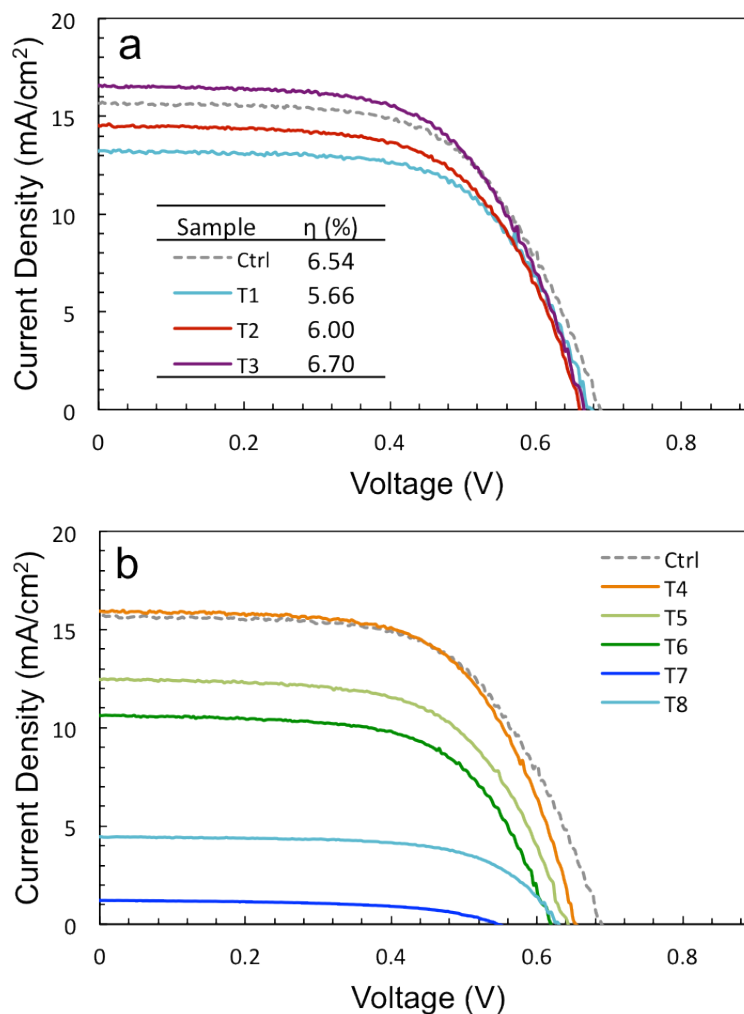
Figure 6.5: J-V curves of DSSCs incorporated with TiO_2 synthesized in a) conventional solvents; and b) bio-sourced solvents.

Table 6.3: J-V characteristics of DSSCs using TiO_2 synthesized in supercritical CO_2.

Sample	V_{OC} (V)	J_{SC} (mA/cm²)	FF	η (%)
Control	0.69	15.65	0.61	6.54
T1	0.68	13.19	0.63	5.66
T2	0.66	14.51	0.62	6.00
T3	0.67	16.54	0.61	6.70
T4	0.65	15.92	0.62	6.50
T5	0.64	12.47	0.63	4.96
T6	0.62	10.61	0.64	4.18
T7	0.55	1.21	0.57	0.38
T8	0.63	4.44	0.65	1.82

The J-V curves of the TiO_2 samples synthesized in green bio-sourced solvents are shown in Figure 6.5b. These samples gave a wider spread of cell performance than the TiO_2 made from conventional solvents. The green curves used ethyl lactate as a solvent and the blue curves used ethyl acetate. Sample T4, TBO precursor in glycerol, obtained the highest efficiency of all the bio-sourced solvents (6.5%), which was on par with the control's performance. This is an indication that a good cell performance can still be achieved by using a less toxic alternative to chlorinated solvents as gas-expanded liquids for making photoactive material.

Samples synthesized in ethyl lactate (T5, T6) produced better efficiencies than samples synthesized in ethyl acetate (T7, T8). In a DSSC photoanode, the photoactive TiO_2 film needs to to have good crystallinity in order to ensure proper electron transport throughout the cell. Similarly, its surface area needs to be high to allow for adequate dye coverage to efficiently absorb sunlight. Since the V_{OC} values of both sets of bio-sourced samples were comparable, the decline in performance of samples T7 and T8 stemmed from lower photocurrent densities, which can be attributed to their weak crystallinity (Figure 6.2) and their unfavorable physical characteristics shown in Table 6.2.

When comparing the two different TiO_2 precursors used, TBO was the superior precursor in ethyl lactate solvent, as T5 gave a better J_{SC} than T6. The SEM micrographs in Figure 6.4 show how the particles in sample T5 seem to be better fused together than the particles in T6, allowing for better electron transport within the photoactive layer during cell operation. However this was not the case for the reactions in ethyl acetate, in which DIPBAT seemed to be the superior precursor. DIPBAT is a less reactive precursor than TBO because its two acetylacetonate ligands are much more kinetically and thermally stable than TBO's butoxy ligands[44]. It therefore follows that the hydrolysis reaction of the DIPBAT precursor occurs less willingly than that of TBO, resulting in a slower and more controlled reaction producing smaller nanoparticles. This is reflected in the BET data listed in Table 6.2.

Figure 6.6 compares the normalized surface areas and efficiencies of the TiO$_2$ samples. Generally, the results follow the expected trend of higher efficiency with higher specific surface area (SSA). For instance, the SSA of T1 and the control are relatively similar, with T1's SSA being slightly less, and their cell efficiencies reflect this. Similarly, T7's cell efficiency is extremely low, which reflects its equally low SSA. Some of the samples however did not follow these expected trends. For example, BET analysis revealed that sample T6 achieved the highest SSA (and smallest average particle size), apart from the control, yet solar simulation testing revealed a mid-range efficiency value. This variation may be explained by the sample's small pore size of 3.3 nm.
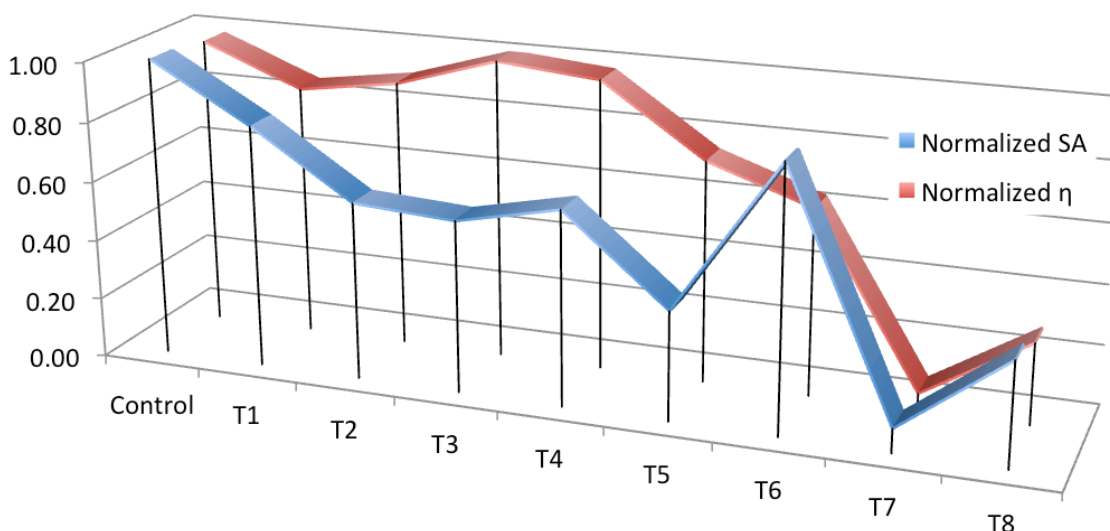
Figure 6.6: The normalized specific surface areas (SA) and corresponding DSSC cell efficiencies (η) of the TiO$_2$ samples.

One must take into account the porosity when considering dye uptake capacity and redox couple shuttling during cell fabrication and operation, respectively. An N$_2$ molecule has a cross-sectional area of 16.2 Å^2, and the size of iodide/triiodide redox couple electrolytes and N719 dye molecules are approximately 4 nm and 1.5 nm, respectively[119]. Consequently, N$_2$ gas adsorption readings are much higher than that of N719 dye because the dye molecules may not be able to enter a structure's smaller pores. To ensure proper dye uptake, and to obtain sufficient electrolyte penetration and diffusion into the pores,

pores of at least 5 nm in diameter are therefore required between the fused TiO_2 nanoparticles in the fabricated photoanodes[119].

Taking a look at the SEM image of sample T6 in Figure 6.4, the particles do indeed look quite small, almost indiscernible, compared to some of the other samples. It is also worth noting that the particles appear very uniform, which allows for closer packing of the nanoparticles. Closer packing reduces a structure's pores significantly compared to a structure containing irregularly sized particles (e.g. T5, Figure 6.4). Therefore, sample T6's average pore size of 3.3 nm does not meet the minimum 5-nm pore diameter requirement, which may help explain why its DSSC efficiency suffered.

This premise holds true in the other direction as well, where a sample composed of larger particles is packed loosely enough to have pore sizes that can accommodate the dye molecules. For instance, although sample T3 did not have the highest SSA, it achieved the highest efficiency (6.70%). Its average pore size was measured to be 6.4 nm, which is in agreement with the larger (yet still uniform) T3 particles shown in Figure 6.4 in comparison to the particles in sample T6.

6.4 Conclusions

This study aimed at developing superior quality TiO_2-based nanomaterials utilizing supercritical CO_2 for applications in DSSCs. More specifically, TiO_2 was synthesized using a modified sol-gel technique in $scCO_2$ to investigate the purity, crystallinity and surface area of the material, and to see how it compared to TiO_2 synthesized via the conventional sol-gel route. This study also introduced the synthesis of TiO_2 NPs based on the coupling of green bio-sourced solvents with supercritical CO_2 for gas-expanded liquid applications, with the hopes of encouraging the development of cleaner processes for nanomaterials used in DSSCs and similar advanced functional devices.

The photovoltaic performance of the TiO_2 prepared with conventional solvents in supercritical CO_2 was comparable to that of the TiO_2 prepared via the conventional sol-

gel route. The highest efficiency was achieved by the non-hydrolytic reaction, and so it was determined that sol-gel reactions performed in supercritical CO_2 should avoid the use of water, which may cause excessive, uncontrolled growth of particles leading to lower surface area, crystallinity and consequently photovoltaic efficiency.

Glycerol exhibited excellent solvent and oxygen-contributing properties in synthesizing TiO_2 photoactive material under supercritical conditions, demonstrating comparable DSSC performance to TiO_2 synthesized via conventional methods. Glycerol is therefore a green bio-sourced solvent which, coupled with $scCO_2$ for gas-expanded liquid applications, has tremendous potential as an alternative to many toxic halogenated solvents.

Finally, surface area and porosity are two important physical properties that impact the performance of a DSSC's photoactive layer. Despite smaller particle sizes generally producing higher surface area materials, the pores of the photoactive material need to have a minimum diameter of 5 nm to ensure proper dye uptake and proper electrolyte penetration into the pores during cell fabrication and cell operation, respectively.

Chapter 7

7 Final Conclusions and Outlook

7.1 Summary of Conclusions

The aim of this thesis was to examine the effects of incorporating ZrO_2 into plasmon-enhanced DSSCs with the goal of counteracting thermal energy loss and correspondingly increasing the allowable plasmon-NP concentration without negatively affecting cell efficiency. This study also introduced the synthesis of TiO_2 NPs based on the coupling of green bio-sourced solvents with supercritical CO_2 for gas-expanded liquid applications, with the hopes of encouraging the development of cleaner processes for nanomaterials used in DSSCs. The work conducted during this thesis resulted in the development of several conclusions, which are briefly summarized below:

Synthesis and characterization of a binary oxide ZrO_2-TiO_2 and its application in dye-sensitized solar cells – It was demonstrated that the addition of zirconia into the photoactive layer of DSSCs inhibited the anatase-rutile phase transformation allowing for higher processing temperatures for increased crystallinity, and stabilized the TiO_2 pore structure at high temperatures, consequently improving device performance. The optimal addition of 5% zirconia demonstrated the best resistance to thermal degradation, achieving the best retention of surface area, particle size and pore size. Solar simulation demonstrated that performance was optimal at 5% Zr doping concentrations. The samples showing the best performance were used as the base photoactive layer for plasmon-enhanced DSSCs.

The Effect of Zirconia Doping on the Performance of Plasmon-Enhanced DSSCs – Zirconia was shown to thermostabilize the effects of heat loss created by $Ag@TiO_2$ doping in both plasmonic DSSC architectures studied, resulting in increased optical absorption and photocurrent. The thermostabilizing effects were more pronounced in the

'chocolate-chip' architecture, where the plasmonic nanoparticles were dispersed throughout the photoactive layer. Additionally, it was demonstrated that incorporating zirconia into the 'chocolate-chip' DSSCs permitted the plasmon-doping threshold to be increased to 5 % before submitting to a decrease in efficiency, which is an improvement on the 0.6% doping limit reported in literature. The 'chocolate-chip' architecture demonstrated superior performance over the 'blanket-array' architecture in the presence of ZrO_2, despite the unsuccessful coating of TiO_2 on the silver NPs' surface. Both the photocurrent and fill factor were significantly enhanced, and a PCE of 6.32% was observed in the presence of zirconia, compared to 4.38% without zirconia. The thermostabilizing benefits of ZrO_2 were limited in the 'blanket-array' architecture, as the addition of 5% Zr only marginally improved the cell efficiency from 5.25 to 5.27%. It was therefore determine that the 'chocolate-chip' architecture was the superior cell design for incorporating $Ag@TiO_2$ NPs into Zr-doped DSSCs.

The performance of TiO_2 nanoparticles synthesized in supercritical CO_2 as photoactive material in DSSCs – The photovoltaic performance of the TiO_2 prepared with conventional solvents in supercritical CO_2 was comparable to that of the TiO_2 prepared via the conventional sol-gel route. The highest efficiency was achieved by the non-hydrolytic reaction (6.70%), and so it was determined that sol-gel reactions performed in supercritical CO_2 should avoid the use of water, which may cause excessive, uncontrolled growth of particles leading to lower surface area, crystallinity and consequently photovoltaic efficiency. Among the bio-sourced solvents, glycerol demonstrated excellent solvent and oxygen-contributing properties in synthesizing TiO_2 photoactive material under supercritical conditions, achieving a PCE of 6.50%. This is comparable to the performance of DSSCs using TiO_2 synthesized via conventional methods (6.54%). Glycerol is therefore a green bio-sourced solvent which, coupled with $scCO_2$ for gas-expanded liquid applications, has tremendous potential as an alternative to many toxic halogenated solvents.

The successful synthesis of TiO_2 using bio-sourced solvents makes a valuable contribution to the development of greener processes, and opens up new opportunities to link green chemistry and green process engineering to develop an entire green production process for nanomaterials which are required for next-generation advanced functional devices. The optimized plasmonic DSSC architectures developed during this thesis make a valuable contribution to the development and commercialization of inexpensive and high efficiency plasmon-enhanced DSSCs. Considering the two architectures proposed, the findings in this research thesis may inspire scientists and engineers to explore further plasmonic-enhanced applications such as photocatalysis, sensing, solar water splitting, and environmental remediation. Zirconia's thermostabilizing effect in plasmon-enhanced DSSCs can also lead to new solar cell designs with smaller semiconductor thicknesses and thus lower material costs. This has important technical and strategic consequences, as the PV industry is projected to scale-up in manufacturing capacity from its present level of a few GW in 2015 to over 200 GW by 2050, and eventually to the TW scale.

7.2   Assumptions and Limitations of Thesis Work

Even though visible achievements have been made on plasmonic enhanced photovoltaics, there still exist limitations and knowledge gaps in the field of plasmonic photovoltaics, and more work needs to be done in the future to improve the photovoltaic performance of DSSCs and to clarify the charge transfer mechanism.

There are a few assumptions and limitations that need to be considered. Firstly, although BET data obtained for this thesis are useful in highlighting trends in porosity and specific surface area, dye-loading data obtained from Freundlich isotherms, which use N719 dye instead of nitrogen gas, can provide a more accurate picture of metal oxide surface area for dye binding. This is because N_2 physisorbs to all surfaces, TiO_2 surface and residual organic matter included, which distorts the reported surface area. N719 dye however will only chemisorb to "free" metal oxides surfaces. Furthermore, a N_2 molecule is much smaller than a N719 molecule, so their sorption characteristics will be different.

Unfortunately, obtaining Freundlich isotherms are much more expensive, due to the high cost of the dye.

A limitation of the thesis work was the inability to conduct quantum efficiency measurements. Spectral response measurements would be very valuable to have in order to determine which wavelengths of the visible light spectrum are specifically being enhanced by the plasmon resonance. Our lab is in the process of investing in a Quantum Efficiency Measurement System that is able to acquire this type of data. Knowing the spectral response of plasmonic excitement would allow us to tailor our plasmonic nanoparticle geometries to target those specific areas of the solar spectrum, which would result in enhanced light absorption.

Finally, the cost of plasmonic metals is still high. The practical application of plasmonic photovoltaics is a big issue, because the plasmonic photovoltaics heavily depend on the use of gold or silver nanostructures since they express resonance in the visible spectrum.

7.3   Outlook (Future work)

Integrating metallic nanostructures into the photoactive cell layer and taking advantage of their resonance with incoming light is an effective way to increase light absorption in DSSCs. Plasmon resonance conditions are highly dependent on the geometry of the particle, the dielectric constant of the metal and the local environment. An electron cloud would take a different amount of time to oscillate, and oscillate in a different way for a rod- or a square-shaped metallic structure, or another unique shape. This would result in different resonances at different frequencies. In addition, if particles are close together, resonance coupling may be observed. Therefore, plasmonic enhancement can be tuned throughout the visible wavelength range by changing the geometry of the plasmonic nanostructure.

Future investigations and developments should examine the effects of different particle geometries. It would be interesting to see whether a particle geometry exists that would

produce multiple resonance peaks, which could contribute to a wider, panchromatic absorption spectrum for DSSC photoabsorptive layers. It could also be interesting to modify the surrounding environment of the plasmonic nanostructures, such as doping the TiO_2 shell layers with zirconia to see how the resonance peak intensities and locations are affected, as well as if the thermostabilizing properties of zirconia would contribute positively.

Plasmonic nanostructures will play an increasingly larger role in solar energy harvesting. The simple solution of blending plasmonic NPs with available photoactive materials to enhance light harvesting highlights easy fabrication, and may benefit solar cells using other photoabsorbers or other types of solar-harvesting devices. Additionally, the fabrication method for plasmon-enhanced DSSCs is compatible with large-scale processes, such as printing, jet spraying[14,43] and roll-to-roll processing[15,120], making manufacturing and commercialization of DSSCs more feasible. Furthermore, since light harvesting is the initial stage of a series of physical, chemical or biochemical processes in many solar energy conversion devices, plasmon-NP resonance may benefit many other devices including artificial photosynthesis[121], solar heating[76], solar thermal electricity, and solar fuels[122].

References

1. International Energy Agency. *2013 Key World Energy Statistics*. (2013). doi:10.1007/978-3-540-33866-6

2. International Energy Agency. *World Energy Outlook 2014*. (2015).

3. International Energy Agency. *Snapshot of Global PV Markets 2014*. (2015).

4. Arvizu, D. *et al.* in *IPCC Spec. Rep. Renew. Energy Sources Clim. Chang. Mitig.* (Edenhofer, O. et al.) (Cambridge University Press, 2011).

5. SBC Energy Institute. *Solar Photovoltaic: Leading the Energy Transition (Factbook)*. (2013). at <http://www.sbc.slb.com/sbcinstitute.aspx>

6. Wang, X., Byrne, J., Kurdgelashvili, L. & Barnett, A. High efficiency photovoltaics: on the way to becoming a major electricity source. *Wiley Interdiscip. Rev. Energy Environ.* **1,** 132–151 (2012).

7. Tiedje, T., Yablonovitch, E., Cody, G. D. & Brooks, B. G. Limiting efficiency of silicon solar cells. *IEEE Trans. Electron Devices* **31,** 711–716 (1984).

8. Blakers, A. W., Wang, A., Milne, A. M., Zhao, J. & Green, M. A. 22.8% efficient silicon solar cell. *Appl. Phys. Lett.* **55,** 1363 (1989).

9. Dicker, J., Schumacher, J. O., Warta, W. & Glunz, S. W. Analysis of one-sun monocrystalline rear-contacted silicon solar cells with efficiencies of 22.1%. *J. Appl. Phys.* **91,** 4335 (2002).

10. Green, M. A. The path to 25% silicon solar cell efficiency: History of silicon cell evolution. *Prog. Photovoltaics Res. Appl.* **17,** 183–189 (2009).

11. Castrucci, P. Carbon nanotube/silicon hybrid heterojunctions for photovoltaic devices. **2,** 23–56 (2014).

12. Gevaerts, V. *Morphology control and device optimization for efficient organic solar cells*. *alexandria.tue.nl* (Eindhoven, 2013).

13. Baxter, J. B. Commercialization of dye sensitized solar cells: Present status and future research needs to improve efficiency, stability, and manufacturing. *J. Vac. Sci. Technol. A Vacuum, Surfaces, Film.* **30,** 020801 (2012).

14. Eslamian, M. Spray-on Thin Film PV Solar Cells: Advances, Potentials and Challenges. *Coatings* **4,** 60–84 (2014).

15. Gong, J., Liang, J. & Sumathy, K. Review on dye-sensitized solar cells (DSSCs):

Fundamental concepts and novel materials. *Renew. Sustain. Energy Rev.* **16,** 5848–5860 (2012).

16. O'Regan, B. & Grätzel, M. A low-cost, high-efficiency solar cell based on dye-sensitized colloidal TiO2 films. *Nature* **353,** 737–740 (1991).

17. Mathew, S. *et al.* Dye-sensitized solar cells with 13% efficiency achieved through the molecular engineering of porphyrin sensitizers. *Nat. Chem.* **6,** 242–247 (2014).

18. Fakharuddin, A., Jose, R., Brown, T. M., Fabregat-Santiago, F. & Bisquert, J. A perspective on the production of dye-sensitized solar modules. *Energy Environ. Sci.* **7,** 3952–3981 (2014).

19. Wu, J. *et al.* Electrolytes in Dye-Sensitized Solar Cells. *Chem. Rev.* (2015). doi:10.1021/cr400675m

20. Green, M. A., Emery, K., Hishikawa, Y., Warta, W. & Dunlop, E. D. Solar cell efficiency tables (version 44). *Prog. Photovoltaics Res. Appl.* **22,** 701–710 (2014).

21. Kojima, A., Teshima, K., Shirai, Y. & Miyasaka, T. Organometal Halide Perovskites as Visible-Light Sensitizers for Photovoltaic Cells. *J. Am. Chem. Soc.* **131,** 6050–6051 (2009).

22. Im, J.-H., Lee, C.-R., Lee, J.-W., Park, S.-W. & Park, N.-G. 6.5% efficient perovskite quantum-dot-sensitized solar cell. *Nanoscale* **3,** 4088 (2011).

23. Yun, M. J., Cha, S. I., Seo, S. H. & Lee, D. Y. Highly Flexible Dye-sensitized Solar Cells Produced by Sewing Textile Electrodes on Cloth. *Sci. Rep.* **4,** (2014).

24. Wu, W.-Q., Xu, Y.-F., Rao, H.-S., Su, C.-Y. & Kuang, D.-B. A Tri-Layered Photoanode of TiO 2 Nanoparticles on 1D-3D Nanostructured TiO 2 -Grown Flexible Ti Substrate for High-Efficiency (9.1%) Dye-Sensitized Solar Cells with Unprecedentedly High Photocurrent Density. *J. Phys. Chem. C* 140117113713007 (2014). doi:10.1021/jp4116782

25. Ming, L. *et al.* Selective laser sintering of TiO2 nanoparticle film on plastic conductive substrate for highly efficient flexible dye-sensitized solar cell application. *J. Mater. Chem. A* **2,** 4566 (2014).

26. Yamaguchi, T., Tobe, N., Matsumoto, D., Nagai, T. & Arakawa, H. Highly efficient plastic-substrate dye-sensitized solar cells with validated conversion efficiency of 7.6%. *Sol. Energy Mater. Sol. Cells* **94,** 812–816 (2010).

27. Hagfeldt, A., Boschloo, G., Sun, L., Kloo, L. & Pettersson, H. Dye-sensitized solar cells. *Chem. Rev.* **110,** 6595–663 (2010).

28. Vatansever, D., Siores, E. & Shah, T. in *Glob. Warm. - Impacts Futur. Perspect.* (Singh, B. R.) (CC BY, 2012). doi:10.5772/50570

29. Yen, Y.-S., Chou, H.-H., Chen, Y.-C., Hsu, C.-Y. & Lin, J. T. Recent developments in molecule-based organic materials for dye-sensitized solar cells. *J. Mater. Chem.* **22,** 8734 (2012).

30. Chen, C. *et al.* Highly efficient light-harvesting ruthenium sensitizer for thin-film dye-sensitized solar cells. *ACS Nano* **3,** 3103–9 (2009).

31. Singh, M. *et al.* Characterization of metal-free D-(π-A)2 organic dye and its application as cosensitizer along with N719 dye for efficient dye-sensitized solar cells. *Indian J. Phys.* (2015). doi:10.1007/s12648-015-0681-0

32. Balasingam, S. K., Lee, M., Kang, M. G. & Jun, Y. Improvement of dye-sensitized solar cells toward the broader light harvesting of the solar spectrum. *Chem. Commun.* **49,** 1471–1487 (2013).

33. Ngamsinlapasathian, S., Sreethawong, T., Suzuki, Y. & Yoshikawa, S. Single- and double-layered mesoporous TiO2/P25 TiO2 electrode for dye-sensitized solar cell. *Sol. Energy Mater. Sol. Cells* **86,** 269–282 (2005).

34. Dang, X. *et al.* Virus-templated self-assembled single-walled carbon nanotubes for highly efficient electron collection in photovoltaic devices. *Nat. Nanotechnol.* **6,** 377–84 (2011).

35. Kawano, R. & Watanabe, M. Equilibrium potentials and charge transport of an I-/I3- redox couple in an ionic liquid. *Chem. Commun. (Camb).* 330–331 (2003). doi:10.1039/b208388b

36. Stathatos, E. in *Dye Sensitized Sol. Cells as an Altern. approach to Conv. Photovolt. Technol. based silicon* (2011). doi:10.5772/23650

37. Gupta, D., Mukhopadhyay, S. & Narayan, K. S. Fill factor in organic solar cells. *Sol. Energy Mater. Sol. Cells* **94,** 1309–1313 (2010).

38. Shah, A. Photovoltaic Technology: The Case for Thin-Film Solar Cells. *Science (80-.).* **285,** 692–698 (1999).

39. Hoffmann, W. PV solar electricity industry: Market growth and perspective. *Sol. Energy Mater. Sol. Cells* **90,** 3285–3311 (2006).

40. Atwater, H. a & Polman, A. Plasmonics for improved photovoltaic devices. *Nat. Mater.* **9,** 205–213 (2010).

41. Voisin, C., Del Fatti, N., Christofilos, D. & Vallée, F. Ultrafast Electron Dynamics and Optical Nonlinearities in Metal Nanoparticles. *J. Phys. Chem. B* **105,** 2264–2280 (2001).

42. Kumar, M. K. *et al.* Field Effects in Plasmonic Photocatalyst by Precise SiO 2 Thickness Control Using Atomic Layer Deposition. *ACS Catal.* **1,** 300–308

(2011).

43. Qi, J., Dang, X., Hammond, P. T. & Belcher, A. M. Highly efficient plasmon-enhanced dye-sensitized solar cells through metal@oxide core-shell nanostructure. *ACS Nano* **5,** 7108–16 (2011).

44. Alonso, E., Montequi, I., Lucas, S. & Cocero, M. J. Synthesis of titanium oxide particles in supercritical CO2: Effect of operational variables in the characteristics of the final product. *J. Supercrit. Fluids* **39,** 453–461 (2007).

45. Hald, P. *et al.* Supercritical Propanol–Water Synthesis and Comprehensive Size Characterisation of Highly Crystalline anatase TiO2 Nanoparticles. *J. Solid State Chem.* **179,** 2674–2680 (2006).

46. Da Silva, E. P. *et al.* scCO2-based synthesis of semi-crystalline TiO2 nanoparticles: A rapid and direct strategy. *Mater. Lett.* **136,** 133–137 (2014).

47. Theyssen, N. *et al. Handbook of Green Chemistry, Volume 4: Supercritical Solvents*. (Wiley-VCH, 2013).

48. Zou, G., Jiang, H.-F. & Chen, M.-C. Chemical Reactions in Supercritical Carbon Dioxide. *I* **51A,** 1298–1305 (2012).

49. Sui, R., Rizkalla, A. S. & Charpentier, P. a. Formation of titania nanofibers: A direct sol-gel route in supercritical CO2. *Langmuir* **21,** 6150–6153 (2005).

50. Aksomaityte, G., Alonso, E. & Cocero, M. J. Synthesis of doped TiO2 metal oxide nanoparticles in supercritical CO2. *AIChE Annu. Meet., Conf. Proc.* 389/1–389/2 (2008).

51. Abrams, N. M. Efficiency Enhancement in Dye-Sensitized Solar Cells Through Light Manipulation. (2005).

52. Li, B., Wang, L., Kang, B., Wang, P. & Qiu, Y. Review of recent progress in solid-state dye-sensitized solar cells. *Sol. Energy Mater. Sol. Cells* **90,** 549–573 (2006).

53. Adrian Gaitan, T., Bennett, C. & Davenport, R. *Materials and technologies for solar energy*. (2009). at <http://chemical.ihs.com/nl/Public/2009/0904/0904.html#a=>

54. Dang, X. *et al.* Tunable localized surface plasmon-enabled broadband light-harvesting enhancement for high-efficiency panchromatic dye-sensitized solar cells. *Nano Lett.* **13,** 637–42 (2013).

55. Xu, Q., Liu, F., Meng, W. & Huang, Y. Plasmonic core-shell metal-organic nanoparticles enhanced dye-sensitized solar cells. **20,** 898–907 (2012).

56. Xu, Q. *et al.* Broadband light absorption enhancement in dye-sensitized solar cells with Au-Ag alloy popcorn nanoparticles. *Sci. Rep.* **3,** 2112 (2013).

57. Pillai, S., Catchpole, K. R., Trupke, T. & Green, M. A. Surface plasmon enhanced silicon solar cells. in *J. Appl. Phys.* **101,** (2007).

58. Rand, B. P., Peumans, P. & Forrest, S. R. Long-range absorption enhancement in organic tandem thin-film solar cells containing silver nanoclusters. *J. Appl. Phys.* **96,** 7519–7526 (2004).

59. Hägglund, C., Zäch, M. & Kasemo, B. Enhanced charge carrier generation in dye sensitized solar cells by nanoparticle plasmons. *Appl. Phys. Lett.* **92,** 013113 (2008).

60. Lin, S. J., Lee, K. C., Wu, J. L. & Wu, J. Y. Plasmon-enhanced photocurrent in dye-sensitized solar cells. *Sol. Energy* **86,** 2600–2605 (2012).

61. Paci, B. *et al.* Enhancement of photo/thermal stability of organic bulk heterojunction photovoltaic devices via gold nanoparticles doping of the active layer. *Nanoscale* **4,** 7452 (2012).

62. Link, S. & El-Sayed, M. a. Size and Temperature Dependence of the Plasmon Absorption of Colloidal Gold Nanoparticles. *J. Phys. Chem. B* **103,** 4212 (1999).

63. Zhou, N. *et al.* Plasmon-Enhanced Light Harvesting: Applications in Enhanced Photocatalysis, Photodynamic Therapy and Photovoltaics. *RSC Adv.* (2015). doi:10.1039/C5RA01819F

64. Guo, K. *et al.* Preparation and enhanced properties of dye-sensitized solar cells by surface plasmon resonance of Ag nanoparticles in nanocomposite photoanode. *J. Power Sources* **230,** 155–160 (2013).

65. Du, P. *et al.* Synthesis of thermally stable Ag@TiO2 core–shell nanoprisms and plasmon–enhanced optical properties for a P3HT thin film. *RSC Adv.* **3,** 6016 (2013).

66. Niesen, B. *et al.* Excitation of multiple dipole surface plasmon resonances in spherical silver nanoparticles. *Opt. Express* **18,** 19032–19038 (2010).

67. Awazu, K. *et al.* A plasmonic photocatalyst consisting of silver nanoparticles embedded in titanium dioxide. *J. Am. Chem. Soc.* **130,** 1676–1680 (2008).

68. Catchpole, K. R. & Polman, A. Design principles for particle plasmon enhanced solar cells. *Appl. Phys. Lett.* **93,** (2008).

69. Mertz, J. Radiative absorption, fluorescence, and scattering of a classical dipole near a lossless interface: a unified description. *J. Opt. Soc. Am. B* **17,** 1906 (2000).

70.   Marinel, S., Choi, D. H., Heuguet, R., Agrawal, D. & Lanagan, M. Broadband dielectric characterization of TiO2 ceramics sintered through microwave and conventional processes. *Ceram. Int.* **39,** 299–306 (2013).

71.   Ahmad, Z. in *Dielectr. Mater.* (InTech, 2012). doi:10.5772/50638

72.   Scheinert, S., Paasch, G., Hörselmann, I. & Herasimovich, A. in *Org. Electron.* (Grasser, T., Meller, G. & Li, L.) **223,** 163 (Springer Berlin Heidelberg, 2010).

73.   Bohren, C. F. & Huffman, D. R. *Absorption and scattering of light by small particles. Res. Support. by Univ. Arizona Inst. Occup. Environ. Heal. New York WileyInterscience 1983 541 p* **1,** (1983).

74.   Shockley, W. & Queisser, H. J. Detailed balance limit of efficiency of p-n junction solar cells. *J. Appl. Phys.* **32,** 510–519 (1961).

75.   Cushing, S. K. & Wu, N. Plasmon-Enhanced Solar Energy Harvesting. *Electrochem. Soc. Interface* **2,** 63–67 (2013).

76.   Linic, S., Christopher, P. & Ingram, D. B. Plasmonic-metal nanostructures for efficient conversion of solar to chemical energy. *Nat. Mater.* **10,** 911–21 (2011).

77.   Dürr, M., Rosselli, S., Yasuda, A. & Nelles, G. Band-Gap Engineering of Metal Oxides for Dye-Sensitized Solar Cells. *J. Phys. …* **110,** 21899–21902 (2006).

78.   Kitiyanan, A., Sakulkhaemaruethai, S., Suzuki, Y. & Yoshikawa, S. Structural and photovoltaic properties of binary TiO2-ZrO2 oxides system prepared by sol-gel method. *Compos. Sci. Technol.* **66,** 1259–1265 (2006).

79.   Hernández-Alonso, M. D., Tejedor-Tejedor, I., Coronado, J. M., Soria, J. & Anderson, M. A. Sol-gel preparation of TiO2-ZrO2 thin films supported on glass rings: Influence of phase composition on photocatalytic activity. in *Thin Solid Films* **502,** 125–131 (2006).

80.   Reidy, D. J., Holmes, J. D. & Morris, M. A. Preparation of a highly thermally stable titania anatase phase by addition of mixed zirconia and silica dopants. *Ceram. Int.* **32,** 235–239 (2006).

81.   Sui, R. & Charpentier, P. Synthesis of metal oxide nanostructures by direct sol-gel chemistry in supercritical fluids. *Chem. Rev.* **112,** 3057–82 (2012).

82.   Lucky, R. a. & Charpentier, P. a. A One-Step Approach to the Synthesis of ZrO2-Modified TiO2 Nanotubes in Supercritical Carbon Dioxide. *Adv. Mater.* **20,** 1755–1759 (2008).

83.   Lucky, R. a, Medina-Gonzalez, Y. & Charpentier, P. a. Zr doping on one-dimensional titania nanomaterials synthesized in supercritical carbon dioxide. *Langmuir* **26,** 19014–21 (2010).

84. Sashchiuk, A. *et al.* Optical and conductivity properties of PbS nanocrystals in amorphous zirconia sol-gel films. *J. Sol-Gel Sci. Technol.* **24,** 31–38 (2002).

85. Miao, Z., Xu, L., Song, H., Zhao, H. & Chou, L. One-pot synthesis of ordered mesoporous zirconium oxophosphate with high thermostability and acidic properties. *Catal. Sci. Technol.* **3,** 1942 (2013).

86. Namavar, F. *et al.* Thermal stability of nanostructurally stabilized zirconium oxide. *Nanotechnology* **18,** 415702 (2007).

87. Niederberger, M. in *Met. Oxide Nanoparticles Org. Solvents* 7–19 (2009). doi:bfm:978-1-84882-671-7/1

88. Lucky, R. a. SYNTHESIS OF TiO 2 -BASED NANOSTRUCTURED MATERIALS USING A SOL-GEL PROCESS IN SUPERCRITICAL CO 2. **2,** 265 (2008).

89. Chen, Y., Zhou, S., Gu, G. & Wu, L. Microstructure and properties of polyester-based polyurethane/titania hybrid films prepared by sol–gel process. *Polymer (Guildf).* **47,** 1640–1648 (2006).

90. Charitidis, C. A., Georgiou, P., Koklioti, M. A., Trompeta, A.-F. & Markakis, V. Manufacturing nanomaterials: from research to industry. *Manuf. Rev.* **1,** 11 (2014).

91. Pastoriza-Santos, I. *et al.* One-pot synthesis of Ag@ TiO2 core-shell nanoparticles and their layer-by-layer assembly. *Langmuir* **16,** 2731–2735 (2000).

92. Tom, R. T. *et al.* Freely Dispersible Au@TiO 2 , Au@ZrO 2 , Ag@TiO 2 , and Ag@ZrO 2 Core−Shell Nanoparticles: One-Step Synthesis, Characterization, Spectroscopy, and Optical Limiting Properties. *Langmuir* **19,** 3439–3445 (2003).

93. Lin, Y. *et al.* Synthesis of Ag/TiO 2 Core/Shell Nanoparticles with Antibacterial Properties. *Bull. Korean Chem. Soc.* **32,** 2607–2610 (2011).

94. Evanoff, D. D. & Chumanov., G. Size-controlled synthesis of nanoparticles. 1. 'Silver only' Aqueous suspension via Hydrogen reduction. *J. Phys. Chem. B* **108,** 13948 (2004).

95. Standridge, S. D., Schatz, G. C. & Hupp, J. T. Toward plasmonic solar cells: protection of silver nanoparticles via atomic layer deposition of TiO2. *Langmuir* **25,** 2596–2600 (2009).

96. Zielinski, J. M. & Kettle, L. *Physical Characterization : Surface Area and Porosity*. (2013).

97. Schattka, J. H., Shchukin, D. G., Jia, J., Antonietti, M. & Caruso, R. A. Photocatalytic Activities of Porous Titania and Titania/Zirconia Structures Formed by Using a Polymer Gel Templating Technique. *Chem. Mater.* **14,** 5103–5108

(2002).

98.   Linsebigler, A. L. *et al.* Photocatalysis on TiO2 Surfaces: Principles, Mechanisms, and Selected Results. *Chem. Rev.* **95,** 735–758 (1995).

99.   Abd El-Lateef, H. M. & Khalaf, M. M. Corrosion resistance of ZrO2–TiO2 nanocomposite multilayer thin films coated on carbon steel in hydrochloric acid solution. *Mater. Charact.* **108,** 29–41 (2015).

100.   Zheleznov, V. V., Sushkov, Y. V., Voit, E. I., Sarin, S. A. & Dmitrieva, E. É. Effect of ZrO2 on the Structure of ZrO2/TiO2/SiO2 Nanocomposites Fabricated by a Template Sol–Gel Method. *J. Appl. Spectrosc.* **81,** 983–989 (2015).

101.   Kim, J., Song, K. C., Foncillas, S. & Pratsinis, S. E. Dopants for synthesis of stable bimodally porous titania. *J. Eur. Ceram. Soc.* **21,** 2863–2872 (2001).

102.   Hanaor, D. a H. & Sorrell, C. C. Review of the anatase to rutile phase transformation. *J. Mater. Sci.* **46,** 855–874 (2011).

103.   Venkatachalam, N., Palanichamy, M., Arabindoo, B. & Murugesan, V. Enhanced photocatalytic degradation of 4-chlorophenol by Zr4+ doped nano TiO2. *J. Mol. Catal. A Chem.* **266,** 158–165 (2007).

104.   Bendoni, R. *et al.* Alternative route for the preparation of Zr – doped TiO2 layers for energy and environmental applications. *Ceram. Int.* (2015). doi:10.1016/j.ceramint.2015.04.067

105.   Sing, K. S. W. Reporting physisorption data for gas/solid systems with special reference to the determination of surface area and porosity (Recommendations 1984). *Pure Appl. Chem.* **57,** 603–619 (1985).

106.   Lowell, S., Shields, J. E. & Morral, J. E. Powder Surface Area and Porosity, 2nd Edition. *J. Eng. Mater. Technol.* **107,** 180 (1985).

107.   Chang, S. & Doong, R. Characterization of Zr-Doped TiO 2 Nanocrystals Prepared by a Nonhydrolytic Sol - Gel Method at High Temperatures. 20808–20814 (2006).

108.   Burda, C., Chen, X., Narayanan, R. & El-Sayed, M. a. *Chemistry and properties of nanocrystals of different shapes. Chem. Rev.* **105,** (2005).

109.   Wurfel, U., Peters, M. & Hinscht, A. Detailed experimental and theoretical investigation of the electron transport in a dye solar cell by means of a three-electrode configuration. *J. Phys. Chem. C* **112,** 1711–1720 (2008).

110.   Kumbhar, A. S., Kinnan, M. K. & Chumanov, G. Multipole plasmon resonances of submicron silver particles. *J. Am. Chem. Soc.* **127,** 12444–12445 (2005).

111. Link, S. & El-Sayed, M. a. Shape and size dependence of radiative, non-radiative and photothermal properties of gold nanocrystals. *Int. Rev. Phys. Chem.* **19,** 409–453 (2000).

112. Thomas, S. *et al.* Size-dependent surface plasmon resonance in silver silica nanocomposites. *Nanotechnology* **19,** 075710 (2008).

113. Link, S., Link, S., El-Sayed, M. a. & El-Sayed, M. Spectral Properties and Relaxation Dynamics of Surface Plasmon Electronic Oscillations in Gold and Silver Nanodots and Nanorods. *J. Phys. Chem. B* **103,** 8410–8426 (1999).

114. Brayner, R., Fiever, F. & Thibaud, C. Nanomaterials: A Danger or a Promise? 407 (2013). doi:10.1007/978-1-4471-4213-3

115. Holliman, P. J. *et al.* Low temperature sintering of binder-containing TiO2/metal peroxide pastes for dye-sensitized solar cells. *J. Mater. Chem. A* (2014). doi:10.1039/c4ta01000k

116. Leitner, W. Reactions in supercritical carbon dioxide (scCO2). *Mod. Solvents Org. Synth.* **206,** 107–132 (1999).

117. Jessop, P. G. Applications of CO2 in homogeneous catalysis. *Abstr. Pap. Am. Chem. Soc.* **227,** U1069–U1069 (2004).

118. Saunders, S. R. Use of Gas-Expanded Liquids as Tunable Solvents for the Preparation of Well-Defined Nanomaterials. 1–191 (2011).

119. Parmar, K. P. S., Ramasamy, E., Lee, J. & Lee, J. S. Rapid (~10 min) synthesis of single-crystalline, nanorice TiO2 mesoparticles with a high photovoltaic efficiency of above 8%. *Chem. Commun.* **47,** 8572 (2011).

120. Law, M., Greene, L. E., Johnson, J. C., Saykally, R. & Yang, P. Nanowire dye-sensitized solar cells. *Nat. Mater.* **4,** 455–9 (2005).

121. Gao, H., Liu, C., Jeong, H. E. & Yang, P. Plasmon-enhanced photocatalytic activity of iron oxide on gold nanopillars. *ACS Nano* **6,** 234–40 (2012).

122. Thomann, I. *et al.* Plasmon enhanced solar-to-fuel energy conversion. *Nano Lett.* **11,** 3440–6 (2011).

Curriculum Vitae

Name:	Anastasia Pasche
Post-secondary Education and Degrees:	University of Waterloo Waterloo, Ontario, Canada 2007-2013 B.A.Sc. The University of Western Ontario London, Ontario, Canada 2013-2015 M.E.Sc.
Honours and Awards:	Ontario Society of Professional Engineers' The Personal Scholarship 2015
Related Work Experience	Teaching Assistant The University of Western Ontario 2014-2015